STARS

2021

Studies on Powder Compaction and Wire Extrusion of Pure Metals and Metal/CNT Nano Composites

Qiang Zhou
University of Central Florida

Showcase of Text, Archives, Research & Scholarship

STUDIES ON POWDER COMPACTION AND WIRE EXTRUSION OF PURE METALS AND METAL/CNT NANO COMPOSITES

by

QIANG ZHOU
B.S. Northeast Agriculture University, China, 2004
M.S. Harbin Institute of Technology, China, 2007

A dissertation submitted in partial fulfillment of the requirements
for the degree of Doctor of Philosophy
in the Department of Mechanical and Aerospace Engineering
in the College of Engineering and Computer Science
at the University of Central Florida
Orlando, Florida

Summer Term
2021

Major Professor: Yuanli Bai

ABSTRACT

The goal of this dissertation is to fabricate wires made of Cu/CNT and Al/CNT composites with good mechanical strength and super thermal/electrical conductivities using powder compaction and wire extrusion manufacturing processes. Powder compaction was studied using both test and simulation. Cold compaction, hot compaction and vibration assisted (cold) compaction tests were conducted to achieve different density ratios. Hot compaction tests improved about 6% compared with cold compaction under the same compression pressure. Although the relative density ratio does not obviously improve at vibration assisted (cold) compaction, the strength of the specimens made under vibration loading is much better than those of cold compaction. Additionally, finite element models with well calibrated Drucker Prager Cap (DPC) material constitutive model were built in Abaqus/Standard to simulate powder compaction processes. The results of finite element model have excellent correlations with test results up to the tested range, and finite element models can further predict the loading conditions required in order to achieve the higher density ratios of the materials. Two exponential formulas for predicting density ratio were obtained by combining the test data and the simulation results. A new analytical solution was first time developed to predict the axial pressure versus the density ratio for powder compaction according to DPC material model. The results between analytical solution and simulation model have an excellent match.

Extrusion method was adopted to produce wires of aluminum (Al), copper (Cu) and copper/carbon nanotubes (Cu/CNTs) composites. A new analytical solution was developed to predict magnitude of extrusion force, where friction effects between die and sample were considered. The analytical solution achieved a much better result than the classical slip line theory and other existing

analytical solutions. Extensive finite element (FE) models were built to validate the analytical solution under different extrusion conditions. FE simulation cases were run for different die angles (including 30°, 45° and 60°) and different extrusion area ratios (including 16:1 and 4:1). The comparison results showed a good match between analytical solutions and finite element models. Both Eulerian and Lagrangian methods were set up and compared in finite element models in order to predict the extrusion force during the extrusion process.

Four wire extrusion tests of metals and metal/CNTs composites were successfully conducted under elevated temperatures ranging from 300°C to 703°C. Test results further validated the accuracy of the analytical solution.

KEYWORDS: Powder Compaction, Wire Extrusion, Finite Element Simulation, Analytical Solutions.

ACKNOWLEDGMENTS

TABLE OF CONTENTS

LIST OF FIGURES

xiii

LIST OF TABLES

CHAPTER 1 INTRODUCTION

1.1 Background

Global energy consumptions grow year by year at an unprecedent speed in order to develop economy and improve people's living conditions from all over the world. Global energy consumption is shown in Figure 1, one can conclude that energy consumption had increased to more than 160,000TWh by 2019.
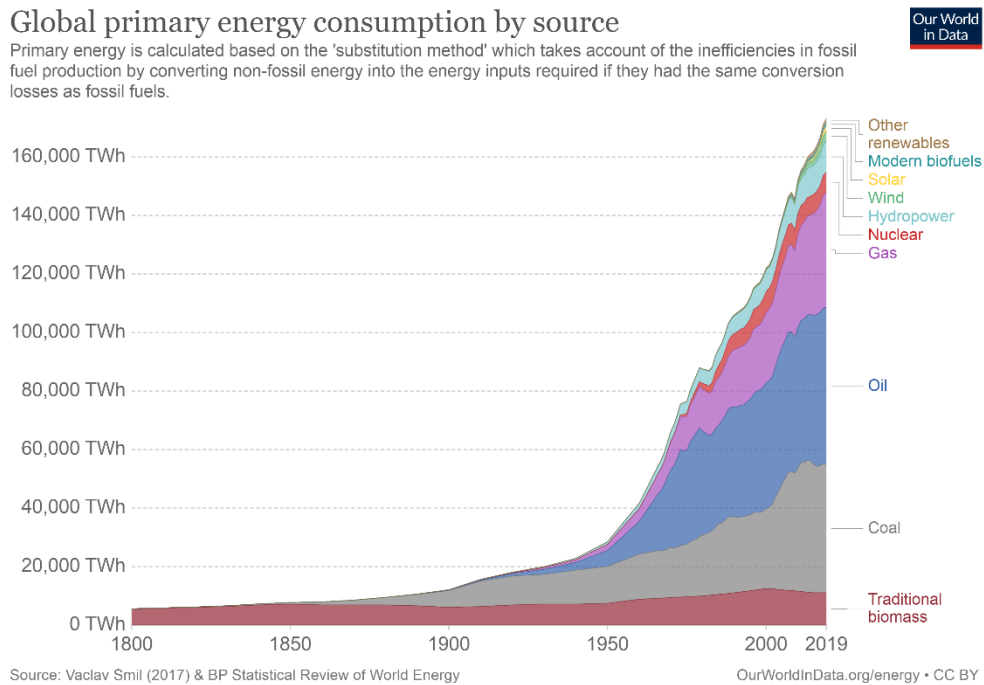
Figure 1. Global energy consumption from 1800 to 2019 (Smil, 2016).

One of the most predominant energy consumptions is the non-renewable resource, which would be run out in future. Thus, we face a huge burden from the energy supply to find the solutions. One solution is to use more renewable resource such as wind, hydropower and nuclear energy. Wind energy usage has reached to 1400TWh by 2019 and supplied 5% of electricity generation around the world. Wind energy has several disadvantages. They are stability, transmission and costs.

Because wind farms must be in some special places, usually they are far from the city. Hydropower energy is the primary use in the modern society for the generation of the electricity. Although hydroelectric power is a good way to generate the electricity without adding substantial carbon, the dams have the negative environmental impacts. Nuclear energy can provide the electricity from the heat of the nuclear reaction energy. The safety of the nuclear energy is the most concern, thus there is still not the most popular energy in the world.

Another necessary solution is to reduce the energy consumptions for the sustainable development of human society. Many energy saving ways at consumers' terminal were applied in order to reduce energy consumptions. Such as energy efficient bulbs, smart power strips, energy efficient appliances and HVAC systems. Generally, electric energy is transmitted through the wires, thus some electricity energy is transferred to heat energy. So, wires are the key factor to reduce energy consumptions. Aluminum (Al) and Copper (Cu) are most popular materials used for electric wire according to their excellent electrical conductivity property. New materials with high electric conductivity always attracted researchers to develop in order to improve energy efficient.

<div align="center">1.2 Motivation and Objectives</div>

Carbon nanotube (CNT) has many excellent physical properties, such as strength, electrical conductivity, thermal conductivity (Berber, Kwon, & Tománek, 2000; P. Kim, Shi, Majumdar, & McEuen, 2001; Mintmire, Dunlap, & White, 1992; Tans et al., 1997; Yu et al., 2000). When CNT is mixed with other metal materials, it can improve the physical property of metal matrix composite materials (Mansoor & Shahid, 2016; Mohammed & Chen, 2020; Wang et al., 2019). Researchers did a lot of works for the improvement of material strength. Electrical conductivities of CNTs composites are very few to investigate (Sundaram, Sekiguchi, Sekiya, Yamada, & Hata, 2018).

Electrical conductivity of Al, Cu with CNT composites obviously can be higher than Al and Cu themselves because of the combination with CNTs (Earp et al., 2020; Shin, Choi, & Bae, 2013).

This dissertation is mainly focus on the manufacturing of Cu, Al/CNTs composites from powder to wire. Powder compaction and wire extrusion are used to fabricate Al, Cu/CNTs composites samples and wires in our research lab. Firstly, powder compaction technique is used as the manufacturing process method of Al, Cu/CNT composites samples. Then, wire extrusion is used to produce the wire of Al, Cu/CNTs composites with elevated temperature conditions. In this research journey, some of mechanics behaviors of powder compaction and wire extrusion are investigated comprehensively. Finite element models are used to simulate the manufacturing process of powder compaction and wire extrusion. Some compression tests are run through MTS system for powder compaction and wire extrusion with heater system. Analytical solutions for both powder compaction and wire extrusion are proposed to predict powder compaction and wire extrusion pressure.

For powder compaction, elevated temperature conditions and vibration loading conditions were used to enhance the density ratio and strength of the materials Al, Cu/CNTs composites. Because the relative density ratio is proportional to the electrical conductivity of the material, one can conclude that the electrical conductivity must be relatively low if there are many pores in the materials. The more the pores the material has, the lower the relative density ratio the material owns. Simulation models were used to predict the pressure applied on the powder. Finite element models can simulate the whole process of powder compaction. Drucker-Prager Cap model is used to characterize material constitutive model during the compaction process. Powder compaction tests were run to fabricate samples of the composites and tests results can calibrate the constitutive

model of Drucker-Prager Cap model. For the prediction of the pressure of powder compaction, an analytical solution was proposed in order to predict the extrusion force supplied by MTS system.

For wire extrusion, we used elevated temperature conditions with MTS system to produce Al, Cu/CNTs composites. Finite element models were also used to simulate the whole process of wire extrusion for Al/CNTs, Cu/CNTs composites respectively. An analytical solution was proposed to calculate the extrusion force for some specific material at different extrusion ratios. This is a good way to predict the extrusion force magnitude directly and easily if one can know the material properties. Wire extrusion tests were also run to fabricate the wire samples and validated our simulation models.

The main topics in this dissertation are powder compaction and wire extrusion. As we have known that powder compaction is widely used not only in academy area but also in industry. Wire extrusion is relative to wire drawing, which is also a popular subject for researchers.

1.3 Outline of Dissertation

This dissertation includes 5 chapters. They are Chapter 1 Introduction, Chapter 2 Literature Review, Chapter 3 Powder Compaction, Chapter 4 Wire extrusion and Chapter 5 Conclusion.

Chapter 1 introduces background, motivation and the outline of this dissertation.

Chapter 2 lists a series of paper reviews. The topics of the reviews are composed of powder compaction and wire extrusion. For powder compaction, cold compaction and hot compaction, simulation models and material constitutive models, powder compaction experiments are introduced. For wire extrusion, wire drawing is also introduced to explain the relation with wire extrusion. Simulation models and experiments of wire extrusion are also introduced.

Chapter 3 describes experiments, simulations, material constitutive models and analytical solutions of powder compaction. For powder compaction experiments, die design, experiments instruments, experiments setup, experiments results summaries of Al, Cu/CNT powder compactions, and SEM pictures are investigated. Vibration assisted and elevated temperature powder compactions are run in order to enhance the relative density ratio of materials. For powder compaction simulation model, finite elements models are used to simulate the process of powder compactions. Drucker-Prager cap model is used to build the constitutive model of material. A calibration method is proposed to validate simulation model. Finally, a new analytical solution for powder compaction is proposed to predict powder compaction force magnitude directly. This Chapter's contents were drafted to publish on the Journal of manufacturing science and engineering.

Chapter 4 summarizes simulation models, experiments and analytical solution of Al, Cu/CNT. Wire extrusion tests are run to obtain Al, Cu/CNT wire samples during elevated temperature conditions. Finite element models are used to simulate wire extrusion process, and wire extrusion pressure can be predicted through simulation models. A new analytical solution is developed to predict extrusion force, and it is validated by finite element models and test results. This Chapter's contents has been submitted to Journal of Materials Processing Technology.

Chapter 5 summarizes the conclusions of this dissertation and proposes the future studies. It contains the current research results of powder compaction and wire extrusion for Al, Cu/CNT, and provides some discussion for the future research of powder compaction and wire extrusion.

CHAPTER 2 LITERATURE REVIEW

2.1 Powder Compaction

Powder metallurgy technique attracted many researchers' notice when they were developing the new material because of its advantage (Thümmler & Oberacker, 1993). Ghorbani, Sheibani, and Ataie (2018) fabricated Cu-Cr, Cu-Cr/CNT powders and compressed them to the samples under different temperature conditions. It was found that elevated temperature had a significant effect for the improvement of the material hardness. Rahmani, Majzoobi, and Atrian (2018) used a dynamic compaction method with a modified Hopkinson Pressure bar to achieve the samples with the relative density more than 99%. The results showed that micro-hardness and compressive strength of the samples increased about 70% and 50%. Saboori et al. (2017) produced Al matrix with graphene nanoplatelets by the conventional powder metallurgy. The fabricated nanocomposites showed a high hardness by increasing the compression pressure. Yufeng Wu and Kim (2011) fabricated aluminum alloy 6061 with carbon nanotube composites through Semi-solid powder processing technology. They investigagted the effects of the processing temperature for the fracture surface and hardness of the composites. The aluminum alloy 6061/CNT composites showed a good material densification above 99%. Yim et al. (2017) used the static and shock wave compaction technique to compress CoCrFeMnNi high entropy alloy. The relative density of the sample made by the shock wave compaction reached to 95%, after sintering, to 99.5%. Shokrollahi and Janghorban (2007) summarized a review of the property, characteristics and the applications about soft magetic composite materials. They found that soft magnetic composites were generally manufactured by the powder compaction combined with the warm compaction and two step compactions. Liu et al. (2016) prepared the reduced graphene oxide(RGO) and the graphene nanosheets (GNSs) reinforcement of aluminium matrix nanocomposites (AMCs) through coating.

6

They made use of powder compaction method to manufacutre disc-shaped specimens, and then sintered in the inert atmosphere. The hardness was obviously improved by 32% and 43% respectively for the 0.2 wt.% rGO-Al and 0.15 wt% GNSs-Al composites.

Many researchers investigated powder compaction by combining experiments and simulation models. C.-Y. Wu et al. (2005) used Finite Element Methods (FEM) and Drucker-Prager Cap (DPC) model to investigate the variations of the pharmaceutical powder's relative density with the applied pressure. And the uniaxial compaction experiments were used to calibrate the DPC model. A good agreement between the experimental and the FEA results was achieved, which indicated that FEM model could predict the major features of the powder mechanics behavior during the compaction process. Khoei, Azami, and Azizi (2007) proposed a double-surface plasticity theory to simulate the powder compaction process. The numerical simulations were conducted to well predict the density of the material. Shang, Sinka, and Pan (2012) presented a calibration procedure for the powder compaction simulation. A new die with the radial sensors was designed to help the calibration of the material parameters. Heckel (1961) conducted some powder compaction tests for the metallic materials to obtain the density with the compression pressure curves under 103MPa to 206MPa pressure. The test results provided a relation between the density of material and the punch pressure. Sinka, Cocks, Morrison, and Lightfoot (2000) developed a high-pressure tri-axial testing facility to study the characteristics of the powder compaction, where the density of the specimens was very close to the full density of the material.

Recently spark plasma is one of the most advanced powder compaction methods, which could significantly improve the material density at a very fast speed under the high temperature condition during the powder compaction process. Guillon et al. (2014) reviewed Field-Assisted sintering

technology. They described the working principles and the history background for it. They discussed the refractory materials and the nanocrystalline ceramics and introduced the concepts of the advanced tool. However, the cost of spark plasma instrument is very high compared to that of others. Rothe, Kalabukhov, Frage, and Hartmann (2016) proposed a compressible thermo-visco plastic constitutive model based on the multiplicative decomposition of the deformation gradient for the field-assisted sintering technology. They discussed the required experiments that can help reach to the electrical, thermal and mechanical properties for the materials. They identified the material parameters for this constitutive model. Dash, Ray, and Chaira (2012) compared the maximum Vickers hardness under the conventional and the spark plasma technique for $Cu-Al_2O_3$ metal matrix composites. The maximum hardness is 60, 70 and 80 for Cu-15vol.% Al_2O_3 sintered conventionally in N2, Ar and H2 atmosphere respectively. And the hardness reached to 125 for Cu-5vol.% Al_2O_3 nanocomposites made by the spark plasma sintering technique. The conclusion showed that spark plasma sintering technique had a very good advantage compared to the conventional sintering techniques. Zhang, Li, Yuan, and Peng (2007) investigated hot compression behavior of Al-Mg-Si-Cu alloys under temperature range 350°C-550°C and strain rate range $0.005s^{-1}$-$5s^{-1}$. They ran metallographic and Transmission Electron Microscopy (TEM) tests to observe structural changes. Material flow showed a dynamic flow softening as the results of the dynamic recovery and recrystallization.

For the numerical simulation study of the powder compaction, discrete element method (DEM) and finite element method (FEM) are used to predict the density ratio of the material and study its mechanics mechanism. DEM builds the real material particles to simulate the dynamic process of the powder compaction, which is based on Coulomb friction theory. Garner, Strong, and

Zavaliangos (2018) used the DEM model to investigate the micromechanical characteristics of the powder compaction process. A new adhesive elastoplastic contact model is proposed to define the force displacement characteristics between the contacting particles under the high confining conditions. FEM models based on continuum mechanics also can accurately predict the density ratio of the material. Two widely used constitutive models in FEM are Drucker-Prager model and Mohr-Coulomb model. Cante, Oliver, González, Calero, and Benítez (2013) used the elastic-plastic Drucker Prager model to predict the behavior of the powder compaction, and proposed a set of calibration experiments for the powder compaction simulation model. Bier, Dariel, Frage, Hartmann, and Michailov (2007) used an analytical solution and some instrumented tests to study the relative density ratios of the powder compaction. Most of the above-mentioned models need the extensive experiments data to calibrate the material parameters of the constitutive models. Mamalis, Vottea, and Manolakos (2001) discussed and introduced some theoretical and empirical models under the dynamic powder compaction in order to understand the mechanics mechanism of the powder compaction. Parilak, Dudrova, Bidulsky, and Kabatova (2017) developed a practical compaction equation for the cold powder compaction through running 205 various metal powder mixes, which could give a direct calculation of the compaction force for various powders. Feng, Mei, and Wang (2019) made use of multi particle finite element method (MPFEM) and cohesive zone method (CZM) to simulate the compaction process of Al and NaCl laminar composite powders. The fracture phenomenon of the brittle powder materials was modelled by CZM with the initial cracks. They found that the CZM-based MPFEM could find the internal mechanics mechanism of the powder compaction process. It includes the particle rearrangement, the plastic deformation of Al powder particles and the brittle fracture of NaCl particles.

Recently, a vibration assisted compaction method was proposed as a potential way to improve the material density of the specimen made from the powder compaction under the room temperature condition. This method was widely used to improve the material density for the particle industry in 1960s. An, Xing, and Jia (2014) designed an instrument to investigate the cold compaction of the copper powders with the vibration loading. And they concluded that vibration loading could improve the density and uniformity of the material. Fartashvand, Abdullah, and Vanini (2017) used an ultrasonic vibration method to enhance the density ratio of titanium. It was found that a fine size powder can give an ideal density under the ultrasonic vibration loading. The friction force between the die wall and the powder was reduced through the vibration loading. Majzoobi, Atrian, and Enayati (2015) manufactured Al7075-SiC nanocomposites by the hot dynamic compaction. They obtained the similar conclusion that the relative density ratio of SiC reinforced with Al7075 was slightly reduced by 2%. However, the compressive strength of the material was increased by about 60%.

2.2 Wire Extrusion

Once the material samples were fabricated through powder compaction, after the sintering of the samples, we could use the wire extrusion method to make wires directly. Before introducing wire extrusion method, wire drawing will be discussed. Wire drawing is widely used to manufacture copper (Cu) or aluminum (Al) electric wires in industry. Most of metals, such as Cu, Al and silver (Ag), have a very good ductility that can allow them to employ wire drawing technique to obtain wires. Friction plays a key role in wire drawing process. Friction can result in bad surface qualities for wires. Lowrie and Ngaile (2016) created a stable fluid film between sample and die for the wire drawing process. The friction and the wear of the die were reduced significantly. The fluid

film increased the life of the extrusion die. They also proposed an analytical model to determine the thickness of the fluid film, and to improve the material property of wire made by wire drawing. Strzępek, Mamala, Zasadzińska, Franczak, and Jurkiewicz (2019) used wire drawing method to obtain Cu and Cu/Zn wires under both cryogenic conditions and ambient temperature conditions. They concluded that hardness and uniaxial tensile strength of the material manufactured in the cryogenic conditions are higher than that in the ambient temperature conditions. For the investigation of the mechanics of the drawing process, Wistreich (1955) developed a semi-empirical formula to predict the drawing force, and measured the drawing force, the mean of die pressure and the friction coefficient. The author also discovered a simple relation between tool-stock setup and non-homogeneity of deformation.

When metallic matrix is reinforced by carbon nanotube (CNT), nano composite materials like Cu/CNTs and Al/CNTs would lose a large amount of ductility. Long, Bai, Algarni, Choi, and Chen (2015) validated the fact with both analytical solution and FE model that copper matrix with 4% volume fraction CNTs could improve the strength of composites while decreasing their ductility. Thus, wires made by the wire drawing method would be easily broken during the manufacturing process or after the process due to lack of enough ductility. Otherwise, wire extrusion method is an alternative method with less demand on material ductility. Extrusion can be either cold extrusion or hot extrusion according to the temperature condition of the extrusion die. For cold extrusion, the extrusion die is put in the room temperature condition. For hot extrusion, the extrusion die is in the elevated temperature condition.

Cold extrusion usually needs high energy and large extrusion force to have samples extruded. W Johnson (1956) used cold extrusion experiments to obtain an empirical equation between

compression pressure and area reduction for pure lead. The author concluded that the empirical expression for lead could predict the extrusion pressure with a maximum of 7% error range given a mean yield stress. Friction coefficient is also one of the main parameters for the extrusion process. Wagener (1994) determined partial friction coefficients for the forward bar extrusion, forward tube extrusion and backward cup extrusion under different frictional conditions and various zones and surfaces of the components. Ong, Chin, Ho, and Ng (2018) used response surface method to formulate a nonlinear programming model that can minimize the punch loading during the extrusion process. The fitted function was established for the extrusion force model. They used an analytical approach and other algorithms to optimize parameters of the extrusion process. Dong et al. (2016) used a dynamic material model (DMM) to build the processing map of AA6N01. The processing parameters were obtained through the hot compression tests and was applied on the simulation model. Simulation model was employed to design extrusion dies with different profiles. There is a good match between numerical results and experimental results. Sharififar and Mousavi (2015) employed statistics method and genetic algorithm to optimize the die geometry for fabricating the rectangular waveguides. Effect factors for extrusion force were investigated by using finite element method (FEM) and artificial neural network (ANN). Tang et al. (2018) established a flow line model combined with crystal plasticity method to simulate extrusion process for a magnesium alloy round bar. A polycrystal method coupled with a dynamic recrystallization model was used to investigate texture and microstructure evolution process. They found that side areas had more refined microstructure because of high strain rate. The mechanical property of the material from the side is more isotropic than the central material with less twinning happening during the compression process. Farhoumand and Ebrahimi (2016) employed FEM to investigate the effects of the plastic deformation in the extrusion process. Their axisymmetric

models showed that friction force between die and sample played a key role in the material flow behavior. The strain heterogeneity effect could be reduced by decreasing the friction during the extrusion process. Simulation model had a good match with test results.

Hot extrusion is a very popular way to obtain material with the reduction section area. Materials made from hot extrusion manufacturing method can have a better mechanics property, such as good strength and ductility. Marín, Camacho, and Pérez (2017) employed hot extrusion process to fabricate aluminum alloys. They obtained the loading magnitude and the maximum exit velocity using a FEM model. They concluded that the optimum value of the billet and the die temperature should be obtained in order to get the extruded aluminum products with a good quality. D. Kim et al. (2019) used hot extrusion method to fabricate aluminum 6063/Al-3vol% carbon nanotubes (CNTs)/Al3003 with the tubular shape. This material had a high strength 142MPa and a hardness 120HV and exhibited a high elongation of 22%. CNTs in the middle layer of functionally graded materials (FGMs) helped the contact area to form the improved properties in their tests. Kwon, Estili, Takagi, Miyazaki, and Kawasaki (2009) applied spark plasma sintering method to obtain high densified carbon nanotubes (CNTs) composites. They fabricated aluminum nanotube composite by hot extrusion process. They found that oriented CNT had a good uniformity in the bulk material. Composites exhibited a tensile strength close to 200MPa. L. Chen, Zhao, Yu, and Zhang (2015) investigated plastic deformation behavior of 7075 aluminum alloy during hot extrusion process from 623K to 823K and strain rate from 0.001/s to 10/s. Numerical simulations and experiments were performed in their study. They showed that simulation model could predict 7005 aluminum alloy material's behavior for the extrusion process.

Numerical simulations can provide much more insights than experiments can directly measure.

Reddy, Sethuraman, and Lal (1996) combined upper bound method and finite element method for axisymmetric dies. Billet was modelled as a visco-plastic rate sensitive material. The flow stress of the billet material depended on strain rate and temperature. Four die shapes (stream lined, cosine, hyperbolic and conical shapes) were studied in the combined upper bound and finite element method. They concluded that optimal strength of the die decreased with friction coefficients and increased with reduction ratio and ram velocity. The power during extrusion process was the lowest level for the stream lined die. Hosseinabadi and Serajzadeh (2014) developed a thermo-mechanical model for hot extrusion process. Extrusion pressures with temperature variations were predicted by employing a coupled upper bound-finite element method. Force displacement curves under different conditions were compared between experiments and simulation models for AA6061-10%SiC$_p$ composites. Results showed that they had a consistent agreement between test and simulation. Hansson and Jansson (2010) performed a sensitivity analysis through a finite element model for stainless tubes. The results showed that billet temperature was the most important factor for extrusion force. Bressan, Martins, and Button (2015) used finite volume method to perform metal plastic flow analysis for aluminum alloy 6351 under axisymmetric hot extrusion condition. Finite volume method and finite element method had good matches for velocity field results. Flitta and Sheppard (2005) investigated the evolution of the temperature from upside to bottom of samples. They used finite element code FORGE2 to simulate the extrusion process. They found that temperature gradient significantly influenced friction and heat transfer of the extrusion parameters. Chanda, Zhou, and Duszczyk (2001) used a 3D finite element model to compare the iso-speed extrusion and the isothermal extrusion of 6061 Al alloys. They showed that stepwise ram speed reduction can make the extrudate to attain a steady value. Temperature can monotonically increase with a constant ram speed. Increasing average ram speed

14

can increase productivity for the extrusion of material. A low ram speed can reduce extrusion pressure. Qamar, Chekotu, and Qamar (2019) investigated the effect of profile, metal flow property and material defects on the extrusion pressure. They performed simulation model through the finite element package DEFORM-3D. They found that higher complexity of the profiles would result in the worse material property and need much more extrusion energy. Extrusion area ratio and symmetric die profile play a key role on the metal distortion process.

Regarding analytical solutions of the extrusion force, the classical slip line theory, the upper bound and the slab methods were widely used to predict the extrusion pressure. Abrinia and Mossuleh (2009) presented a loading prediction method based on the slip line field theory for three dimensional axisymmetric problems. This method was used for forward extrusion of the round billets. They concluded that new formulations had good agreements compared with the experiment, the simulation and other analytical methods. Altinbalik and Onder (2013) investigated effects of the die inlet and transition geometry for extrusion force through upper bound theory and experiment method. They analyzed different shapes of clover sections for round bars. The theoretical analysis for different inlet-die transition geometries was consistent with the experiments results. Gordon, Van Tyne, and Sriram (2002) developed an upper bound solution for a spherical die. This solution contained equations for the velocity and the strain rate fields in order to predict the power of the deformation, the power losses and the friction power losses. Model can determine the optimal die curvature that minimizes the extrusion pressure of spherical die. Fiétier, Krähenbühl, and Vialard (2009) presented two programs that can help extruders to estimate feasibility and performance of extrusion processes. They can be used for aluminum alloys, other metals and polymers extrusion applications, which can accelerate the process of die design. W.

Chen, Davies, Samarasekera, Brimacombe, and Hawbolt (1996) adopted an integrated method including experiments, extrusion plant trials and finite element models to investigate the extrusion of metal matrix composites (MMCs) 6061/Al2O3/20p. An updated Lagrangian formulation was modelled for both transient and steady regions of the extrusion. Loading and temperature predictions from this model had good matches with test results. Prediction results of models revealed that large shear deformation promoted the particle fracture. The tensile stress led to the low-speed cracks of the material during the extrusion process.

Some other unique extrusion methods were also investigated in order to improve the material property. Zeng, Stanford, Davies, Nie, and Birbilis (2019) wrote a review of the developments and prospects of the extruded Mg alloys. They described the recent progress for the magnesium extrusion alloys, the advances of the mechanical properties and the microstructural characterization. Shatermashhadi, Manafi, Abrinia, Faraji, and Sanei (2014) proposed a new backward extrusion method. The die set up was composed of the fix-punch, the moveable punch and the die in their new method. They showed that the loading in the new method was less than 25% of that in the original backward process. The new method improved the homogeneity of the sample and produced the extreme fined samples due to the high level of the shear strains. Z. Chen, Ikeda, Murakami, Takeda, and Xie (2003) developed a multi-billet extrusion fabricating method to make the clad composites. This method was to combine several solid samples using the welding chamber to extrude one sample with different material layers through the extrusion die. They showed that the extrudates can be fabricated under different mixing ratios of zirconia and stainless steel powders. Yang Wu et al. (2019) fabricated the copper billet with high yield strength of 462 MPa and the refined grain size was from 50 to 0.8μm through a new method called repetitive

extrusion and free forging (REFF). The copper billets exhibited a good ductility of 8.3%. Zaharia, Comaneci, Chelariu, and Luca (2014) used a combined process of extrusion followed by the upsetting test of the cylindrical load. The extrusion process can elongate the grains of the aluminum sample. They ran the upsetting test for the sample after extrusion. The tensile stress of the sample after four times extrusions was enhanced about 50% to 180MPa than that of the sample after one extrusion procedure. Kazanowski, Epler, and Misiolek (2004) investigated the influence of initial billet geometry for a bi-material extrusion process.

CHAPTER 3 POWDER COMPACTION

3.1 Powder Compaction Die Design

Powder compaction die is a container that can constrain radial motion of the powder. After one specific force applied on the top of the powder, a sample could be obtained. The powder compaction die assembly is composed of die, base and punch. Figure 2 shows powder compaction die.

(a)   (b)

Figure 2. Powder compaction dies (a) rectangular die, (b) cylindrical die.

Powder compaction die need resist the pressure from both the axial direction and the radial direction during powder compaction process. The axial pressure applies on the die base and the punch, and the radial pressure applies on the die. The axial pressure magnitude is generally bigger than the radial pressure magnitude, unless it is the hydrostatic pressure condition, they are equal. The material strength of the die and the punch should be checked before design. An easy machinable material AISI 1144 carbon steel is selected as the die material. Its maximum yield strength reaches to 689MPa.

Two new powder compaction dies are designed and manufactured for powder compaction in order to resist the high strength and high temperature conditions with the above mentioned AISI 1144 carbon steel. One diameter of them is 6.4mm, another one is 13mm. The physical picture of the two dies is shown in Figure 3. Figure 4 shows the drawing of die with diameter 9.6mm.
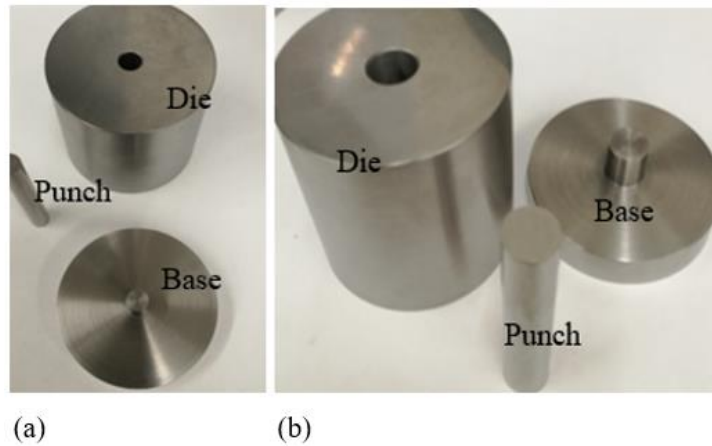
Figure 3. Physical picture of dies (a) Diameter=6.4mm, (b) Diameter=9.6mm.
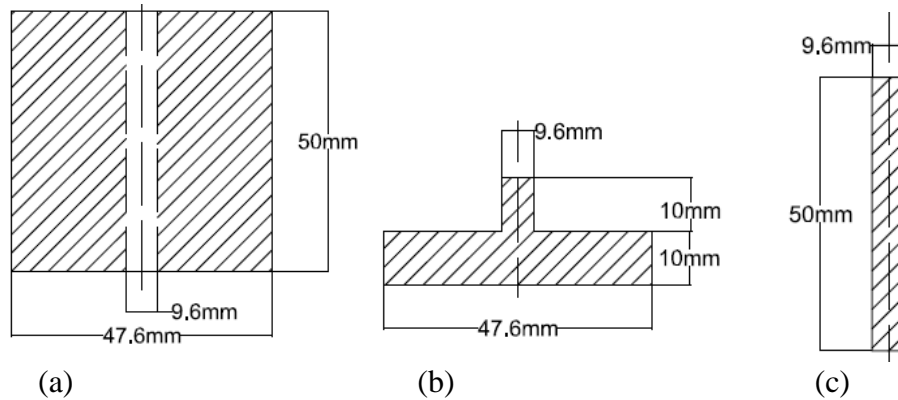
Figure 4. Drawing of die assembly with diameter 9.6mm (a) Die, (b) Base (c) Punch.

3.2 Powder Compaction Test Setup

There are two commercial powder compaction test systems available to run tests. One has the capacity of 30ton force, the other one has the capacity of 10ton force, and there are two types of

commercial dies. One can make rectangular aluminum sheet, another one can make aluminum cylinder solid. Figure 5 shows commercial powder compaction test system. But these two compacting machines can not provide detailed information about force and displacement during compaction tests. They are not easy to add heater system. MTS system can solve this problem, Figure 6 shows new powder compaction test setup.

(a)   (b)
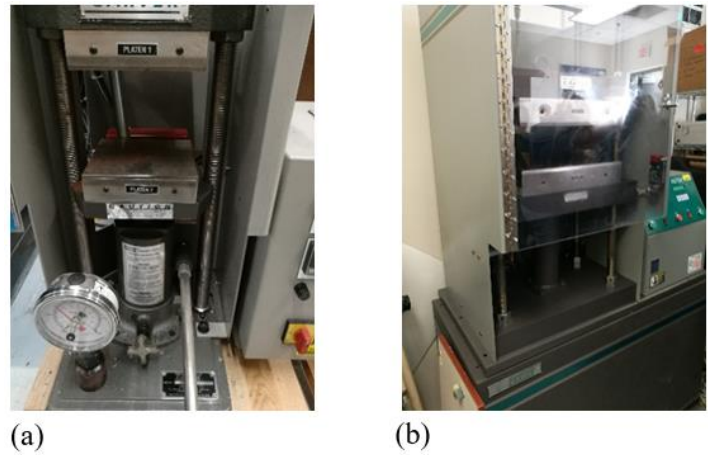
Figure 5. Commercial compacting hydraulic machine (a) 10-ton capacity, (b) 30-ton capacity displacement.

(a)   (b)
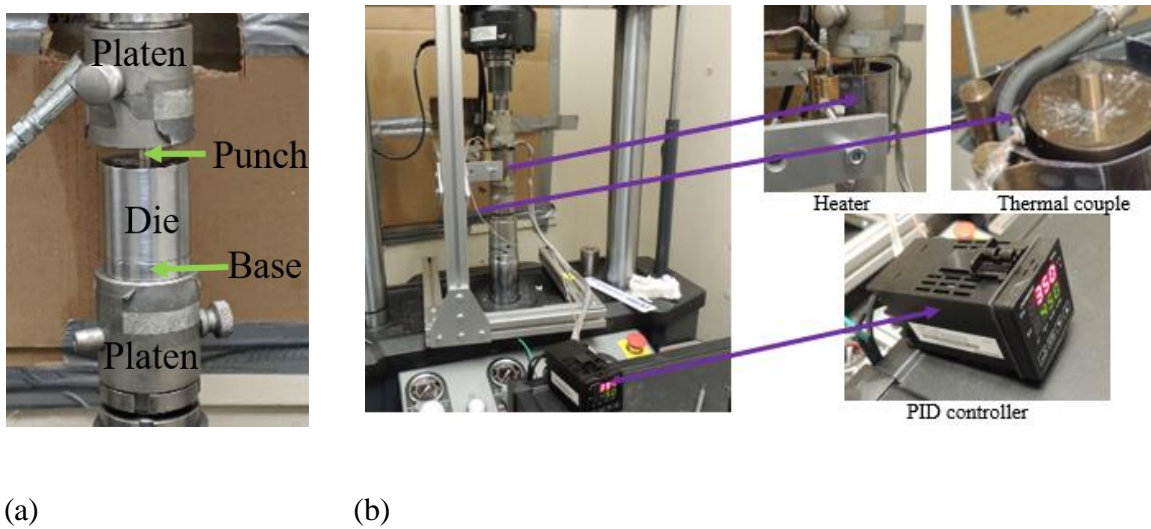
Figure 6. Powder compaction test setup (a) Cold compaction test setup, (b) Hot compaction test setup.

Powder compaction tests were conducted in MTS system. MTS system is a hydraulic system. It can supply the maximum force magnitude 100kN. MTS system is used to provide the pressure source for powder compaction test. Die assembly was put on the grip of the compression test, after powder is put into the hole of the die, then MTS system applies pressure on the punch. Test system contains die, upper punch, lower base and powders.

For hot compaction tests, an extra induction heater was put around the die. Figure 5 (b) shows the setup of the hot compaction test. The heater device is composed of a heater, a PID controller and a thermal couple. The heater model is HBA-202040. The diameter and the height of the heater are 50mm×50mm. It is just suitable for the size of the powder compaction die. Thus, heat energy is easily transferred to the die. Because there is only a little space between the heater and the die. PID controller (CN470) is used to control the temperature of the die. The thermal couple is a type K washer thermal couple.

3.3 Powder Compaction Tests

Aluminum powder compaction tests are ran in the MTS system, test setup is shown in Figure 6-(a). Aluminum powder product information is shown in Table-1 and Figure 7 is a SEM image of aluminum powder, which tells the irregular particles shapes and different sizes.

Table 1. Aluminum powder information

Product number	11067
CAS number	7429-90-5
Melting point	Melting point:660ºC
Particle size	APS 7-15 micron
Mesh	325 mesh, 99.5% (metal basis)
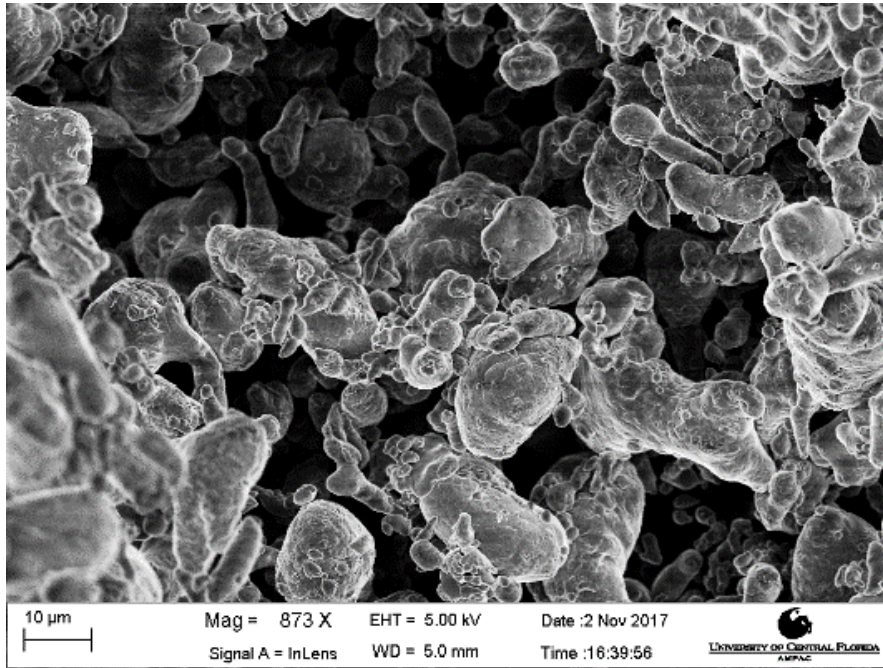
Figure 7. Aluminum powder SEM picture.

3.3.1 Aluminum Powder Compaction Test with Die of Diameter 6.4mm

Powder compaction tests was done with the die of the diameter 6.4 mm. The pressure on the punch was 481MPa, the mass of aluminum powder is 1g, and the mass of the specimen after compaction is 0.913g. In this test, force control mode is used to apply pressure. This method is easy to control the whole test process, because the displacement control mode is easy to harm the MTS system if the force amplitude is out of the range of MTS system force sensor. The pressure on the punch will hold for 5minutes after pressure reached to the objective value 481MPa.

The aluminum sample is shown in Figure 8 after powder compaction. SEM pictures are shown in Figure 9. The summary of aluminum powder compaction is shown in Table-2.

Figure 8. Aluminum sample with diameter 6.4mm.

(a)

(b)

(c)

(d)

(e)

(f)
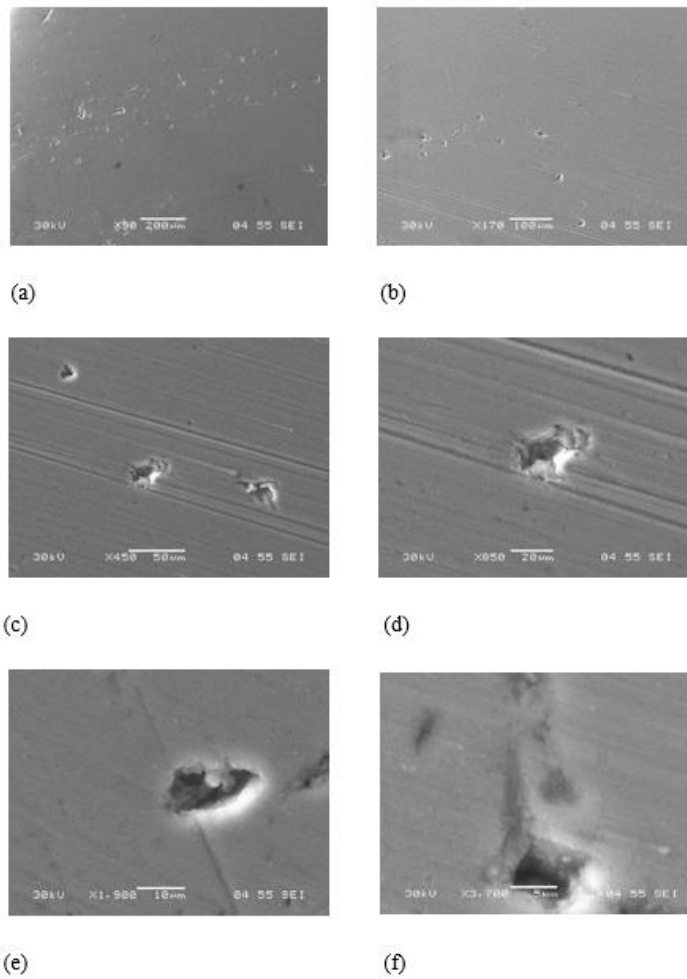
Figure 9. Scanning electron micrograph (a) 90X, (b) 170X, (c) 450X, (d) 850X, (e) 1900X, (f) 3700X.

Table 2. Aluminum sample information summary

Aluminum powder	Die with diameter 6.4mm
Pressure (MPa)	481
Height(mm)	11.32
Diameter(mm)	6.35
Mass(g)	0.913
Density(g/cm^2)	2.54
Relative Density	0.94

From Table-2, the relative density is 0.94. There is still a difference compared with the relative density ratio 1. Figure 8 also shows the same conclusion. There are still some pores in the section of the aluminum billet.

3.3.2 Powder Compaction Test with Die of Diameter 9.6mm

The force control mode of MTS system was used to apply the compression pressure onto the powder. It is helpful to protect the universal test system away from the damage. A maximum force of 10kN was applied on the aluminum powder for the cold compaction test. The powder mass is 0.427g. After the maximum force was reached, the compression pressure was hold on for 300 seconds. This hold action is useful to make the quality of the specimen better. The initial and final powder geometry sketches are shown in the following Figure 10.

(a)	(b)
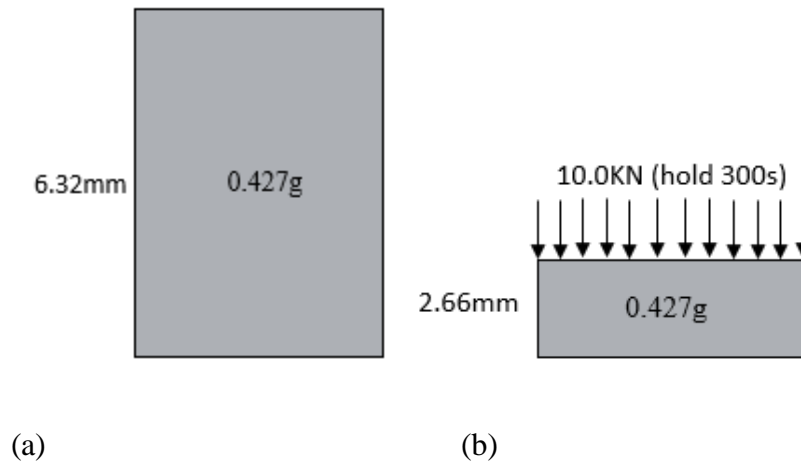
Figure 10. Sketches of cold compaction test. (a) Initial status, (b) Final status.

3.3.3 Hot Compaction Test

For hot compaction tests, the aluminum powder mass is 0.445g, and the compression force is also

10kN. The temperature of the die was steadily increased by heater. After 2 hours, it reached to 300°C.

The maximum compression pressure is 140MPa. The hold time is also 300s. After unloading MTS

system and turn off the heater, the die and the specimen cooled down gradually. One interesting

thing is that the specimen was not easily separated from the compression punch because of the

surfaces glued between the specimen and the punch. This phenomenon shows that the elevated

temperature is obviously useful to make the atoms move dramatically. Thus, the interfaces bonded

perfectly. The initial and final powder sketches are shown in Figure 11. The cold and hot compaction

test data are summarized in Table 3.
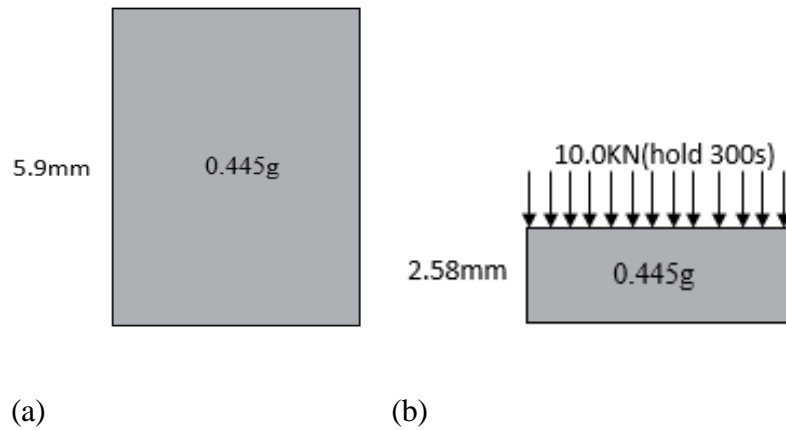
Figure 11. Sketches of hot compaction test. (a) Initial status, (b) Final status.

Table 3. Test data of specimens for both cold and hot compaction tests

	Cold powder compaction (Room temperature)	Hot powder compaction(300°C)
Force(kN)	10	10
Mass(g)	0.427	0.445
Height(cm)	0.266	0.258
Diameter(cm)	0.96	0.96
Volume(cm^3)	0.192	0.186
Density(g/cm^3)	2.22	2.39
Initial Relative Density Ratio	0.35	0.38
Compaction Pressure (MPa)	140	140
Relative Density Ratio	0.82	0.88

From Table 3, one can conclude that the density ratio of the specimen made from the hot powder compaction is larger than that made from the cold powder compaction (from 0.82 to 0.88) under the same compaction pressure. Thus, the elevated temperature compaction test is one effective way to enhance the density ratio for the aluminum powder compaction.

3.4 Vibration Assisted Compaction Test

For the vibration assisted compaction test, the force control mode in MTS testing machine was used. The loading histories of the quasi-static loading (or called monotonic loading) and the vibration

assisted one are shown in Figure 12. The individual and the combined force-displacement curves are plotted.
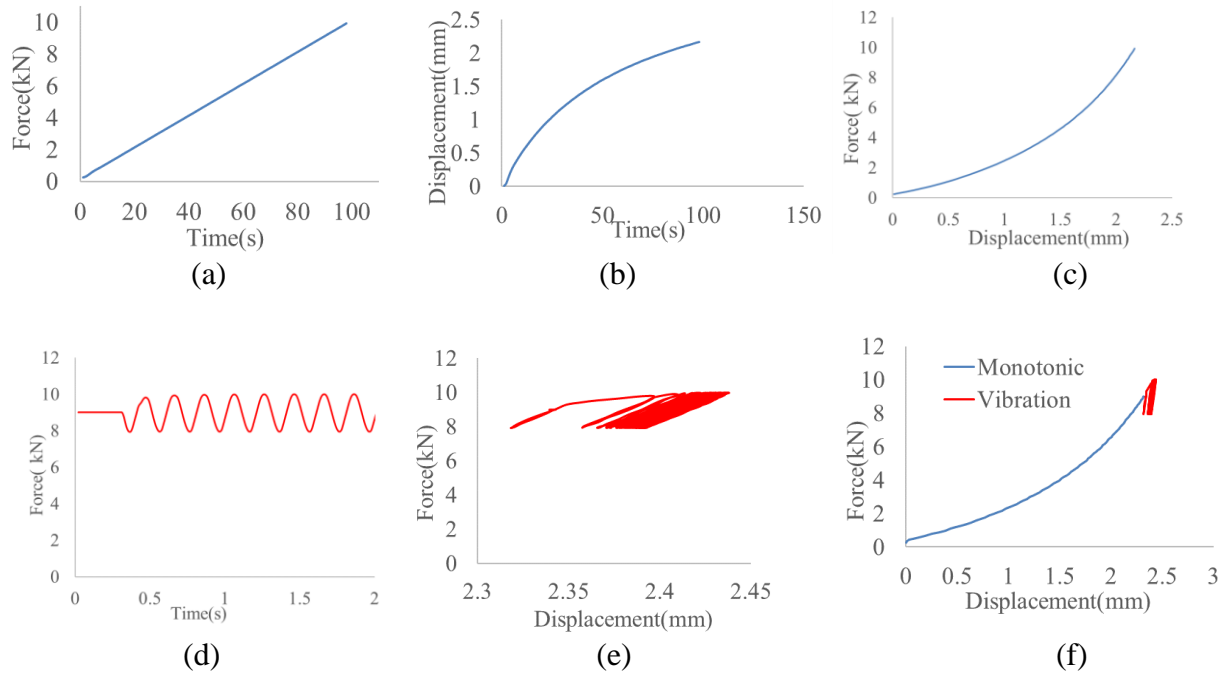
Figure 12. Force and displacement curves of quasi-static loading (first 100 sec) and vibration loading (fist 2 sec) for the first group test. (a) Force with time of quasi-static loading, (b) Displacement with time of quasi-static loading, (c) Force with displacement of quasi-static loading, (d) Force with time of vibration loading (5Hz), (e) Force with displacement of vibration loading (5Hz), (f) Force with displacement of both of the quasi-static loading and the vibration loading (5Hz).

Different loading conditions were programmed with MTS system, using the force control mode. For the four groups of quasi-static and vibrations tests, the following factors were considered, force amplitude, powder mass, quasi-static loading pressure, vibration loading pressure and dwell time of the powder compactions. Each group of tests contains 2 or 3 tests of vibration and/or quasi-static loading. Although the relative density ratio did not change very much under the vibration loading condition compared to the quasi-static loading condition, the strength of the specimen

27

compacted under the vibration loading condition is higher than of that made from the quasi-static loading condition. This part will be described in detail in the following section 2.2.4 and 2.2.5. The following paragraphs will introduce these four groups of tests and a summary of the loading tests data (see Table-4).

The first group of tests are the 10kN quasi-static loading and the 9kN quasi-static force with 1kN vibration force. For the vibration loading condition, the vibration frequency is 5Hz, and the dwell time are all 300 seconds. The mass is 0.427g for the quasi-static loading, and the mass is 0.543g for the vibration loading. The relative density is 0.82 for the quasi-static test. The relative density is 0.82 for the vibration test. It seems that they have almost the same density ratio. The vibration effect on the powder compaction is not obvious. The reason may be that the current vibration amplitude and frequency are not enough to improve the density of the powder compaction. Thus, for the second group of tests, the vibration frequency and amplitude were enhanced to 5kN and 20Hz. This means that more energy from the vibration loading were applied on the powder.

For the second group of tests, three tests were done. They are the quasi-static loading 14kN. The quasi-static loading 9kN with the 5kN vibration loading with 10Hz frequency, and the quasi-static loading 9kN with the 5kN vibration loading with 20Hz frequency. The dwell time are all 300 seconds. The quasi-static loading 14kN represented 128MPa pressure. The vibration force represented 72MPa pressure. The final mass of the powder is 0.53g, 0.36g and 0.329g, respectively. The relative density ratio of the specimens are 0.87, 0.89 and 0.91. It seems that the powder with the vibration loading with frequency 20Hz have a better relative density. But the real force amplitudes for the two vibration loadings are bigger than the input value (14kN). They have the same input total force value 14kN (9kN+5kN). But MTS system generated a different bigger

force value 16.4kN instead. The relative density for the quasi-static force 9kN with the vibration frequency 10Hz is higher than that of the quasi-static loading obviously.

For the third group of tests, the quasi-static force is 16.5kN, and the vibration force is the quasi-static force 9kN and the 7.5kN vibration force with the vibration frequency 20Hz. It means a 127 MPa quasi-static pressure and a 106MPa vibration pressure. The final masses of the powder are 0.257g and 0.264g, respectively. The dwell time is 1800s in this test in order to verify the time effect for the relative density. Eventually the relative density did not improve.

For the fourth group of tests, the quasi-static loading is 10kN, and the vibration loading is 9.8kN quasi-static loading with 0.2kN vibration force with a vibration frequency of 10Hz. The quasi-static compression pressure is 130MPa, and the vibration compression pressure is 3MPa. The powder masses are 0.973g and 0.965g, respectively. The purpose of this group of tests is to investigate the effect of the powder mass. The two tests have almost the same mass. The dwell time is also 300s. The relative density of the specimen with the vibration loading is a little bit higher than of the specimen without the vibration loading. They are 0.76 and 0.77, respectively.

Table 4 gives a summary of the aluminum powder compaction tests from both the quasi-static loading and the quasi-static force with vibration force. The hot compaction test data is also included. Figure 12 shows the relative density ratio of the aluminum powder under different loading conditions. From Table 4 and Figure 12, the relative density ratios did not improve dramatically under the vibration loadings in the current aluminum powder compaction tests. This does not mean that the vibration loading can not enhance the density of the material. In fact, a higher frequency for the vibration loading may be helpful for the improvement of the density ratio. The capacity of the vibration frequency in our MTS machine is very limited, which is one of the

reasons that the relative density ratio was not improved. The dwell time may be also another reason.

Table 4. Summary of aluminum powder compaction tests

Test number	Force and loading condition	Mass (g)	Density (g/cm^3)	Relative Density	Static Pressure (MPa)	Vibration Pressure (MPa)	Dwell Time (s)
1	10kN+300°C	0.445	2.39	0.88	140	0	300
2	10kN	0.427	2.22	0.82	140	0	300
3	9kN+1kN+10Hz	0.543	2.20	0.82	124	13.8	300
4	14kN	0.53	2.29	0.85	197	0	300
5	9kN+5kN+10HZ	0.36	2.35	0.87	128	72	300
6	9kN+5kN+20HZ	0.329	2.39	0.89	137	95	300
7	16.5kN	0.257	2.37	0.88	233	0	1800
8	9kN+7.50kN+20HZ	0.264	2.34	0.87	127	106	1800
9	10kN	0.973	2.01	0.74	141	0	300
10	9.8kN+0.2kN	0.965	2.05	0.76	138	3	300
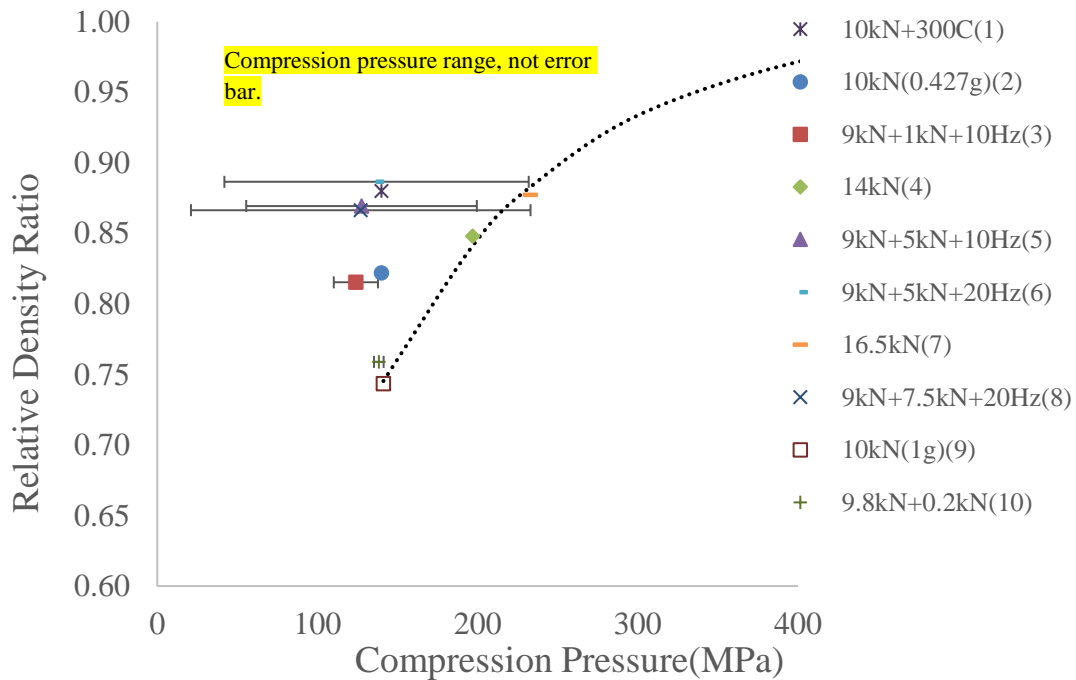
Figure 13. A diagram of the relative density ratios for the compacted samples under different loading conditions. A curve fitting based on maximum pressure is provided. The number displayed in the parentheses above the figure is the test number in Table 4.

3.5 SEM Pictures of Compacted Samples

For the loading 14kN quasi-static force and the loading 9kN quasi-static force with 5kN vibration loading with 10Hz frequency, SEM images are shown in Figure 14. SEM images can provide micro structural information of the specimen. The dark area is the pore in the section of the specimen. The darker areas the specimen had, the smaller the density ratio of the specimen became. From Figure 14, the dark area of the specimen section in the quasi-static loading is more than that of the specimen section in the vibration loading. Thus, the relative density ratio under the quasi-static loading is smaller than the one under the vibration loading at the observed spot. Image analysis shows that the ratio of the dark area to the white area under the quasi-static loading is 6.2%, and that under the vibration loading is 5.5%. From SEM pictures, the difference of the density between the quasi-static and the vibration loading has the same conclusions as the direct measurement. See Table 4. Another observation is that the void/pore description is more uniform in samples made from vibration compaction.
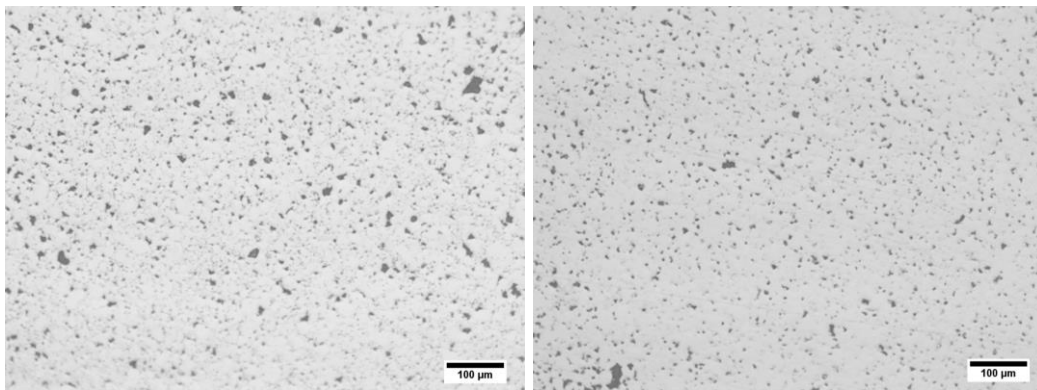
(a)   (b)

Figure 14. SEM images of compacted samples. (a) Quasi-static loading, (b) Vibration assisted loading.

3.6 Mechanical Strength Tests of Compacted Specimens

Two group of compression tests were conducted to compare the strength of specimens. The specimens for Group 1 were compacted with the maximum force 16.5kN. The test setup is shown in Figure 15, which is the radial compression. One specimen was made from the vibration loading, and the other specimen was made from only the quasi-static loading. Figure 15 shows the force vs. displacement curves of the two specimens. It is found that the specimen made from the vibration compaction has a better strength than that made from the quasi-static loading. However, their density ratios are almost the same.
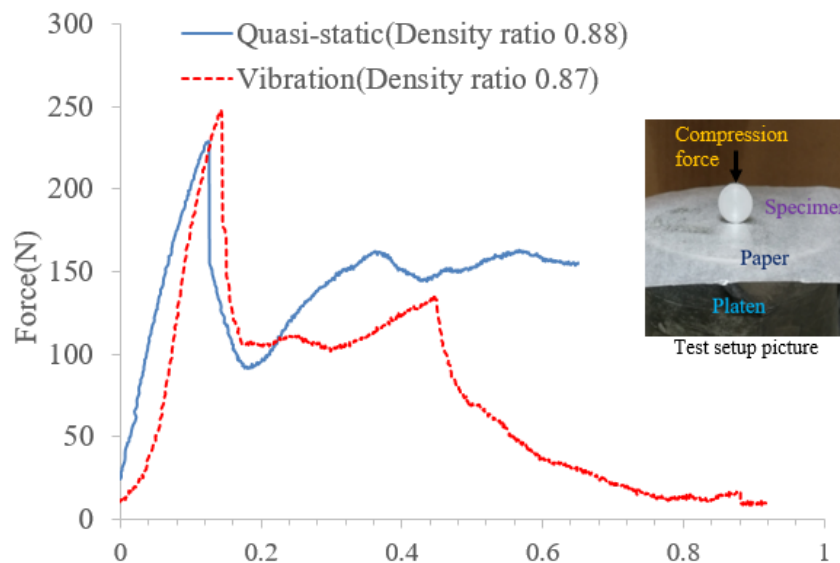
Figure 15. Comparison of force-displacement curves between quasi-static compaction and vibration assisted compaction samples from radial compression tests.

The specimens for Group 2 are compacted with the maximum force 10kN, namely the quasi-static loading force 10kN and the quasi-static loading force 9.8kN with the vibration loading 0.2kN force. Figure 16 shows the specimen deformation after the compression test in the MTS machine. This setup picture is different from the Figure 15, it is a radial compression test. Figure 16 is an axial

compression test. Both the strength comparison of the specimens and the strain-stress curves under the axial compression loading are illustrated in Figure 16.

It is found from Figure 16 that the strength of the specimen compacted under the vibration loading is higher than that of quasi-static loading. The maximum force magnitude is increased from 4000N to 4500N for the specimen made from the vibration compaction. Accordingly, the maximum stress magnitude is increased from 55MPa to 65MPa.
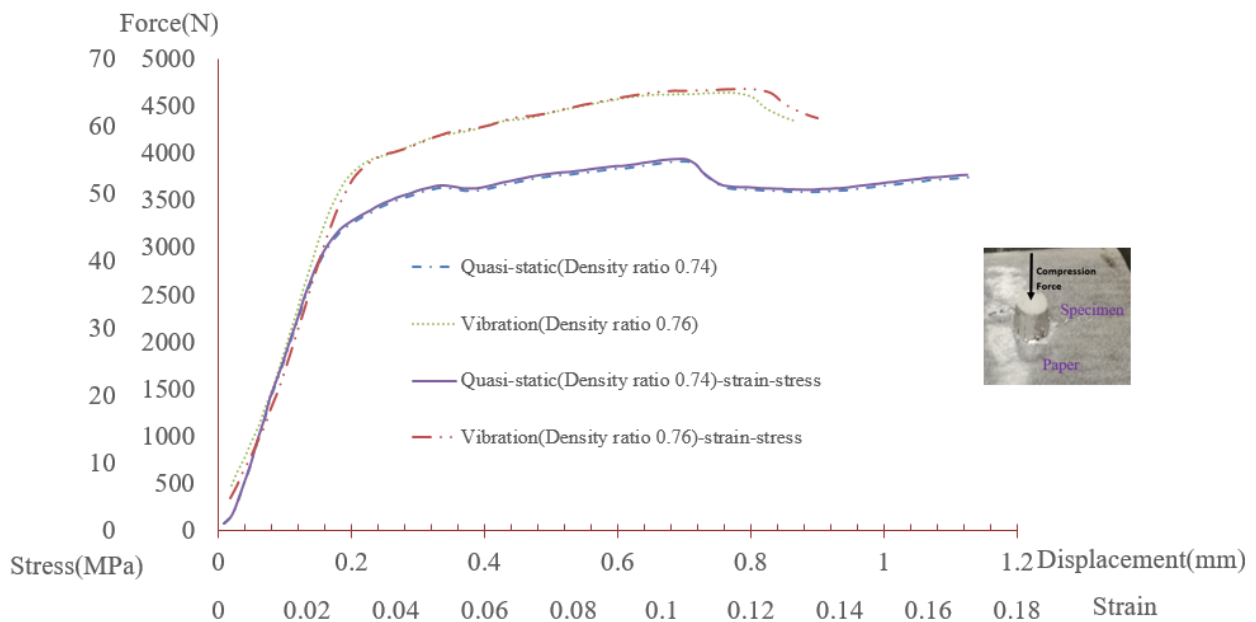
Figure 16. Strength comparisons of the compacted samples between quasi-static loading and vibration assisted loading from axial compression tests. Both force-displacement curves and engineering stress-stain curves are provided.

3.7 Nickel/CNT, Cu, Cu with Nickel/CNT Powder Compaction

Cu, Nickel/CNT and Cu with Nickel/CNT powder compaction tests are run in order to manufacture samples. Nickel owns high melting point, highly ductile and resists corrosion and oxidation property. Nickel is used to coat carbon nanotubes because of its hardness and corrosion characteristics (Sung-Kyu & Tae-Sung, 2011). Carbon nanotubes are coated with Nickel in order

33

to distribute uniformly.

Two volumetric fractions of CNTs are manufactured in order to compare the difference. One is 2%, the other one is 4%. 6 powder compaction tests are ran. They are 4 Nickel with CNT tests, 1 Cu test, 1 Cu with Nickel and CNT test. For Nickel with CNT recipe-4-2 specimen, specimen is not good. It deformed because of fracture. Table 5 shows the detailed data summary. Nickel/CNT mass fraction is 7.15% for Cu, Nickel/CNT test.

Table 5. Powder compaction data summary

Powder	Die diamter(mm)	Mass(g)	Force(N)	Pressure(Mpa)	Height(mm)	Density(g/cm^3)
Nickel-CNT-Recipe-4-1	9.570	0.286	36000	500.7	1.218	3.264
Nickel-CNT-Recipe-5-1	6.400	0.120	20000	622.0	1.059	3.533
Nickel-CNT-Recipe-5-2	6.400	0.157	20000	622.0	1.551	3.138
Cu	9.600	2.197	40000	552.9	3.935	7.717
Cu,Nickel/CNT	9.583	1.245	40000	552.9	2.197	7.861

For Nickel with CNT recipe-4-2 specimen, specimen is not good, it deformed because of fracture. For Table 5, Nickel-CNT-Recipe-4 volume fraction is 4%; Nickel-CNT-Recipe-5 volume fraction is 2%. Figure 17 shows Cu, Cu-Nickel-CNT and Nickel-CNT powder compaction tests curves.
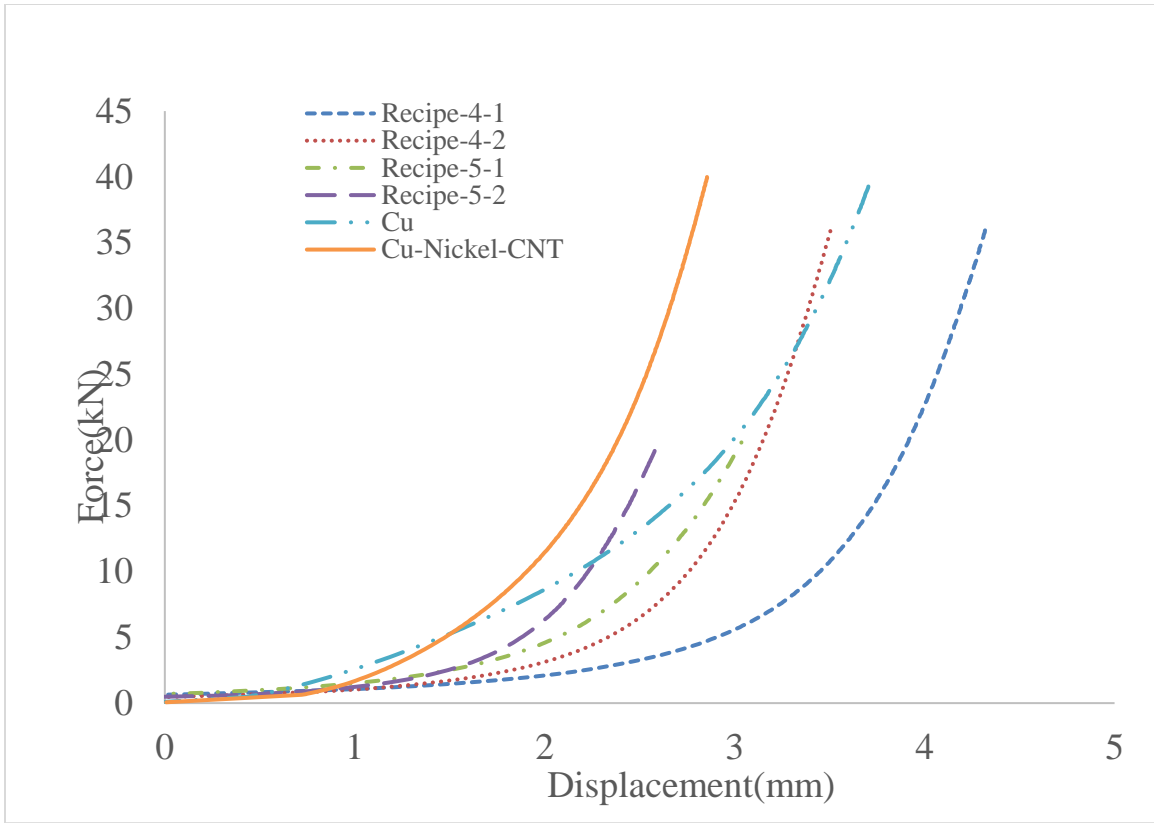
Figure 17. Cu, Cu-Nickel-CNT and Nickel-CNT powder compaction tests.

For density calculation of composites, the following equation is introduced to calculate (M. Zhou et al., 2017).

$$\rho_t = \frac{W_{total}}{V_1+V_2+\cdots+V_n} = \frac{W_{total}}{\frac{W_1}{\rho_1}+\frac{W_2}{\rho_2}+\cdots+\frac{W_n}{\rho_n}} \tag{1}$$

ρ_1 is the individual density of the material, and W_1 is the individual mass of the material.

Ni/CNTs sample's SEM pictures are shown from Figure 18 to Figure 21. Figure 22 and Figure 23 are Recipe 5 and Recipe sample pictures. Recipe 5 powder is compacted in the die with diameter 9.6mm. Recipe 4 powder is compacted in the die with diameter 6.4mm.
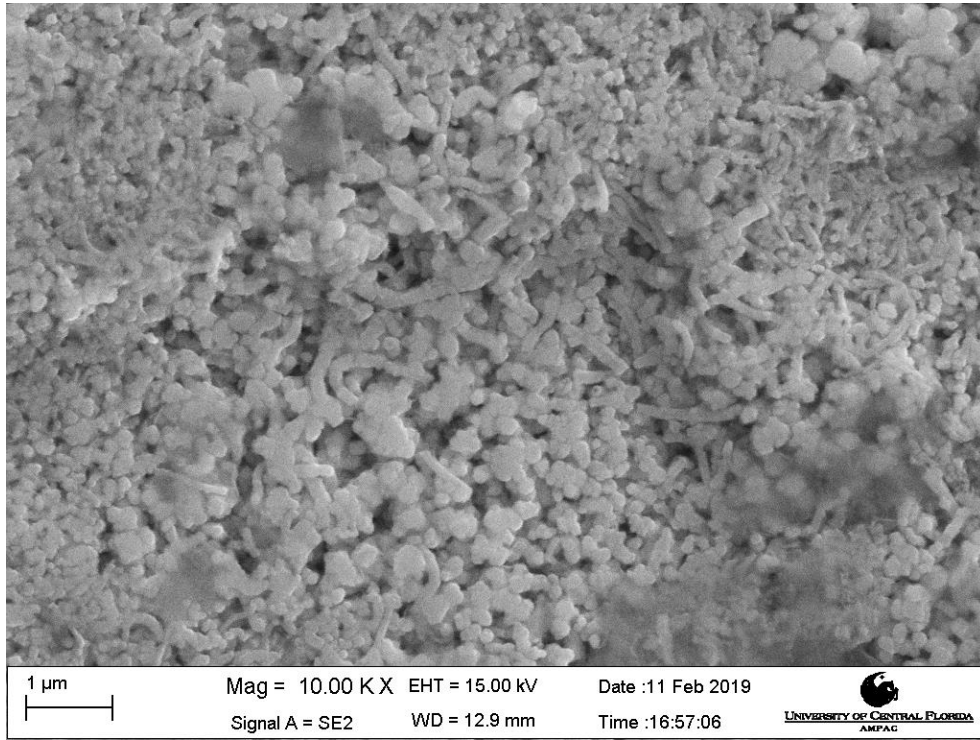
Figure 18. Recipe 5 SEM picture (10KX).
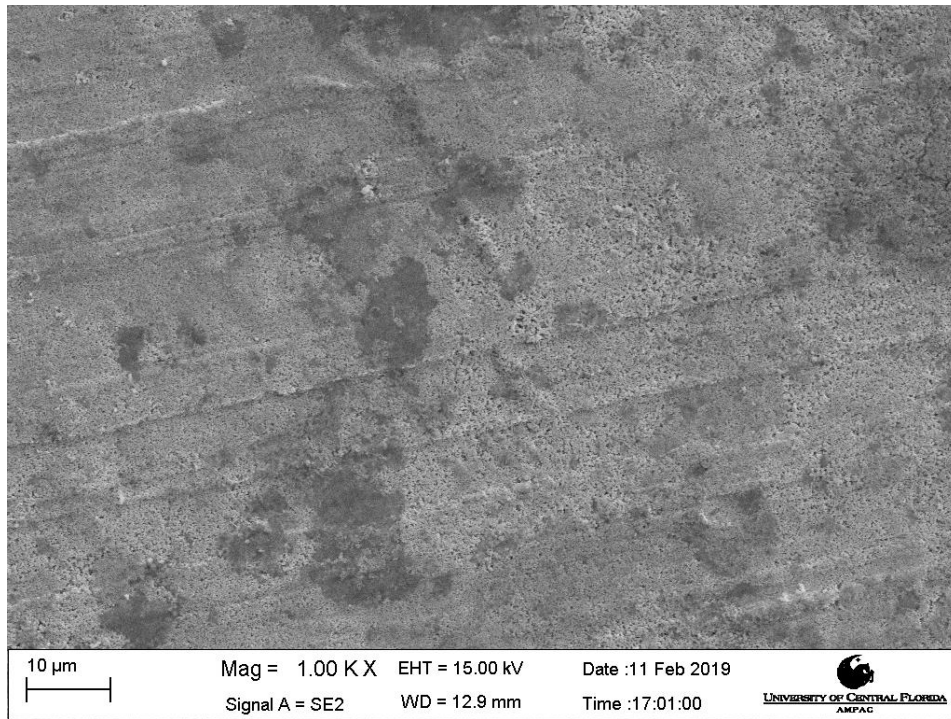
Figure 19. Recipe 5 SEM picture(1KX).
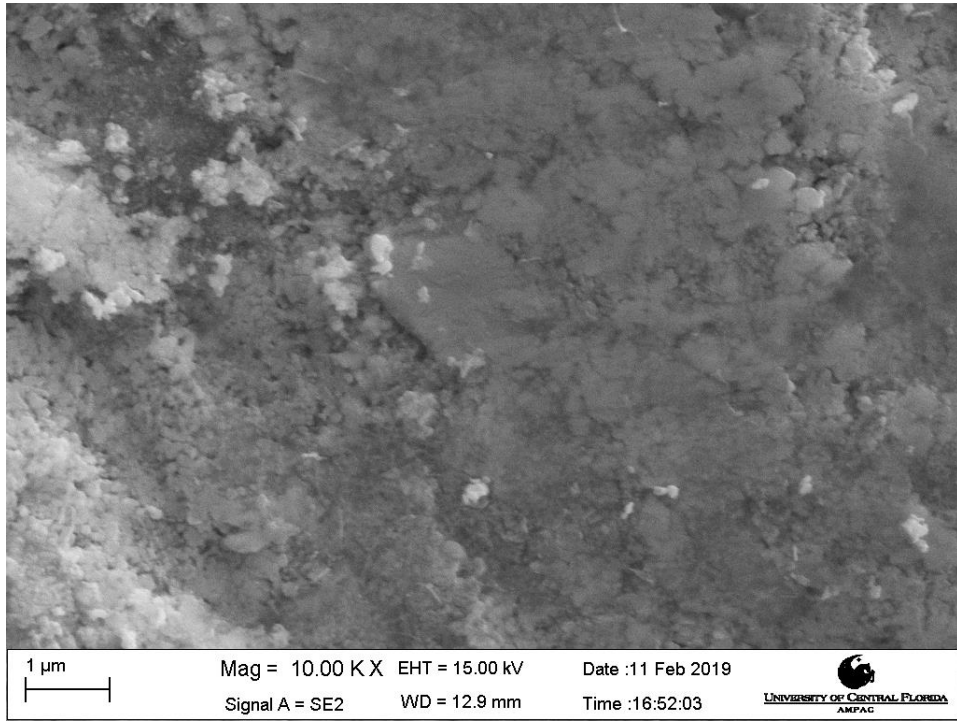
Figure 20. Recipe 4 SEM picture(10KX).
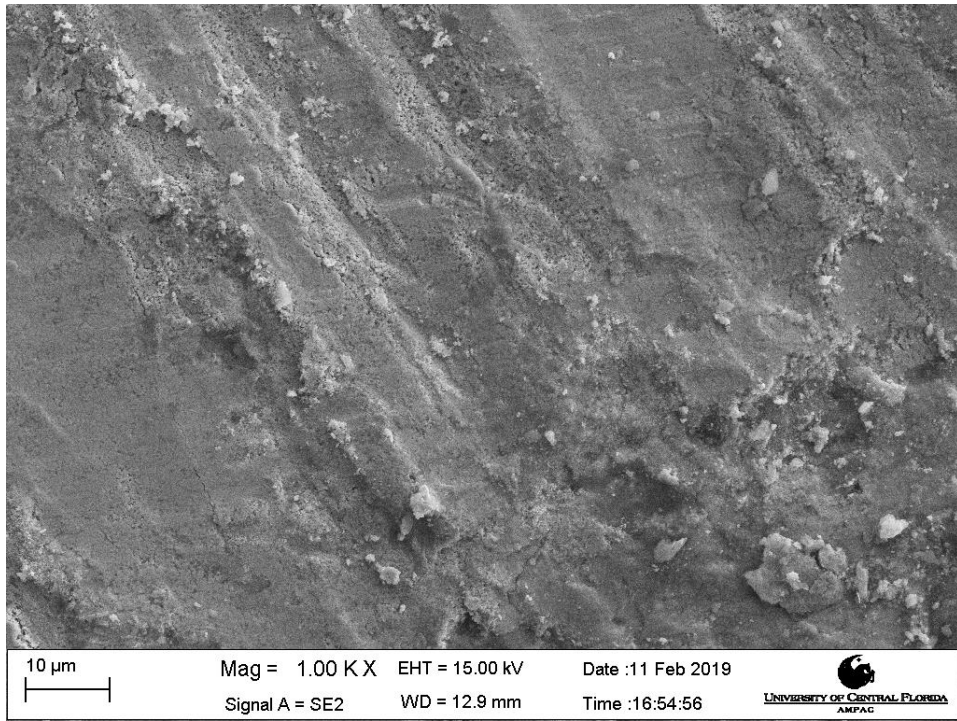
Figure 21. Recipe 4 SEM picture(1KX).
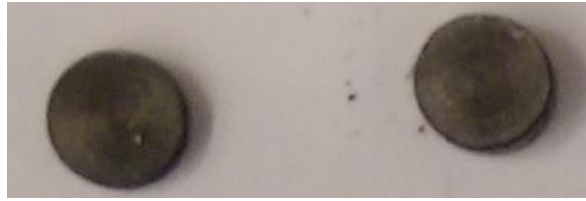
Figure 22. Recipe 5 sample.

Figure 23. Recipe 4 sample.

Cu-Ni/CNTs sample and SEM pictures are shown in Figure 24 to Figure 26. Pure Cu sample and

SEM pictures are shown in Figure 27 to Figure 29.
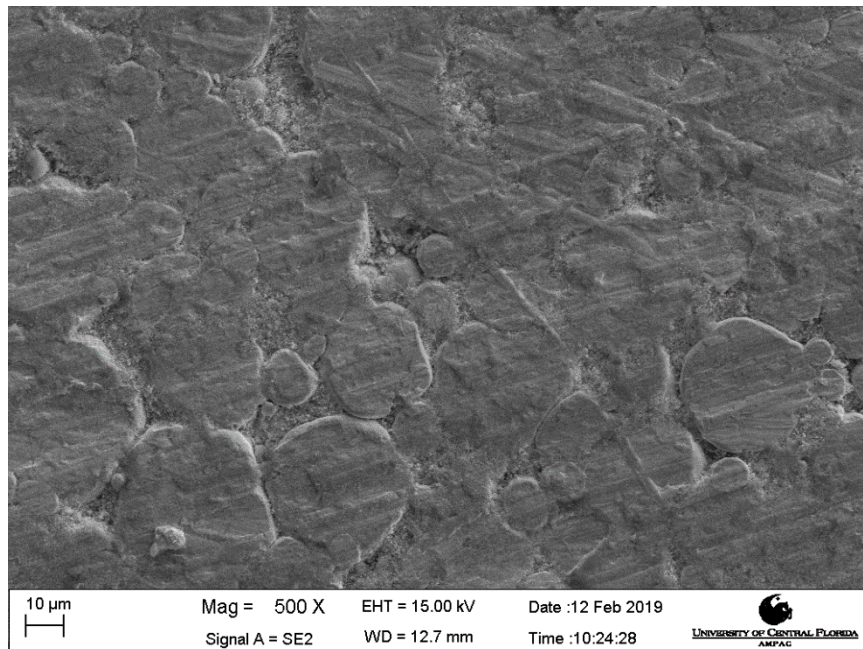
Figure 24. Cu-Ni/CNTs SEM picture (500X).
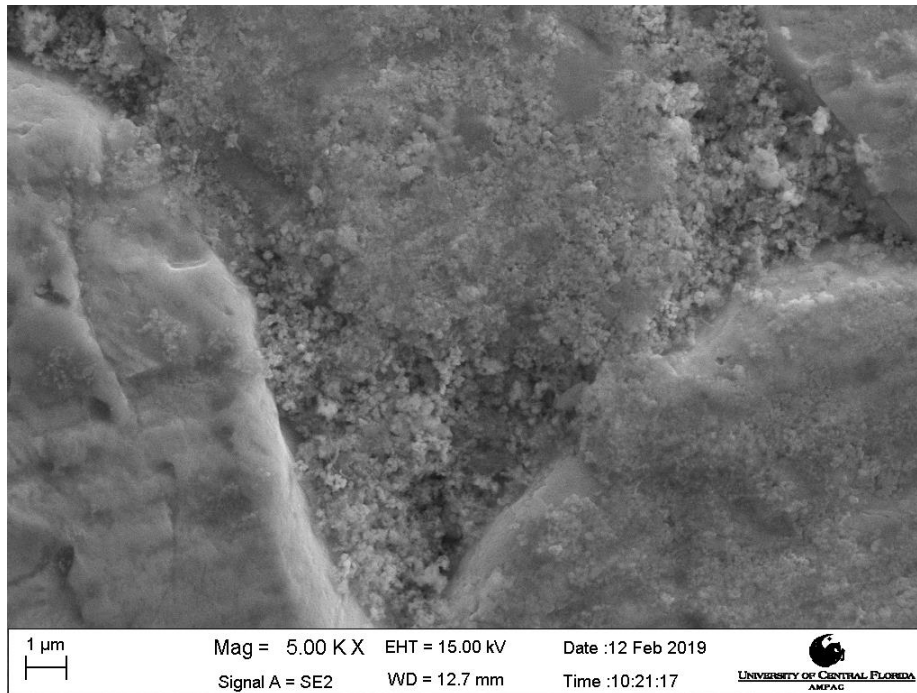
Figure 25. Cu-Ni/CNTs SEM picture (5KX).

Figure 26. Cu-Ni/CNTs sample.
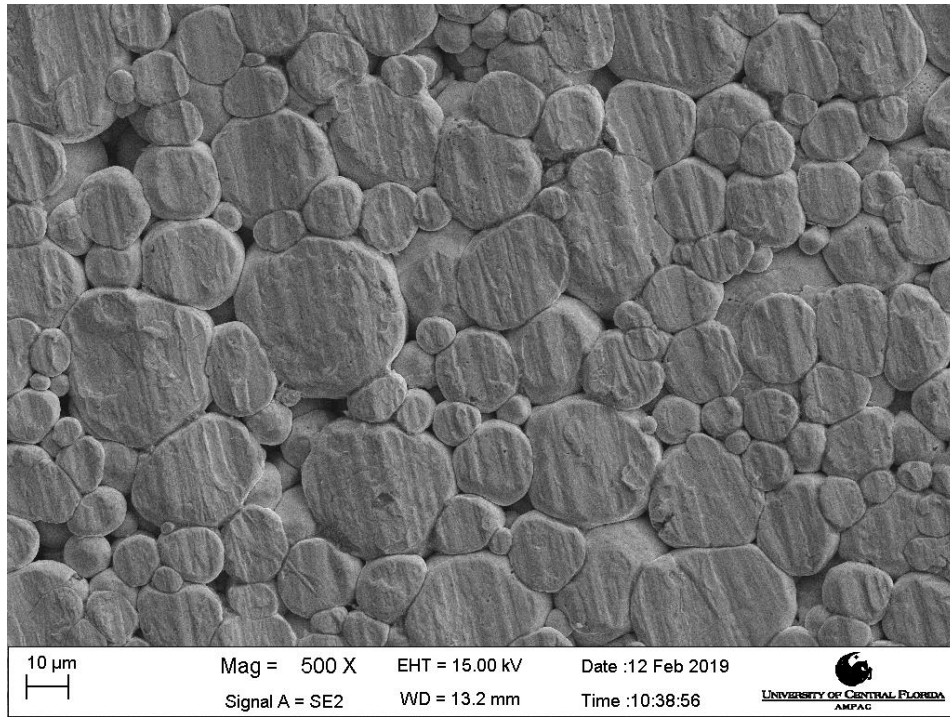
Figure 27. Pure Cu SEM picture(500X).
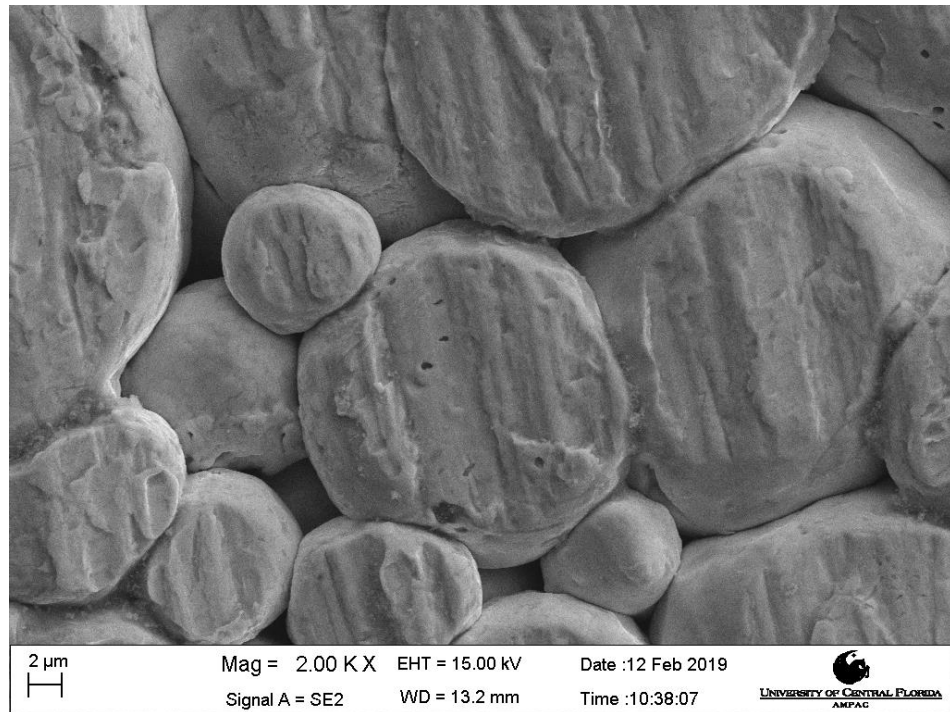
Figure 28. Pure Cu SEM picture(2KX).

Figure 29. Pure Cu sample.

3.8 Finite Element Simulation of Aluminum Powder Compaction

A finite element model was built to simulate the aluminum powder compaction process for the cold compaction and the hot compaction with 300°C. This model will help to understand the mechanics mechanism of the aluminum powder compaction. The force with displacement curves can be predicted through this FE model. The relative density of the aluminum specimen also can be obtained from the simulation model. It will give a guide for the research of the powder compaction tests. For example, if a specific force loading is applied on the powder, this model can predict the density of the specimen made from the powder without running tests.

This finite element model was built by Abaqus/Standard (version 2017). The compaction die is a cylindrical body, was shown in Figure 30. The finite element model of the powder compaction can be built with an axisymmetric model. It was composed of a die and the aluminum powder. The die was considered as a rigid body and the aluminum powder was considered as a deformable body. The CAX4R element is used in Abaqus for the aluminum powder, which is a 4-node axisymmetric quadrilateral, reduced integration, hourglass control element. The discrete rigid element RAX2 is used for the rigid die.

3.8.1 Model Assumptions and Boundary Conditions

In the finite element model, the punch is considered as a rigid plane. The top surface of the powder

body is loaded by an initial displacement. The initial displacement loading can also be replaced by the initial force loading. The results of the finite element model will be the same. Figure 30 shows the finite element model setup.
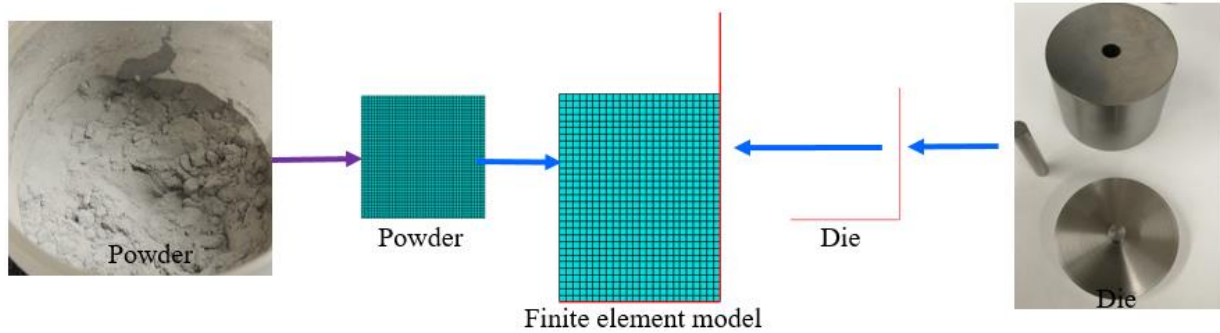
Figure 30. A sketch of finite element model for powder compaction

The die is also considered as a rigid body, and the powder is a deformable body. A deformable die model is built to validate the accuracy of this assumption. Figure 31 shows the geometry model and the result of deformation from the model. Since the die deformation is negligible, the rigid die is a valid assumption.

(a)   (b)
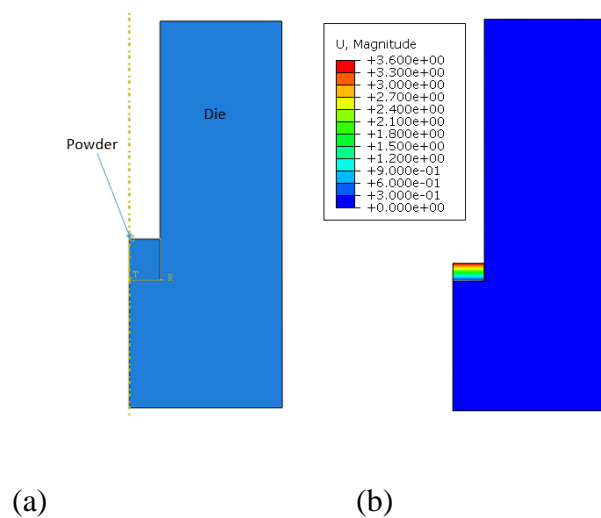
Figure 31. FE simulation using a deformable die. (a)Initial geometry, (b)Deformation in simulation.

Figure 3 shows the geometry models of the cold compaction and the hot compaction tests. The finite element model setup is show in Figure 30. The boundary conditions are shown in Figure 32. The mesh size is 0.1mm for the aluminum powder and the die. There is a contact definition between the die and the aluminum powder. The aluminum powder gradually slides along the die when subjected to a compaction pressure. A friction coefficient 0.1 is defined in this model. The aluminum powder is applied by a prescribed displacement from the test data.
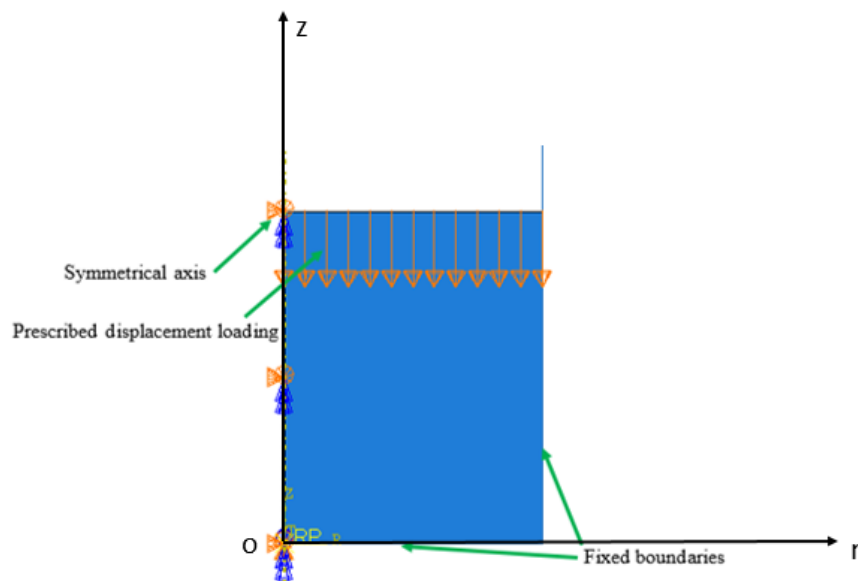
Figure 32. Boundary conditions of aluminum powder compaction simulation

3.8.2 Constitutive Model of Aluminum Powder

Drucker Prager Cap (DPC) model is a popularly used material constitutive model for the powder compaction simulation. Generally, it is used as Soil Mechanics. The material property of the soil has some similar characteristics with the powder. There are pores in the material between them. Steel and aluminum solid are considered as continuum objects. They are incompressible, because

43

the volume of the substance can not be changed by the outside pressure. On the other hand, foam, soils and powders are considered as the compressible substance, because there are a lot of pores in their materials. When this kind of material is compressed by outside pressure, these pores can decrease by force, then the volume of the materials changed. Because Drucker Prager Cap model can describe the compressible characterization of the powder, it is used as the material constitutive model of the simulation model.

The yield locus of DPC model in the p-t plane is shown in Figure 33. Uniaxial compression and confined compression tests (using our powder compaction tests as an approximation) were conducted to calibrate this model.
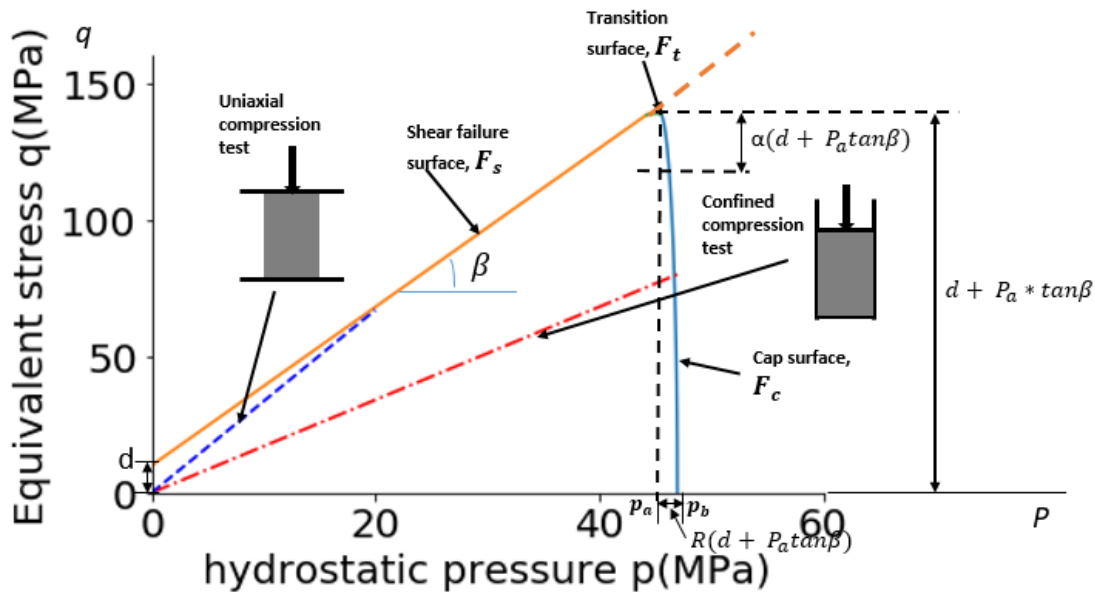
Figure 33. Drucker Prager Cap Model in the p-q plane, where real material parameters are used.

This model contains a cap yield surface, a shear failure surface and a transition surface. The cap yield surface bounds the yield surface in the hydrostatic compression, which gives a plastic

44

hardening mechanism to describe the plastic deformation of the powder compaction. It also controls the volume dilatancy after the material starts to yield. The shear failure surface of Drucker Prager model is written as the following equation.

$$F_s = t - p \tan \beta - d \tag{1}$$

Here, β and d are material's friction angle and the cohesion, which depends on temperature. The deviatoric stress measure t is written as the bellow equation.

$$t = \frac{1}{2} q \left[1 + \frac{1}{K} - \left(1 - \frac{1}{K} \right) \left(\frac{r}{q} \right)^3 \right] \tag{2}$$

Where, $p = -\frac{1}{3} trace(\sigma)$ is the mean pressure. $q = \sqrt{\frac{3}{2} S:S}$ is the Mises equivalent stress. $r = \left(\frac{9}{2} S:S \cdot S \right)^{\frac{1}{3}}$ is the third deviatoric stress invariant($s = \sigma + pI$). K is a material parameter that defines the dependence of the yield surface on r.

The cap yield surface is described as followings.

$$F_c = \sqrt{[p - p_a]^2 + \left[\frac{Rt}{(1 + \alpha - \alpha/\cos\beta)} \right]^2} - R(d + p_a tan\beta) = 0 \tag{3}$$

R is a material parameter that can give the shape of the cap, and p_a is an evolution parameter that describes the volumetric plastic strain. The hardening law is a linear function of hydrostatic compression yield stress (p_b) and volumetric inelastic strain, which is described as the following equation.

$$p_b = p_b(\varepsilon_{vol}^{in} |_0 - \varepsilon_{vol}^{in} + \varepsilon_{vol}^{cr}) \tag{4}$$

The evolution of parameter p_a is described as the following equation.

$$p_a = \frac{p_b - Rd}{(1 + Rtan\beta)} \tag{5}$$

The material parameters of Drucker Prager model contain the cohesion d, the angle of friction β, the cap eccentricity R, the initial cap yield surface position on the volumetric inelastic strain axis $\varepsilon_{vol}^{in}\vert_0$, the transition surface radius parameters α, and the ratio of the flow stress in triaxial tension to the flow stress in triaxial compression K. The above 6 parameters mentioned are Drucker-Prager/Cap plasticity yield surface parameters. Elastic modulus and Poisson ratio are also required for this model. The key input is the evolution of volumetric strain hardening curve (Eq. (4)).

3.8.3 Calibration Method of DPC Material Constitutive Model

An iteration calibration method was used to obtain the material parameters of DPC model. Firstly, to conduct a confined compression test to get DPC volumetric strain hardening parameter curve. Then to perform finite element analysis to obtain the unknown material parameters of DPC model. Finally, to iterate finite element analysis until the force-displacement curve of the simulation model gets well match with that of the test. Figure 34 shows a flow chart of this calibration method.
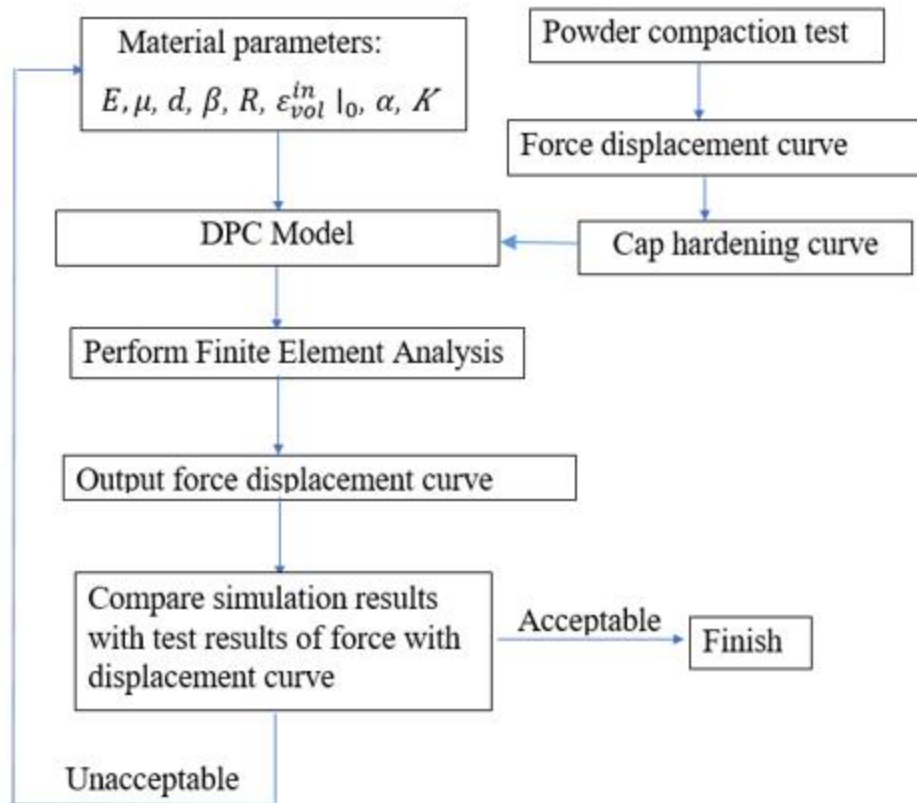
Figure 34. A flowchart of material parameters calibration procedure for the DPC model

3.8.4 Material Property of Aluminum Powder

According to the calibration method of Drucker Prager Cap model (see Section 3.8.3), the material properties of the aluminum powder are listed in Table 6. In this paper, two FEA models are built, which are the loading condition 10kN force on 0.427g aluminum powder without temperature loading, and the loading condition 10kN force on 0.445g aluminum powder with 300°C temperature loading. The same elastic material property and the plastic yield parameters are used as listed in Table-5. The difference between the cold compaction and the hot compaction models is that these two models have different volumetric strain hardening curves. Figure 35 shows the volumetric strain hardening curves for these two loading conditions.

Table 6. Material properties of aluminum powder

Cap plasticity's parameters	
Cohesion d (MPa)	0.01
Friction angle β (°)	71
Eccentricity R	0.021
Initial yield surface position p_a (MPa)	0.01
Flow stress ratio K	1
Elastic Parameters	
Young's modulus E(MPa)	5000
Poisson ratio μ	0.29
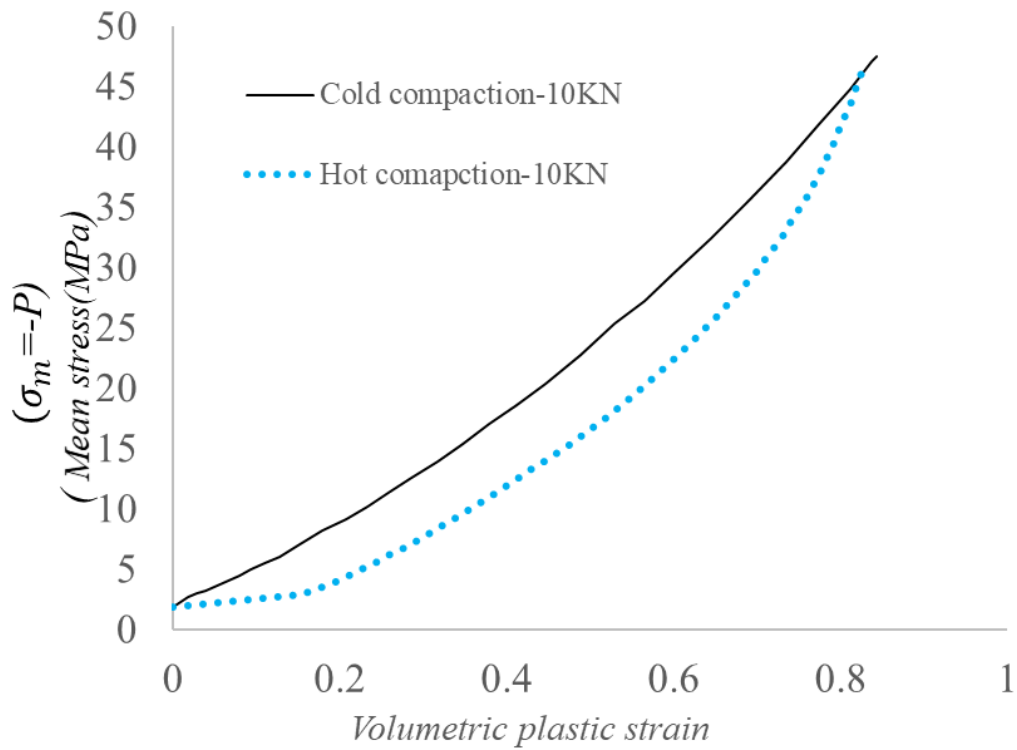
Figure 35. Two inputs of cap hardening curves for cold compaction and hot compaction loadings.

3.8.5 Results Comparison

For the results of finite element model, the top surface of the aluminum powder model can obtain the total force of all nodes with time. And the displacement with time curve is the input excitation in the simulation model. Thus, the force with displacement curve can be obtained. Figure 36 shows the force with displacement curves between tests and finite element models for the cold compaction and the hot compaction. One can conclude that there is a good match between tests and simulations. In the initial phase of powder compaction, powders experienced elastic deformation because of some loose powders, and then the plastic strain gradually increases with the growth of the displacement. The evolutions of the relative density ratios with respect to the axial pressure are plotted in Figure 37. It is found that it needs a larger force for the cold compaction test than that of the hot compaction in order to obtain the same density ratio. However, there is a transition point at the beginning of the curves, which may be due to the thermal expansion and the friction between the die and the punch.
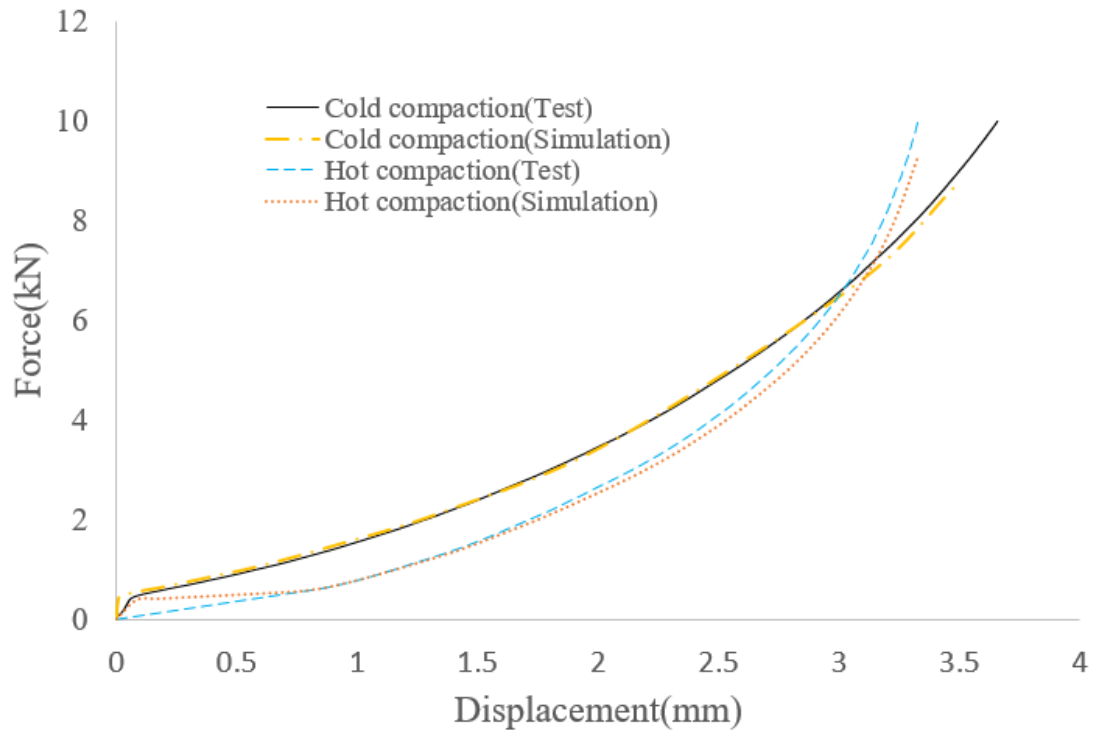
Figure 36. Comparisons of force with displacement curves of cold compaction and hot compaction obtained from FE simulations. Test data are also included for the comparison. A very good correlation is achieved.
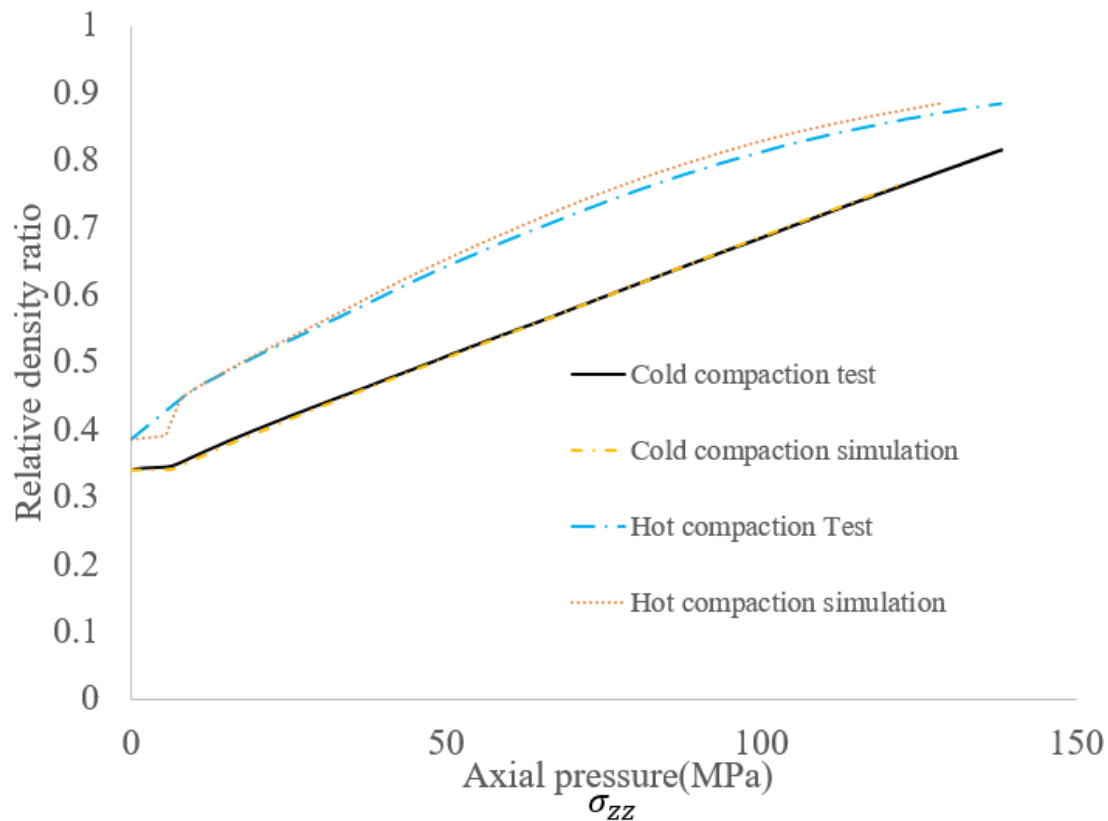
Figure 37. Evolution of relative density ratio with axial pressure of cold compaction and hot compaction simulations. Test data are also included for comparison. A very good correlation is achieved.

One important phenomenon is that the relative density ratio of the hot compaction test is larger than that of the cold compaction test. The biggest difference of the density ratio between the cold compaction and the hot compaction is about 0.15. So, the hot compaction test will be a good choice for the improvement of the relative density ratio of the material if the cold compaction test cannot reach an ideal goal.

According to the test and simulation results of the aluminum powder compaction in the cold compaction, the fitted curves can be extrapolated to predict other compaction pressure conditions.

Figure 38 and Figure 39 show the relative density ratio with the compaction pressure for the test, simulation and the predicted results. The fitted curves can provide a guide for predictions of the relative density of the aluminum powder cold and hot compaction. It is found that the overall trend is nonlinear, and the FE simulations well predict this nonlinearity. Equation 6 and Equation 7 are obtained from the curve fitting of both test data and simulation results for the cold compaction and hot compaction conditions. These two equations can accurately predict the relative density for a specific compression pressure.

$$\bar{\rho}_{cold} = f(\sigma_{zz}) = 1 - 0.715e^{-0.007\sigma_{zz}} \tag{6}$$

$$\bar{\rho}_{hot} = f(\sigma_{zz}) = 1 - 0.626e^{-0.012\sigma_{zz}} \tag{7}$$
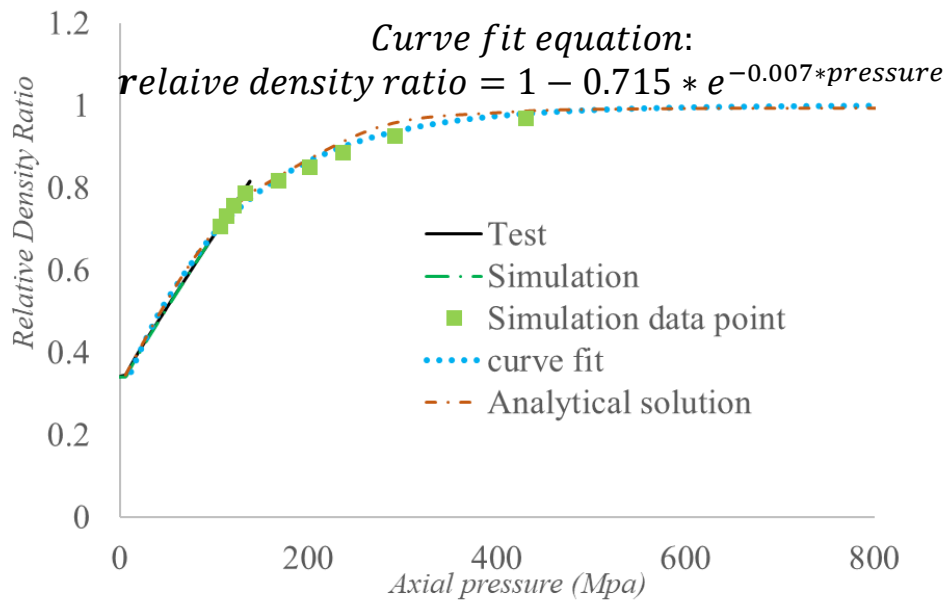
Figure 38. Curve fitting of combined test data and FE simulations to predict relative density ratio with respect to axial pressure σ_{zz} for aluminum powder cold compaction (simulation data point is the extrapolated points from the simulation curve fitted).

52
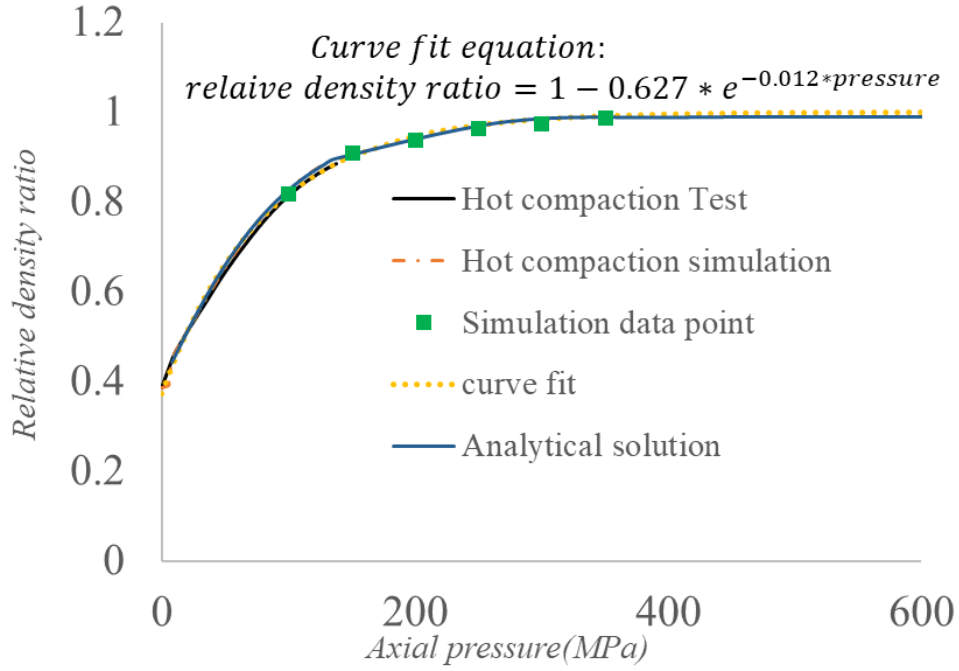
Figure 39. Curve fitting of combined test data and FE simulations to predict relative density ratio with respect to axial pressure σ_{zz} for aluminum powder hot compaction (simulation data point is the extrapolated points from the simulation curve fitted).

3.9 Analytical Solution of Axial Pressure Versus Density Ratio

This section derives an analytical solution of axial pressure versus density ratio. A cylindrical coordinate system for powder compaction is illustrated in Figure 32. Since a rigid die is assumed, the radial strain rate and hoop strain rate are zero, $\dot{\varepsilon}_{rr} = \dot{\varepsilon}_{\theta\theta} = 0$. The axial strain rate along compressive direction is $\dot{\varepsilon}_{zz} = \frac{\dot{H}}{H}$, where H is the height of a powder sample. Note that the elastic strains are very small than the plastic one, so they are negligible for powder compaction analysis. From the definitions of volumetric plastic strain rate ($\dot{\varepsilon}_{vol}$) and equivalent plastic strain rate ($\dot{\varepsilon}_{eq}$), we can get $\dot{\varepsilon}_{vol} = \dot{\varepsilon}_{zz}$, and $\dot{\varepsilon}_{eq} = \sqrt{\frac{2}{3}\dot{\varepsilon}'_{ij}\dot{\varepsilon}'_{ij}} = \frac{2}{3}\dot{\varepsilon}_{zz}$, where $\dot{\varepsilon}'_{ij}$ are deviatoric plastic strain rate

53

components. Hence, we have the following equation.

$$\dot{\varepsilon}_{eq} = \frac{2}{3}\dot{\varepsilon}_{vol} \tag{8}$$

According to the FE simulation of powder compactions, it is found that powder is subjected to a loading condition following the region of cap yield surface. See Figure 33. From the cap yield surface (Eq. (3)), an associated flow rule (AFR) is used. To simplify the yielding equation, let

$\gamma = \frac{R}{\left(1+\alpha-\alpha/_{\cos\beta}\right)}$, and $p_b - p_a = R(d + p_a tan\beta)$. Since this is an axial symmetric loading in powder compaction, $K = 1$, then $t = q$. Therefore Eq. (3) becomes

$$F_c = \sqrt{(p - p_a)^2 + (\gamma q)^2} - (p_b - p_a) = 0. \tag{9}$$

From the AFR material flow rule, we can derive the material plastic flow strain rates as follows.

$$\dot{\varepsilon}_{ij} = \dot{\Lambda}\frac{\partial F_c}{\partial \sigma_{ij}} = \dot{\Lambda}\frac{1}{2(p_b-p_a)}\left[\frac{2}{3}(p - p_a)\delta_{ij} + 3\gamma^2 s_{ij}\right] \tag{10}$$

Here the equations of $\frac{\partial p}{\partial \sigma_{ij}} = \frac{1}{3}\delta_{ij}$ and $\frac{\partial q}{\partial \sigma_{ij}} = \frac{3}{2q}s_{ij}$ are used. From Eq. (10), the volumetric strain rate and equivalent plastic strain rates can be evaluated as follows.

$$\dot{\varepsilon}_{vol} = \dot{\varepsilon}_{kk} = \dot{\Lambda}\frac{(p-p_a)}{(p_b-p_a)} \tag{11}$$

$$\dot{\varepsilon}_{eq} = \sqrt{\frac{2}{3}\dot{\varepsilon}'_{ij}\dot{\varepsilon}'_{ij}} = \frac{\dot{\Lambda}\gamma^2}{(p_b-p_a)}\sqrt{\frac{3}{2}s_{ij}s_{ij}} = \frac{\dot{\Lambda}\gamma^2 q}{(p_b-p_a)} \tag{12}$$

Here the equation of $\delta_{kk} = 3$ is used. Substituting Eq. (11) and Eq. (12) into Eq. (8), we can get the following important relationship between p and q.

$$\gamma^2 q = \frac{2}{3}(p - p_a) \tag{13}$$

Specifying the strain components (Eq. (10)) in the cylindrical coordinate system, we have the following three equations.

$$\dot{\varepsilon}_{rr} = \dot{\Lambda} \; \frac{1}{2(p_b - p_a)} \left[\frac{2}{3}(p - p_a) + 3\gamma^2(\sigma_{rr} + p) \right] = 0 \tag{14}$$

$$\dot{\varepsilon}_{\theta\theta} = \dot{\Lambda} \; \frac{1}{2(p_b - p_a)} \left[\frac{2}{3}(p - p_a) + 3\gamma^2(\sigma_{\theta\theta} + p) \right] = 0 \tag{15}$$

$$\dot{\varepsilon}_{zz} = \dot{\Lambda} \; \frac{1}{2(p_b - p_a)} \left[\frac{2}{3}(p - p_a) + 3\gamma^2(\sigma_{zz} + p) \right] \tag{16}$$

From Eq. (14) and Eq. (15), we can get that $\sigma_{\theta\theta} = \sigma_{rr}$. Again, the definitions of p and q indicate that $p = -\frac{(\sigma_{rr} + \sigma_{\theta\theta} + \sigma_{zz})}{3} = -\frac{2\sigma_{rr} + \sigma_{zz}}{3}$, and $q = \sigma_{rr} - \sigma_{zz}$. Hence the axial pressure (stress) can be expressed as follows.

$$\sigma_{zz} = -p - \frac{2}{3}q \tag{17}$$

The three equations, Eq. (13), Eq. (17) and the cap yield surface (Eq. (9)), solve three unknowns, p, q, and σ_{zz} as follows.

$$p = \frac{\frac{3}{2}\gamma}{\sqrt{\frac{9}{4}\gamma^2 + 1}} (p_b - p_a) + p_a \tag{18}$$

$$q = \frac{(p_b - p_a)}{\gamma\sqrt{\frac{9}{4}\gamma^2 + 1}} \tag{19}$$

$$\sigma_{zz} = -\frac{\frac{3}{2}\gamma^2 + \frac{2}{3}}{\gamma\sqrt{\frac{9}{4}\gamma^2 + 1}} (p_b - p_a) - p_a \tag{20}$$

From the feature of a volumetric strain hardening curve (see Figure 35), it is assumed that $p_b = A + Be^{C\varepsilon_{vol}}$, where A, B, and C are three curve fitting constants, as listed in Table 7. Note that the best curve fitting gives the parameter $A = 0$, which is actually a very small initial number.

Table 7. Constants of p_b parameters

Parameters	Cold compaction	Hot compaction
A (MPa)	0	0
B (MPa)	5.61	3.08
C (-)	2.60	3.26

Thus, we can calculate σ_{zz} in terms of volumetric plastic strain, which is directly related to the relative density ratio ($\bar{\rho}$) through $\varepsilon_{vol}=\ln(\bar{\rho})$. Finally, the above equation can be updated as following.

$$\sigma_{zz} = \frac{\frac{3}{2}\gamma^2+\frac{2}{3}}{\gamma\sqrt{\frac{9}{4}\gamma^2+1}}\left(A + B(\frac{\rho_0}{\rho_R\bar{\rho}})^c - p_a\right) - p_a \tag{21}$$

$$\bar{\rho} = \frac{\rho_0}{\rho_R}\left\{\frac{1}{B}\left[(|\sigma_{ZZ}| - p_a)\frac{\gamma\sqrt{\frac{9}{4}\gamma^2+1}}{\frac{3}{2}\gamma^2+\frac{2}{3}} - A + p_a\right]\right\}^{\frac{-1}{c}} \tag{22}$$

Here ρ_0 is the initial density of the powder material. ρ_R is the reference density of the material. Figure 38 and Figure 39 also show the relation between σ_{zz} and the relative density ratio $\bar{\rho}$ calculated by the analytical solution (Eq. (22). The analytical solution has the following advantages:

 1. The analytical solution can give a quick prediction without the numerical analysis.

2. The analytical solution can extrapolate the relative density of the material without the test data.

3. The simulation model needs the calibration process that takes efforts for the specific conditions.

3.10 Conclusions

This chapter introduced two test methods that can improve the density ratio of powder compaction. One is hot compaction method, and the other one is vibration assisted (cold) compaction method. The relative density ratio of the hot compaction method at 300°C has an obvious increase compared to the cold compaction method. The relative density of the vibration assisted compaction method has no increase so far compared to the quasi-static cold compaction method, but the strength of the specimen made from the vibration loading is much better than that of quasi-static one. The main reason is that vibration loading makes micro voids or pores more uniform providing the same density ratio. The Drucker Prager Cap material model was calibrated for the aluminum powder, and a finite element model was built in Abaqus to simulate the cold compaction and the hot compaction tests. A new calibration method was introduced to obtain the material parameters of aluminum powder during compaction process. The results of simulation model correlated very well to test data. The FE models help to understand the powder compaction mechanisms, and they give a guide to achieve a higher density ratio for the material exceeding the test ranges. Finally, an analytical solution of the powder compaction was developed between axial pressure and relative density ratio. The results between the analytical solution and the simulation model have an excellent match.

CHAPTER 4 WIRE EXTRUSION

4.1 Wire Extrusion Tests

A sketch design of two-stage wire extrusion process is shown in Figure 40. Firstly, a Cu/CNT (or other materials) sample was made by powder compaction method. Powder compaction is a widely used manufacturing method in industry areas, see Q. Zhou, Song, Chen, and Bai (2021). Secondly, an extrusion die with a diameter of 12.6mm was used to fabricate another sample with the diameter 6.3mm under the extrusion area ratio of 4:1, which is called Stage I. Lastly, the other extrusion die with a diameter of 6.3mm was used to fabricate Cu/CNT wire of diameter 1.6mm with the extrusion area ratio of 16:1, which is called Stage II.

Cu/CNT sample(13mm)

Extrusion ratio 4:1
(stage I)

Cu/CNT sample(6.3mm)

Extrusion ratio 16:1
(stage II)

Cu/CNT wire(1.6mm)
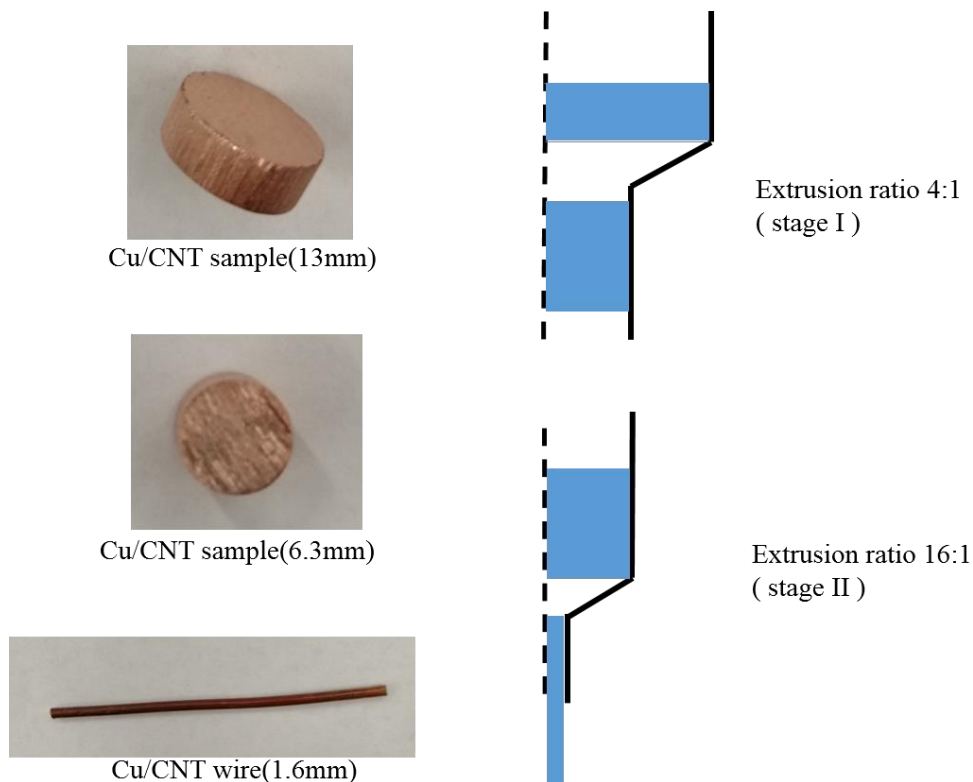
Figure 40. A sketch of two-stage wire extrusion process. Real material sample pictures are also illustrated.
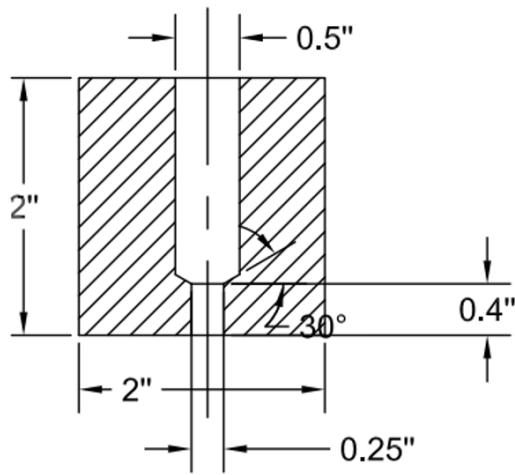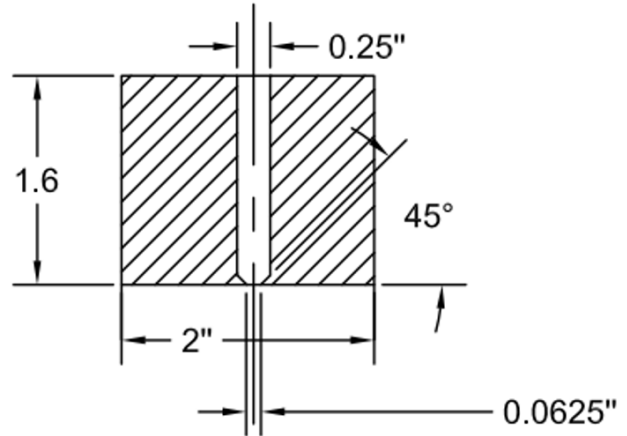
(a) Extrusion ratio 4:1   (b) Extrusion ratio 16:1

Figure 41. Wire extrusion die drawings.
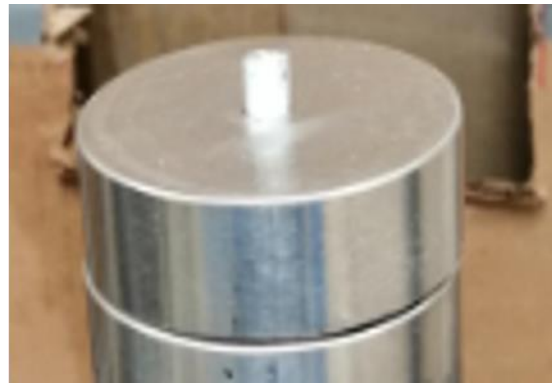
(a) Extrusion ratio 4:1   (b) Extrusion ratio 16:1

Figure 42. Wire extrusion dies.

Extrusion dies and drawings are shown in Figure 41 and Figure 42. The real Cu/CNT wire extrusion

test setup (for stage II) is shown in Figure 43. Wire came out of the extrusion die under 703°C. The

maximum force is 10kN and the stable force is 8kN during the extrusion process, see Figure 44.

The sample and the wire information are shown in Table 8. From Table 8, one can know that the

relative density ratio increased from 0.92 to 0.95 for Stage I. The relative density ratio further

increased from 0.95 to 0.98 at the Stage II.

(a)   (b)
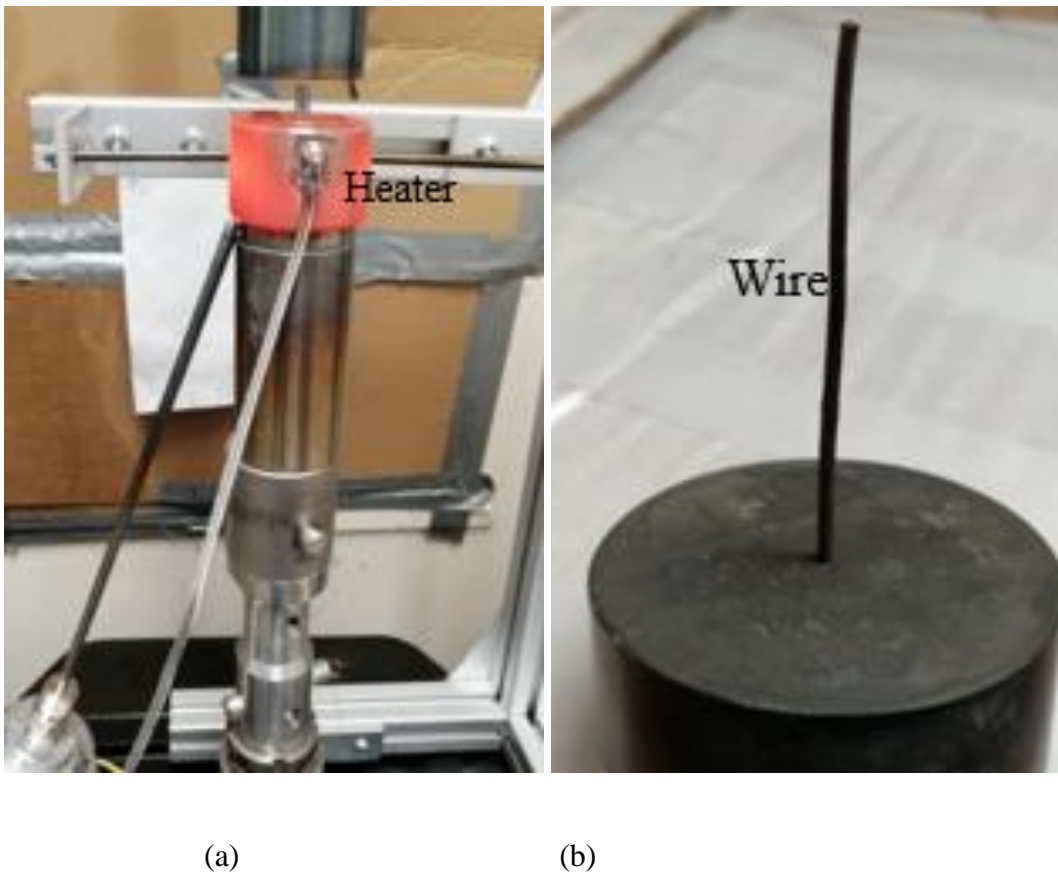
Figure 43. (a)Cu extrusion die and test setup. (b) Extruded wire sample.

Table 8. Parameters of Cu/CNT sample and wire after two-stage extrusion

Items	Cu/CNT sample before extrusion	Cu/CNT sample extruded (stage I)	Cu/CNT wire sample extruded (stage II)
Mass(g)	5.19	1.71	0.85
Height(mm)	4.64	6.58	40.55
Diameter(mm)	13.17	6.24	1.75
Density(g/cm^3)	8.21	8.50	8.73
Relative density	0.92	0.95	0.98
Extrusion force (kN)	N/A	8	25

We also ran extrusion tests for pure aluminum (Al) and pure copper (Cu) samples. The measured force-displacement curves for Al and Cu extrusion tests were also plot in the Figure 44 in order to compare with Cu/CNT samples. Altogether, Figure 44 shows extrusion force curves for Al, Cu, Cu/CNT samples made from the extrusion die with extrusion area ratio 4:1 and Cu/CNT wire sample made from extrusion die with extrusion area ratio 16:1. The heating temperatures are 300°C, 642°, 658°C and 703°C, respectively. For stage II Cu/CNT wire extrusion, the elevated temperature is much higher than that of other samples. That is why the extrusion force curve is more stable for the Cu/CNT wire extrusion process. There is not much strain hardening during the Cu/CNT wire extrusion process.
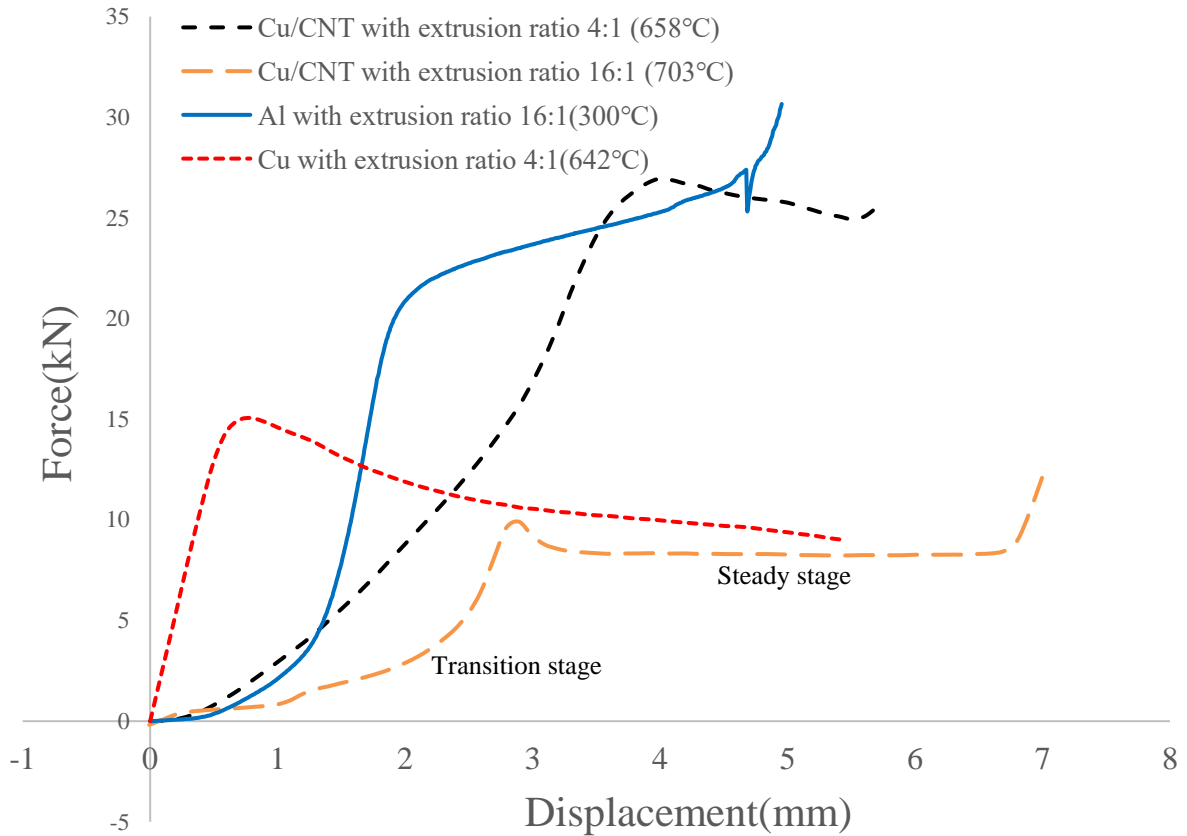
Figure 44. Wire extrusion force curves for Al, Cu and Cu/CNT samples (two stages) under elevated temperature conditions. Note that the differences in the initial stages of curves were affected by different initial contact conditions.

4.2 Finite Element Models with Eulerian Domain

Considering the extremely plastic deformation/flow of material samples under wire extrusion, arbitrary Lagarangian-Eulerian (ALE) adaptive meshing technique is used to build finite element models for the (forward) extrusion process. It can simulate Eulerian boundary where the materials flow through the mesh of the model. The velocity on the entry edge of the model is defined as Eulerian boundary. The exit edge of the model is defined as Eulerian surface in order to obtain the steady state solution during the extrusion process. The inflow and outflow of the meshing were

applied by the adaptive mesh constraints to fix the mesh in the flow direction.

Axisymmetric elements CAX4R in Abaqus are used in finite element model for the sample. CAX4R is a 4-node bilinear axisymmetric quadrilateral, reduced integration and hourglass control element. Explicit solver of Abaqus is used in this extrusion model.

Finite element model is composed of the sample and the extrusion die. Extrusion model is shown in Figure 45. The extrusion die is built as a rigid body. The sample is defined as a deformable body. An initial velocity is applied at the top edge of sample element. Material property is simplified as a perfectly plastic material. The contact is defined between sample and die. Friction coefficient can be input in the contact region.
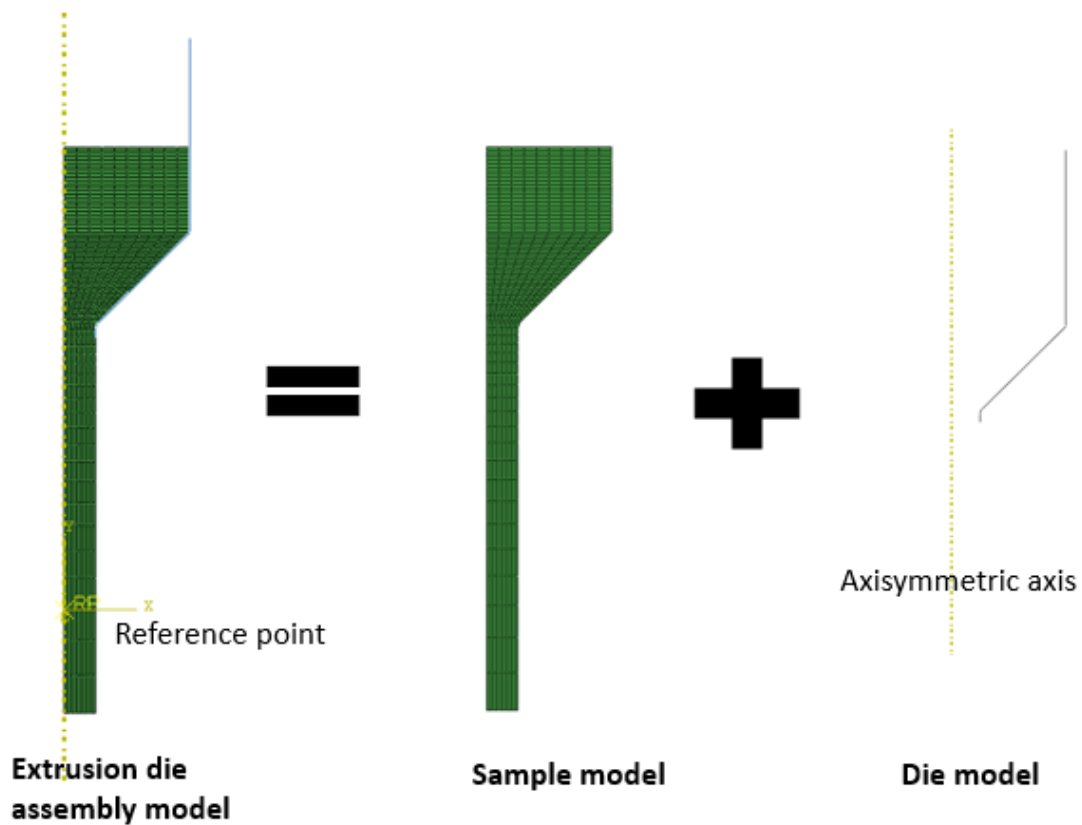
Figure 45. Extrusion die assembly model (it is composed of sample and extrusion die).

Material property is shown in Table 9.

Table 9. Material property for Cu wire extrusion

Young's Modulus (MPa)	1.10E+05
Poisson's ratio	0.33
Density(kg/m^3)	8960
Perfect plasticity (MPa)	90

4.2.1 Extrusion Area Ratio 4:1

Nine finite element models with different extrusion angles and different friction coefficients were built to simulate extrusion process under extrusion area ratio of 4:1. Finite element models of different extrusion angles were illustrated in Figure 46.

Figure 47 shows that the maximum equivalent plastic strains are 1.8, 2.7 and 3.5 under the die angle of 30°, 45° and 60°, respectively. They were simulated under three different friction coefficients of $\mu = 0, 0.5, 0.1$, respectively. One can see that the material deformed more severely and more locally under the higher die angle condition and higher friction.

As summarized in Figure 48, the extrusion force is not very sensitive to the die angle when the friction coefficient is fixed. The extrusion force increased with the friction coefficient when a die angle is fixed. Something more complex is that the relations of extrusion force with respect to die angle and friction coefficient are generally not linear. The simulated extrusion force curves with extrusion area ratio 16:1 are also plot in Figure 48 for further comparison.
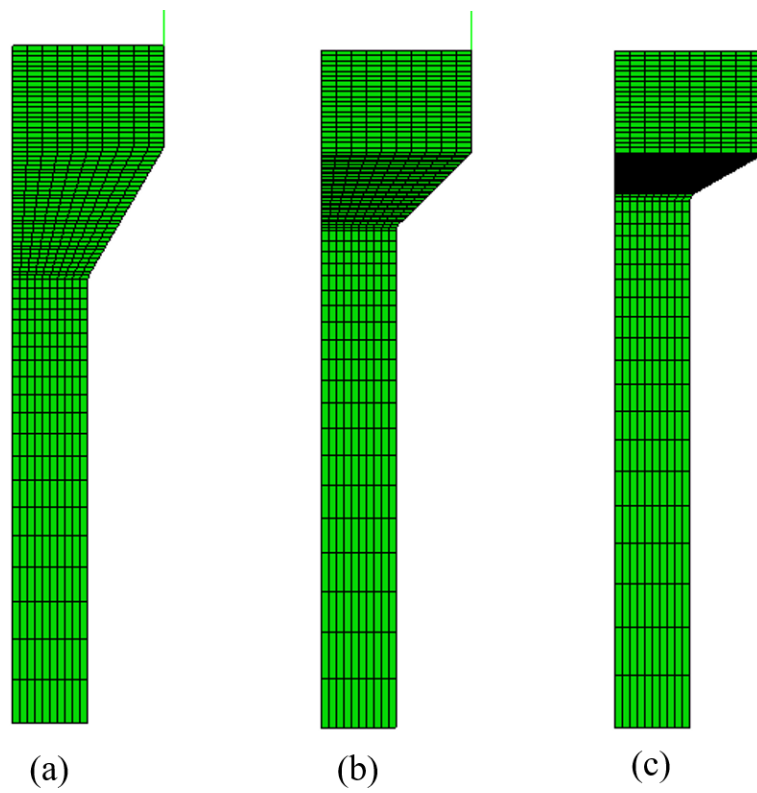
Figure 46. Finite element models with extrusion area ratio 4:1. (a) die angle 30°, (b) die angle 45°, (c) die angle 60°.

Figure 47. Equivalent plastic strain contours of finite element model for the extrusion area ratio 4:1. (a) Die angle 30°, friction coefficient $\mu = 0$; (b) Die angle 30°, $\mu = 0.05$; (c) Die angle 30°, $\mu = 0.1$; (d) Die angle 45°, $\mu = 0$; (e) Die angle 45°, $\mu = 0.05$; (f) Die angle 45°, $\mu = 0.1$; (g) Die angle 60°, $\mu = 0$; (h) Die angle 60°, $\mu = 0.05$; (i) Die angle 60°, $\mu = 0.1$.
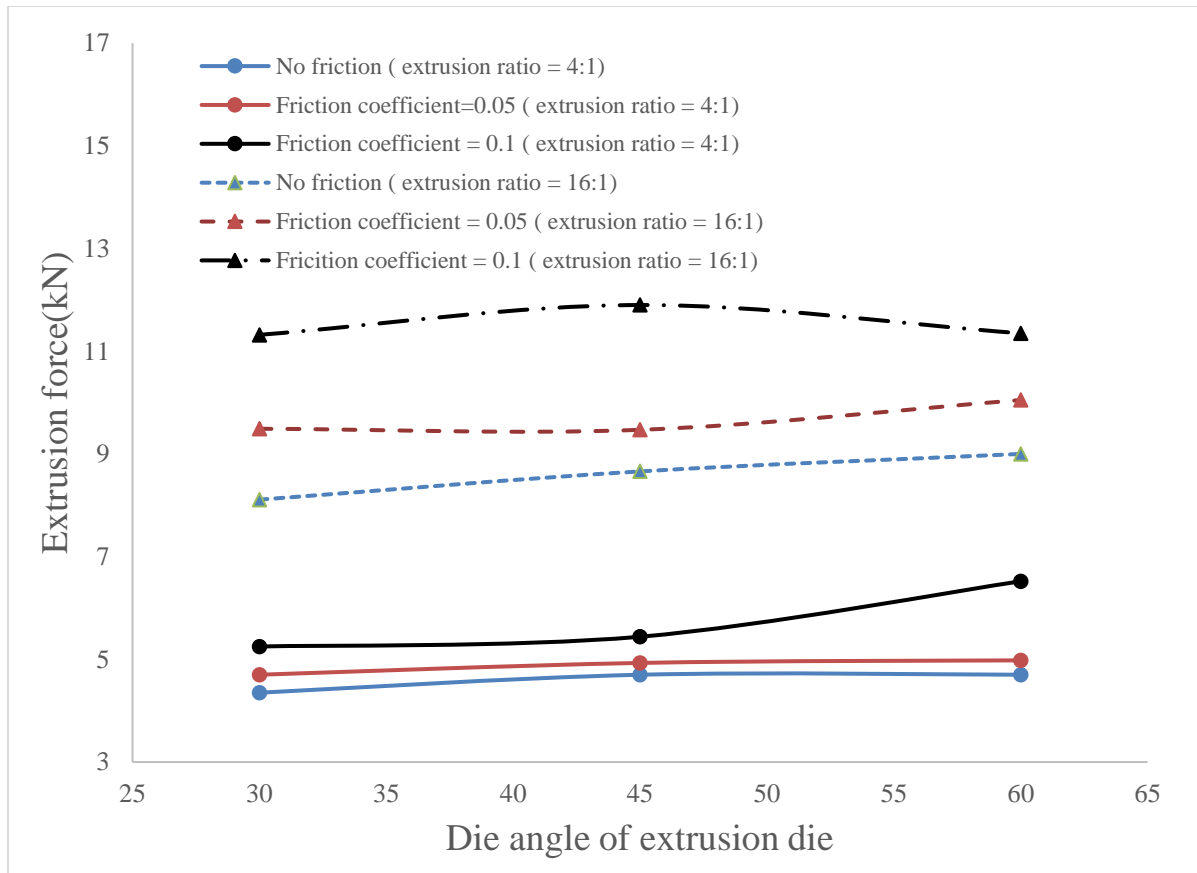
Figure 48. A summary of extrusion forces from finite element model simulations for extrusion area ratio of 4:1 and 16:1.

4.2.2 Extrusion Area Ratio 16:1

Another nine extrusion models were built to demonstrate different extrusion angles 30°, 45°, 60° and different friction coefficients 0. 0, 0.05 and 0.10. They have the same input radius and output radius for the extrusion die dimension. Three models with different extrusion angles are shown in the following picture Figure 49. Equivalent plastic strain contours from simulations are shown in the following picture Figure 50 for the extrusion angle 30°, 45°, 60° of the extrusion dies under 0.05, 0.1 friction coefficient and no friction condition. Figure 48 shows the extrusion force comparisons of finite element models with different friction coefficients together with extrusion

area ratio of 4:1.

From Figure 48, one can conclude that most of equivalent plastic strain have already obtained the stable status during the last time step. The maximum equivalent plastic strain happened on the friction efficient 0.1 condition for every extrusion angle. The maximum equivalent plastic strain is 3.65, 4.63 and 4.71, respectively. From Figure 48, it is found that the extrusion force increased with the increase of friction coefficient. The highest curve in this figure is the extrusion force curve under friction coefficient of 0.10. The extrusion force is again not very sensitive to extrusion angle under a same extrusion area ratio and a same friction coefficient, and it slightly increased with the die angle increment under the friction coefficient 0.00. However, it is not monotonous for the other two friction coefficients, 0.05 and 0.10.

(a)   (b)   (c)
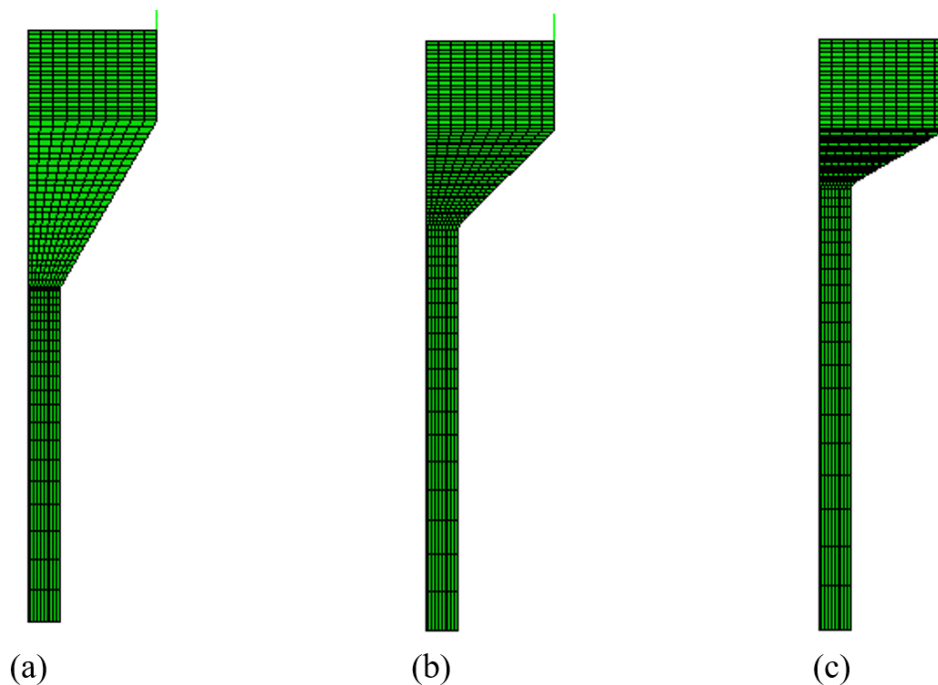
Figure 49. Extrusion models with different die angles. (a) die angle 30°, (b) die angle 45°, (c) die angle 60°.
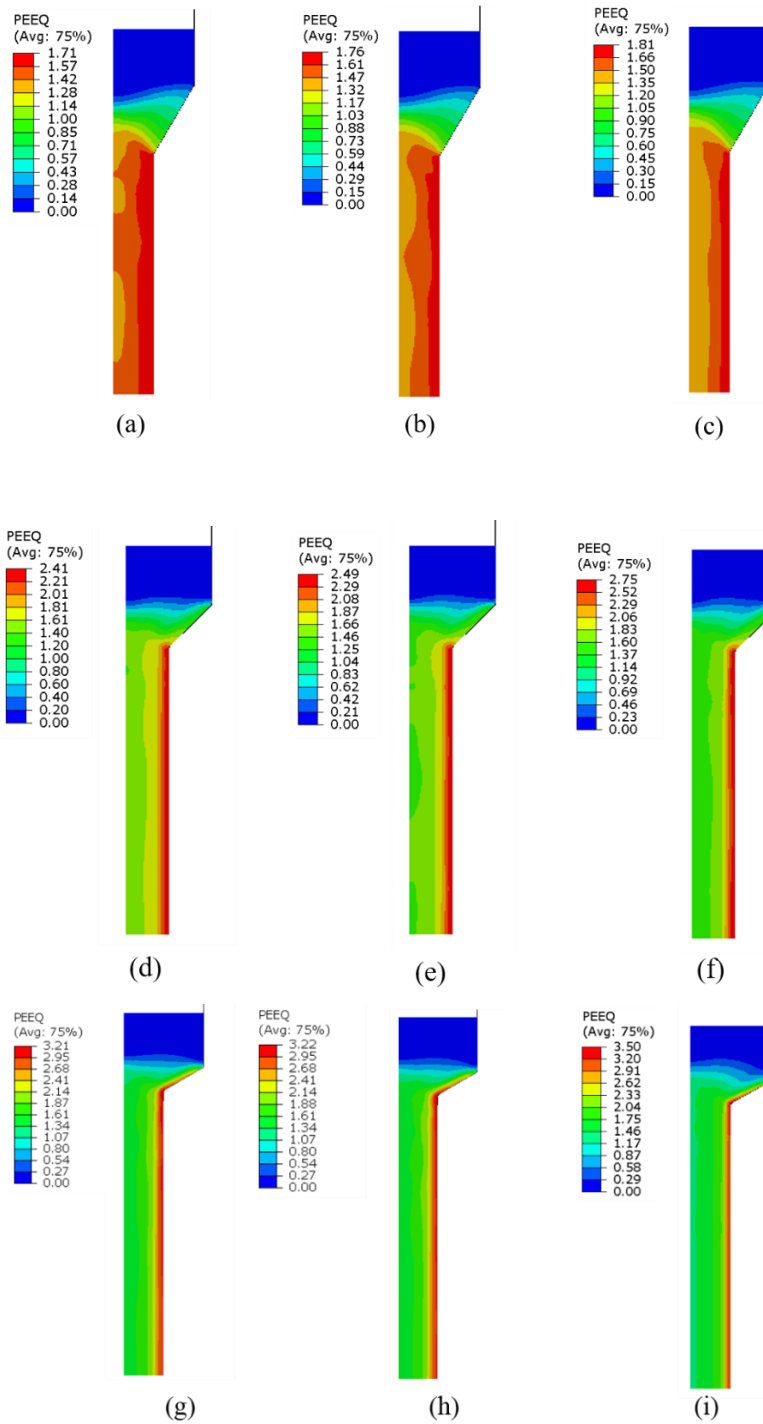
Figure 50. Equivalent plastic strain contours of finite element model for extrusion area ratio 16:1. (a) Die angle 30°, $\mu = 0$; (b) Die angle 30°, $\mu = 0.05$; (c) Die angle 30°, $\mu = 0.1$; (d) Die angle 45°, $\mu = 0$; (e) Die angle 45°, $\mu = 0.05$; (f) Die angle 45°, $\mu = 0.1$; (g) Die angle 60°, $\mu = 0$; (h) Die angle 60°, $\mu = 0.05$; (i) Die angle 60°, $\mu = 0.1$.

69

4.3 Finite Element Models with Lagrangian Domain

Lagrangian domain is used in the finite element model in to simulate the wire extrusion process same as the physical wire extrusion experiment process. An initial billet is put in the extrusion die, it is not deformed at first. Then, it deformed after the pressure applies on the billet in the extrusion die. Because the billet will undergo the extreme distortion when the section area of wire extrusion die reduces along the extrusion flow direction. Adaptive meshing technique is also used in the finite element models with Lagrangian domain.

Axisymmetric elements CAX4R in Abaqus are also used for the sample same as the model with Eulerian domain. Extrusion die is built as a rigid body in the models. One reference point is used to fix the rigid extrusion die as its boundary condition. Explicit solver of Abaqus is also used in this extrusion model to obtain the convergence for Abaqus solver process.

Extrusion model is shown in Figure 51. An initial velocity is applied at the top edge of billet element. Material property is simplified as a perfectly plastic material same as the last section 4.2 introduced. The contact area is defined between billet and extrusion die. Friction coefficient can be input in the contact region.
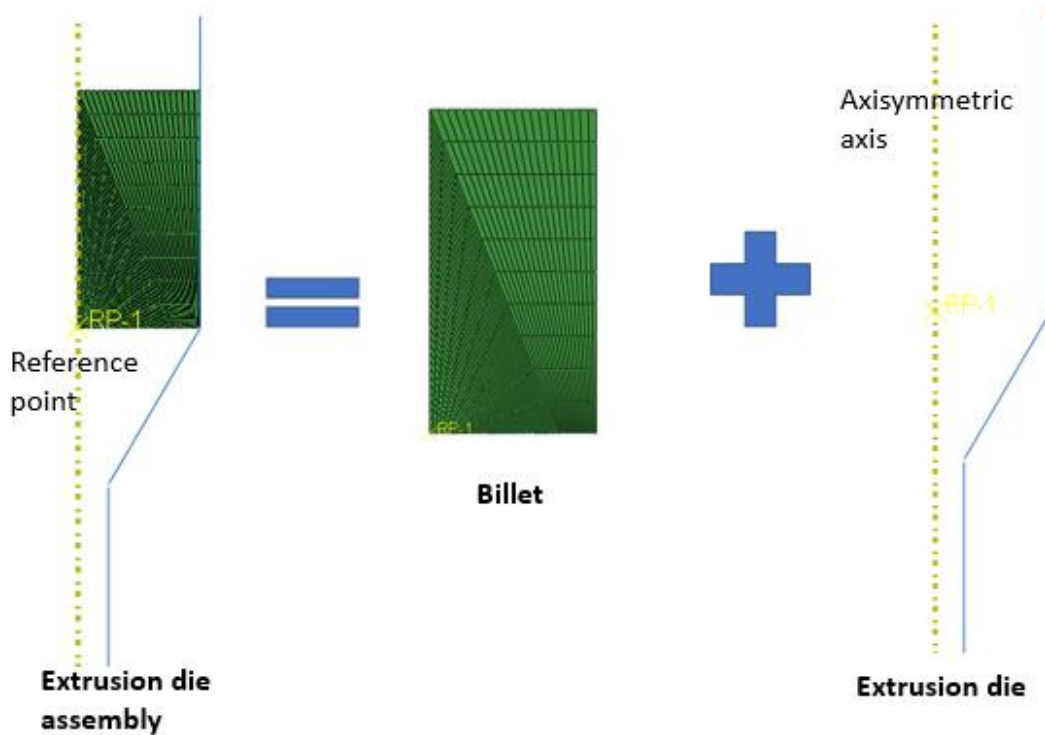
Figure 51. Extrusion die assembly model (it is composed of billet and extrusion die).

4.3.1 Extrusion Area Ratio 16:1

Nine finite element models with different extrusion angles and different friction coefficients were built to simulate extrusion process under extrusion area ratio of 16:1. Finite element models of different extrusion angles were illustrated in Figure 52.

Figure 53 shows that the maximum equivalent plastic strains are 3.54, 3.56 and 4.13 under the die angle of 30°, 45° and 60°, respectively. They were simulated under three different friction coefficients of $\mu = 0, 0.5, 0.1$, respectively. One can see that the material deformed more severely and more locally under the higher die angle condition and higher friction.

As summarized in Figure 54, the extrusion force is not very sensitive to the die angle when the friction coefficient is fixed. The extrusion force increased with the friction coefficient when a die angle is fixed. Something more complex is that the relations of extrusion force with respect to die angle and friction coefficient are also not linear. The simulated extrusion forces with extrusion area ratio of 4:1 (which will be discussed in Section 4.3.2) are also plot in Figure 54 for further comparison.

Die angle =30°   Die angle = 45°   Die angle = 60°

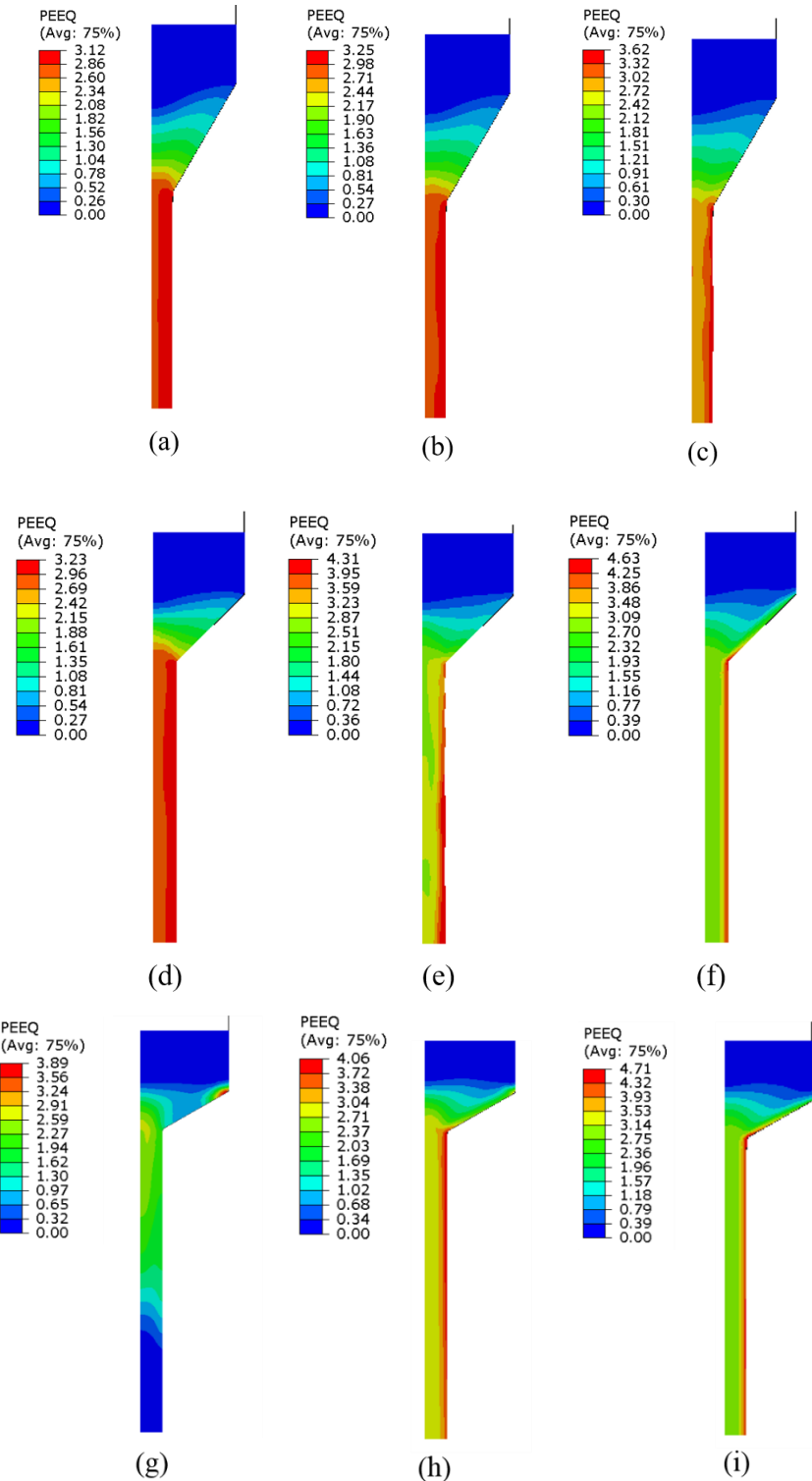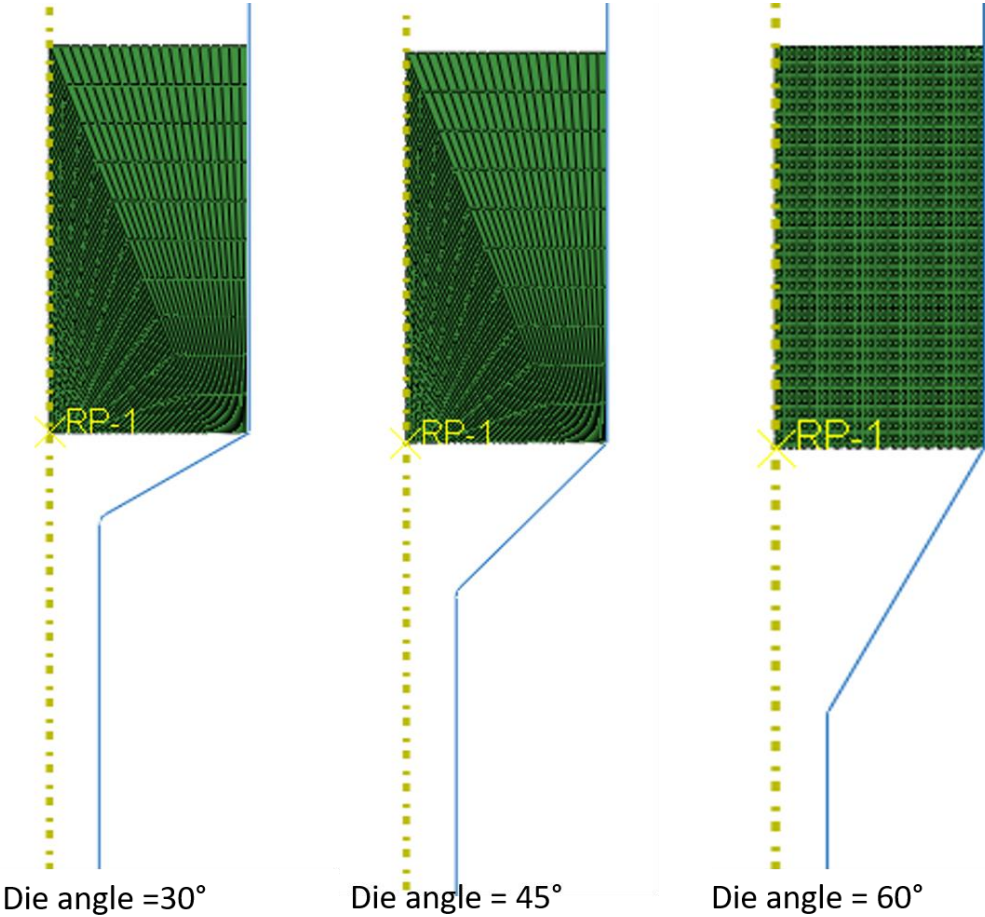Figure 52. Finite element models with extrusion area ratio 16:1. (a) die angle 30°, (b) die angle 45°, (c) die angle 60°.
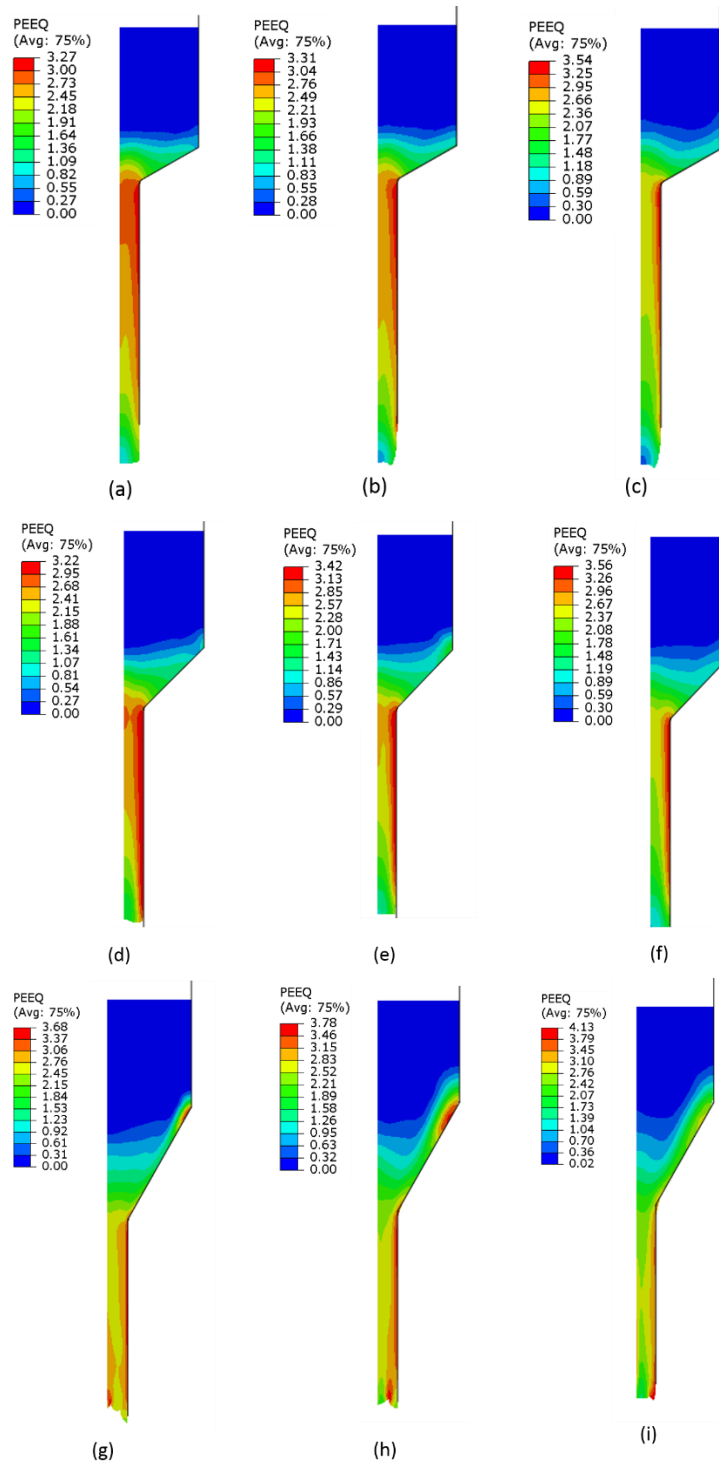
Figure 53. Equivalent plastic strain contours of finite element model for the extrusion area ratio 16:1. (a) Die angle 30°, friction coefficient $\mu = 0$; (b) Die angle 30°, $\mu = 0.05$; (c) Die angle 30°, $\mu = 0.1$; (d) Die angle 45°, $\mu = 0$; (e) Die angle 45°, $\mu = 0.05$; (f) Die angle 45°, $\mu = 0.1$; (g) Die angle 60°, $\mu = 0$; (h) Die angle 60°, $\mu = 0.05$; (i) Die angle 60°, $\mu = 0.1$.
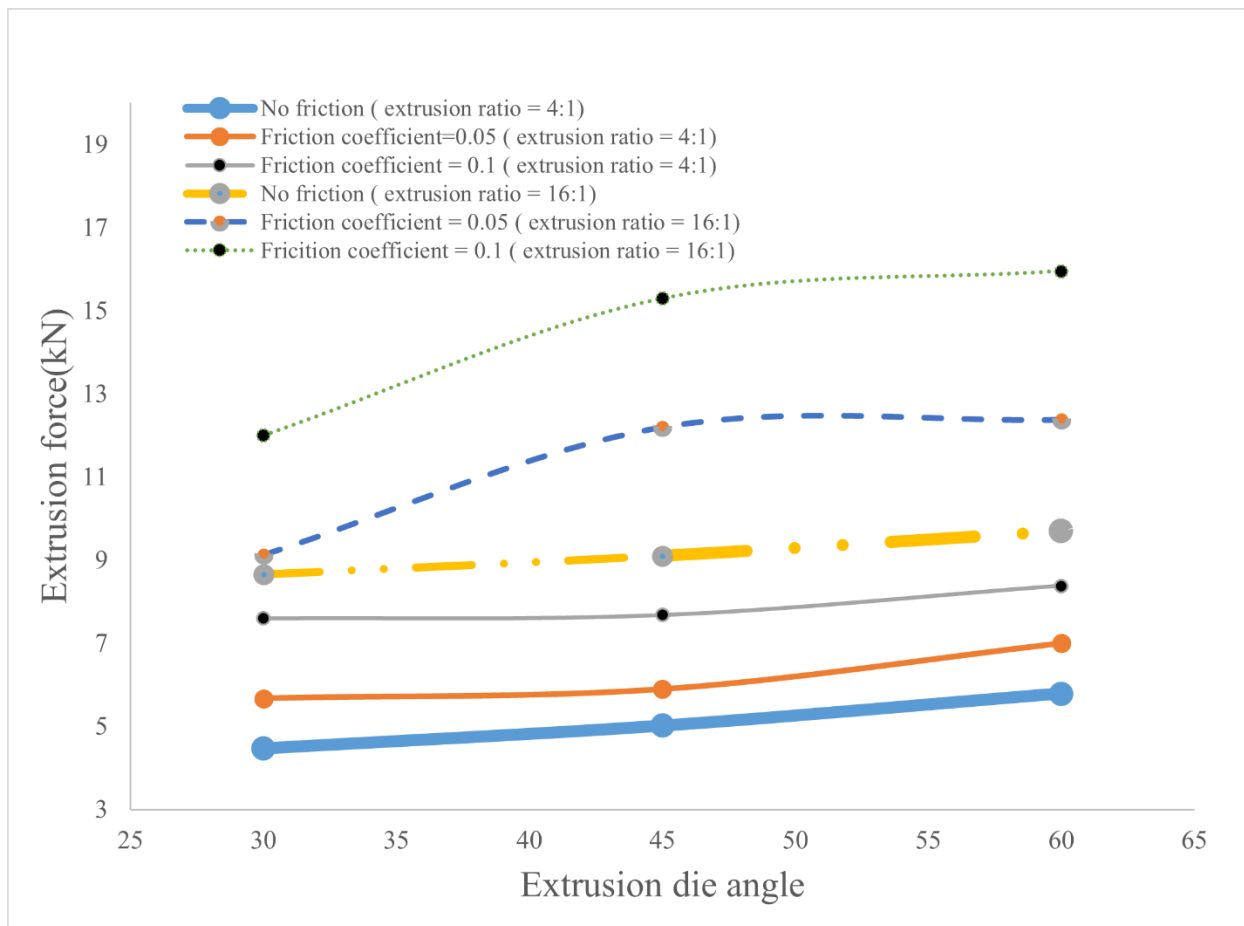
Figure 54. A summary of extrusion forces from finite element model simulations for extrusion area ratio of 4:1 and 16:1

4.3.2 Extrusion Area Ratio 4:1

Nine finite element models with different extrusion angles and different friction coefficients were built to simulate extrusion process under extrusion area ratio of 4:1. Finite element models of different extrusion angles were illustrated in Figure 55.

Figure 56 shows that the maximum equivalent plastic strains are 4.04, 5.83 and 2.6 under the die angle of 30°, 45° and 60°, respectively. The maximum equivalent plastic strain under die angle

$60°$ is under the stable status, so its strain magnitude is less than others. They were simulated under three different friction coefficients of $\mu = 0, 0.5, 0.1$, respectively. One can see that the material deformed more severely and more locally under the higher die angle condition and higher friction.
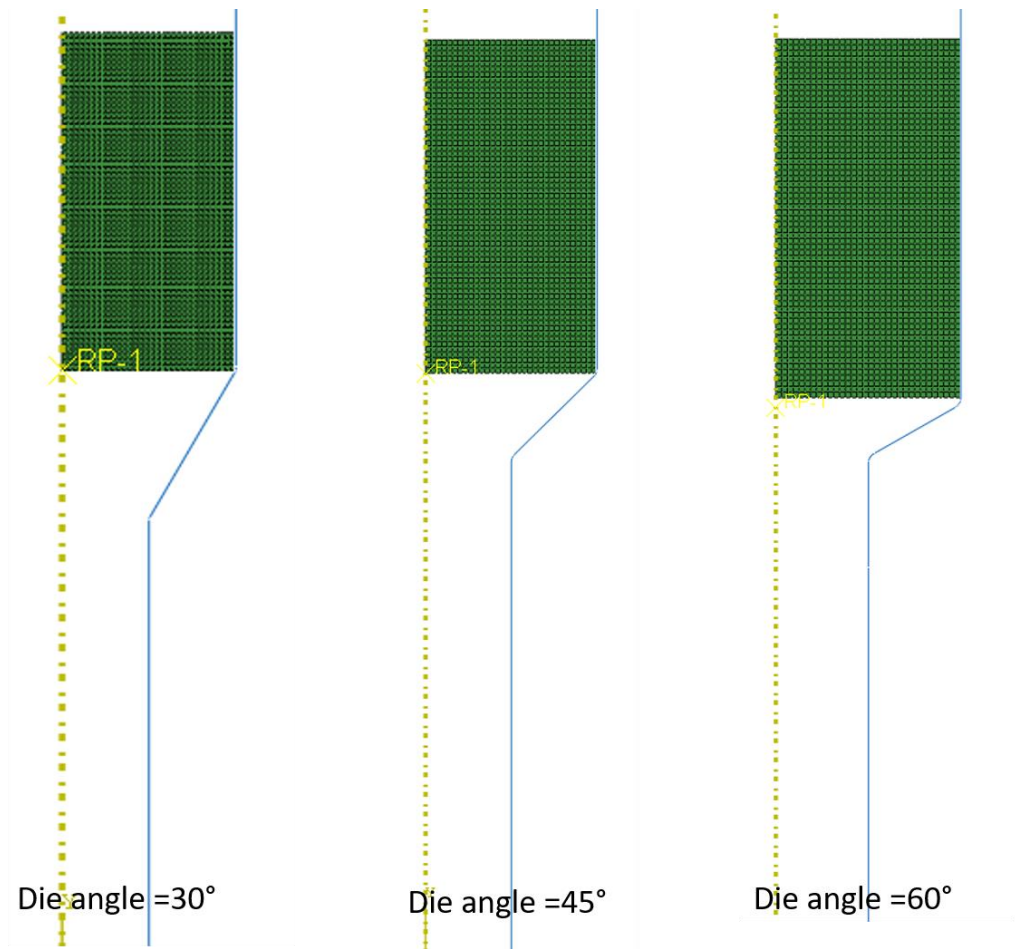
Figure 55. Finite element models with extrusion area ratio 4:1. (a) die angle 30°, (b) die angle 45°, (c) die angle 60°.
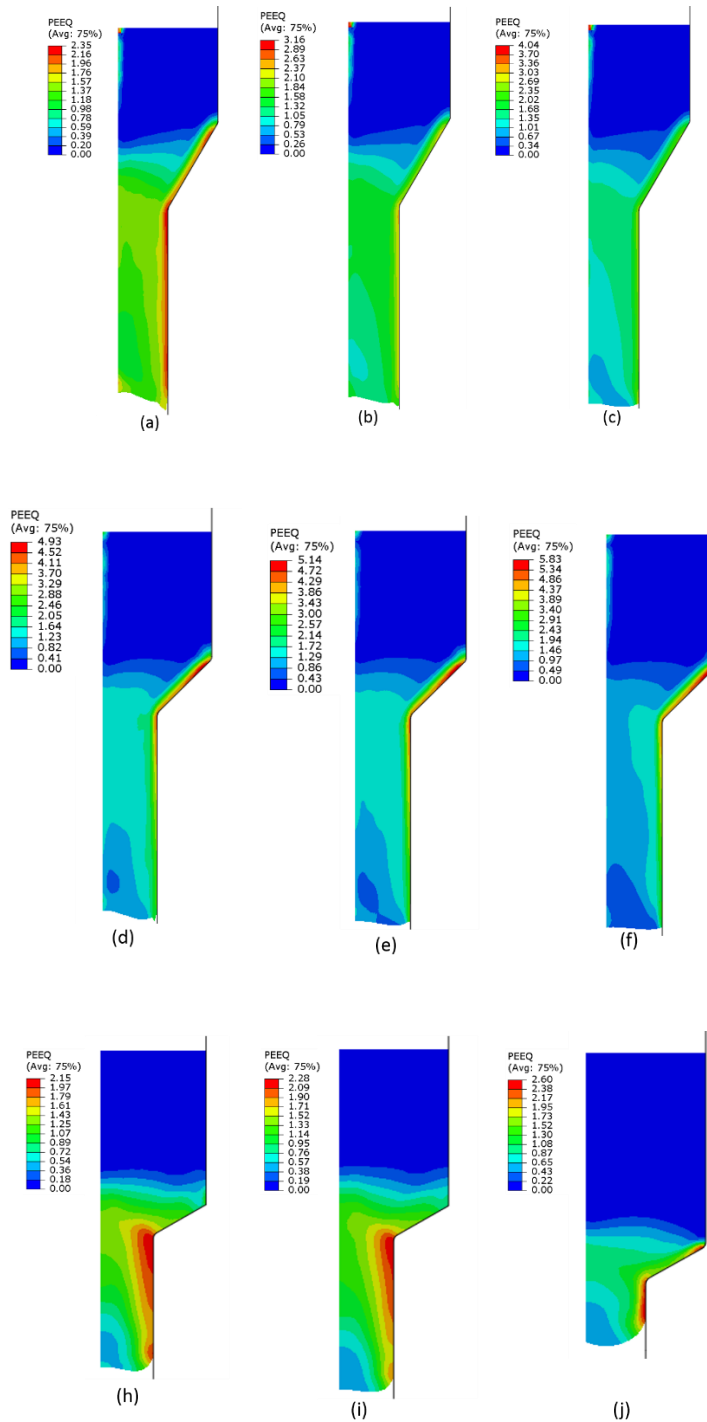
Figure 56. Equivalent plastic strain contours of finite element model for the extrusion area ratio 4:1. (a) Die angle 30°, friction coefficient $\mu = 0$; (b) Die angle 30°, $\mu = 0.05$; (c) Die angle 30°, $\mu = 0.1$; (d) Die angle 45°, $\mu = 0$; (e) Die angle 45°, $\mu = 0.05$; (f) Die angle 45°, $\mu = 0.1$; (g) Die angle 60°, $\mu = 0$; (h) Die angle 60°, $\mu = 0.05$; (i) Die angle 60°, $\mu = 0.1$.
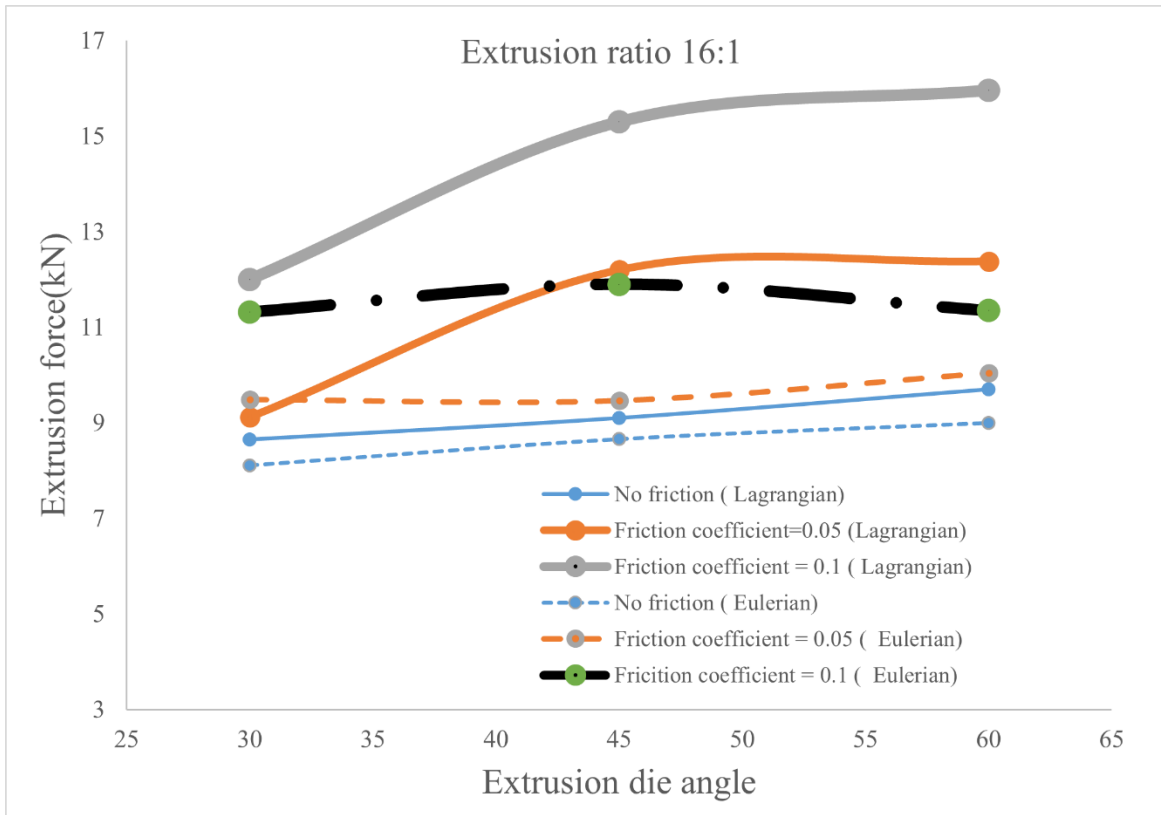
Figure 57. A summary of extrusion forces from finite element model simulations of Eulerian and Lagrangian method for extrusion area ratio of 16:1
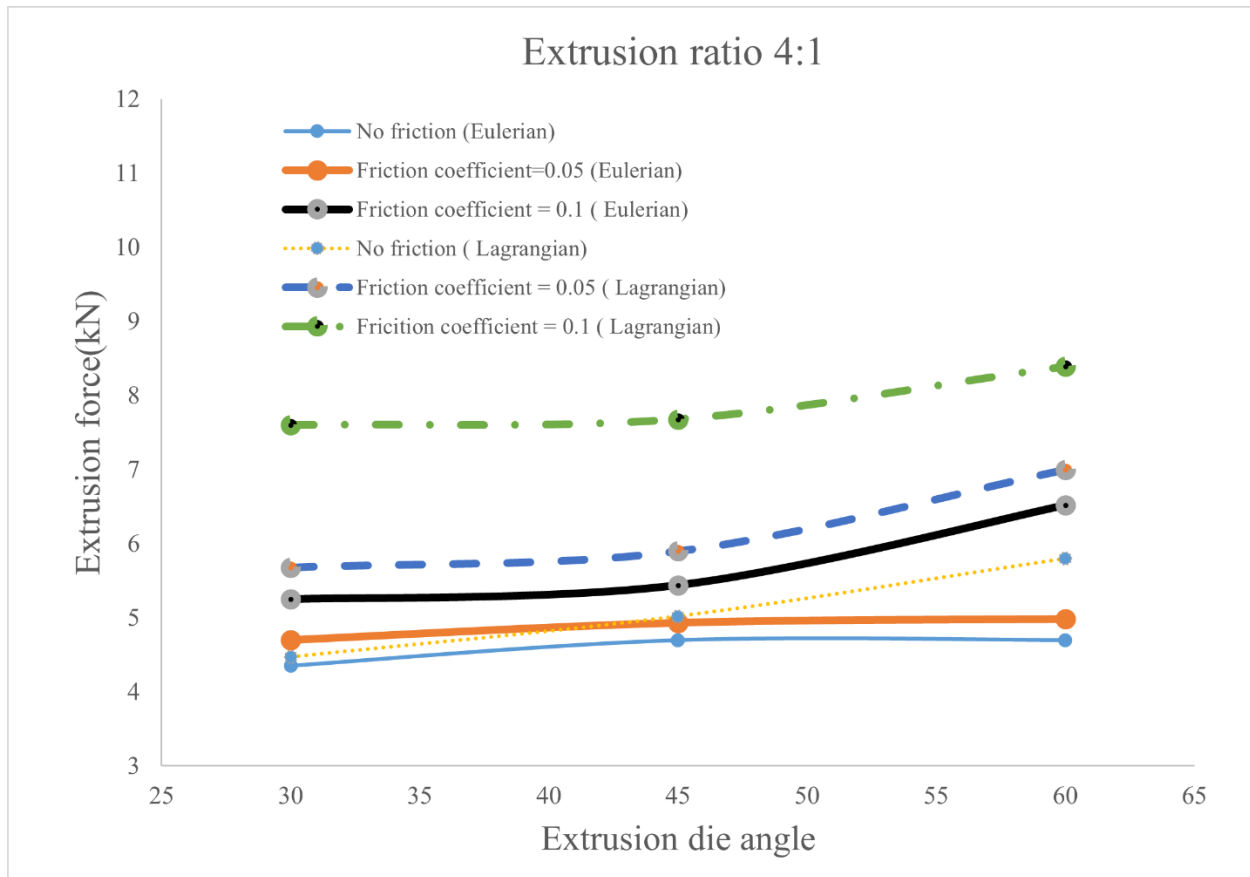
Figure 58. A summary of extrusion forces from finite element model simulations of Eulerian and Lagrangian method for extrusion area ratio of 4:1

Table 10. Extrusion force comparisons between different conditions

Extrusion ratio		16-1			4-1		
Die angle		30	45	60	30	45	60
Friction coefficient μ = 0	Eulerian	8.1	8.7	9.0	4.4	4.7	4.7
	Lagrangian	8.7	9.1	9.7	4.5	5.0	5.8
	Error(%)	6.2	4.8	7.2	2.7	6.4	19.0
Friction coefficient μ = 0.05	Eulerian	9.5	9.5	10.1	4.7	4.9	5.0
	Lagrangian	9.1	12.2	12.4	5.7	5.9	7.0
	Error(%)	-4.1	22.4	18.8	17.3	16.4	28.9
Friction coefficient μ = 0.1	Eulerian	11.3	11.9	11.4	5.3	5.4	6.5
	Lagrangian	12.0	15.3	16.0	7.6	7.7	8.4
	Error(%)	5.7	22.2	28.9	30.9	29.2	22.3

4.4 Material Deformation Study under Wire Extrusion Process

Lagrangian method can provide the simulation process from the start to the end during the wire extrusion process. Simulation results with Lagrangian method can clearly describe the deformation process of the billet material.
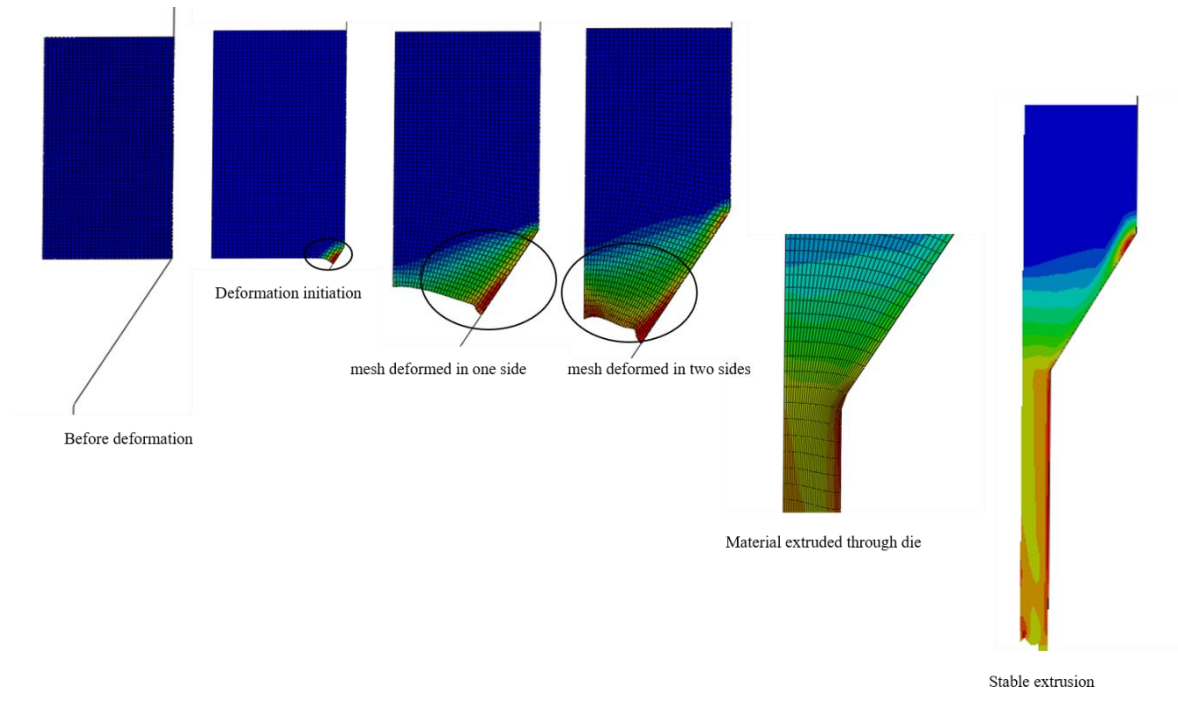
Figure 59. Material deformation under wire extrusion with extrusion ratio 16:1 and die angle 30º.
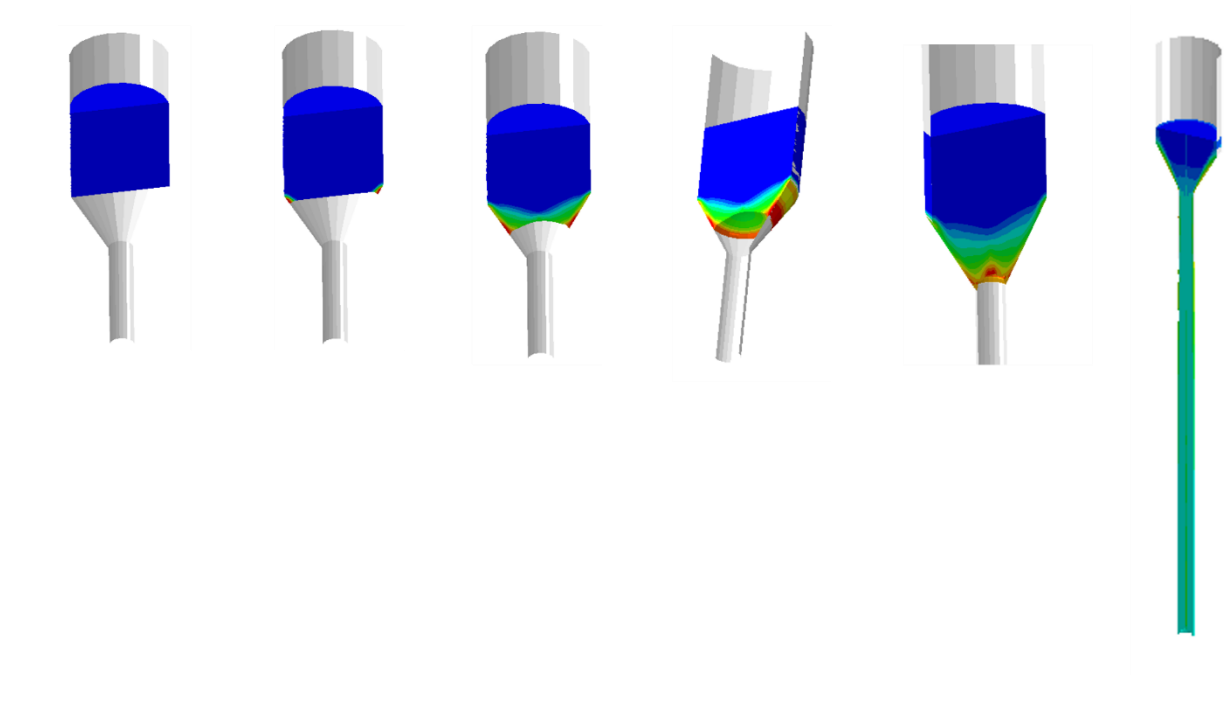
Figure 60. Material deformation under wire extrusion with extrusion ratio 16:1 and die angle 30º in 3D dimension.
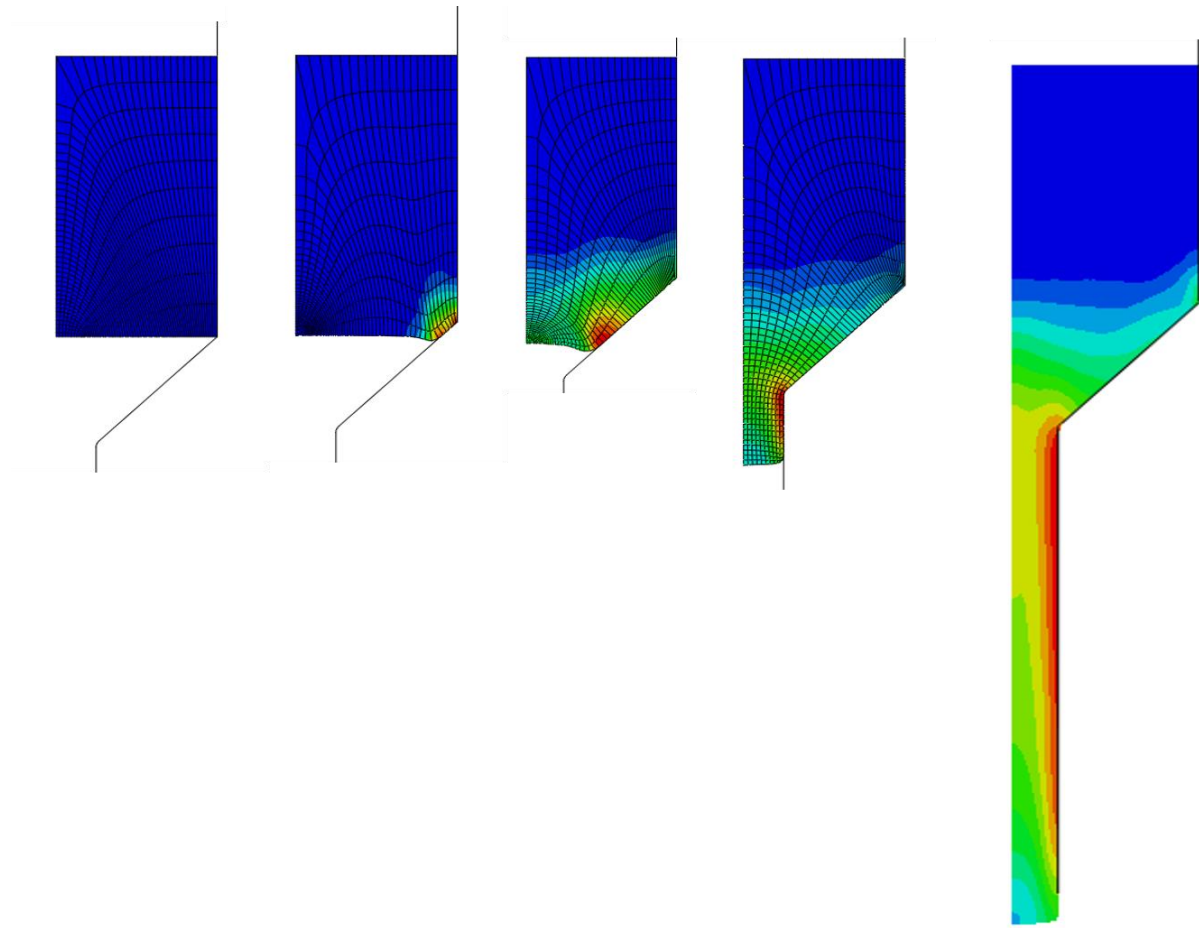
Figure 61. Material deformation under wire extrusion with extrusion ratio 16:1 and die angle 45°
in 2D dimension.
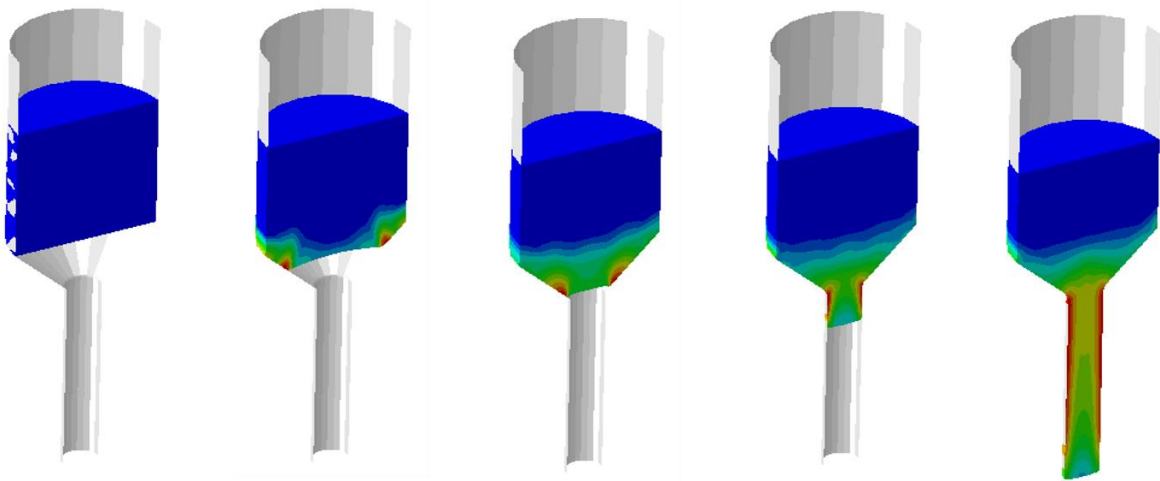
Figure 62. Material deformation under wire extrusion with extrusion ratio 16:1 and die angle 45º in 3D dimension.

Figure 63. Material deformation under wire extrusion with extrusion ratio 16:1 and die angle 60º

in 2D dimension.

Figure 64. Material deformation under wire extrusion with extrusion ratio 16:1 and die angle 60º in 3D dimension.

Figure 65. Material deformation under wire extrusion with extrusion ratio 4:1 and die angle 30º in 2D dimension.
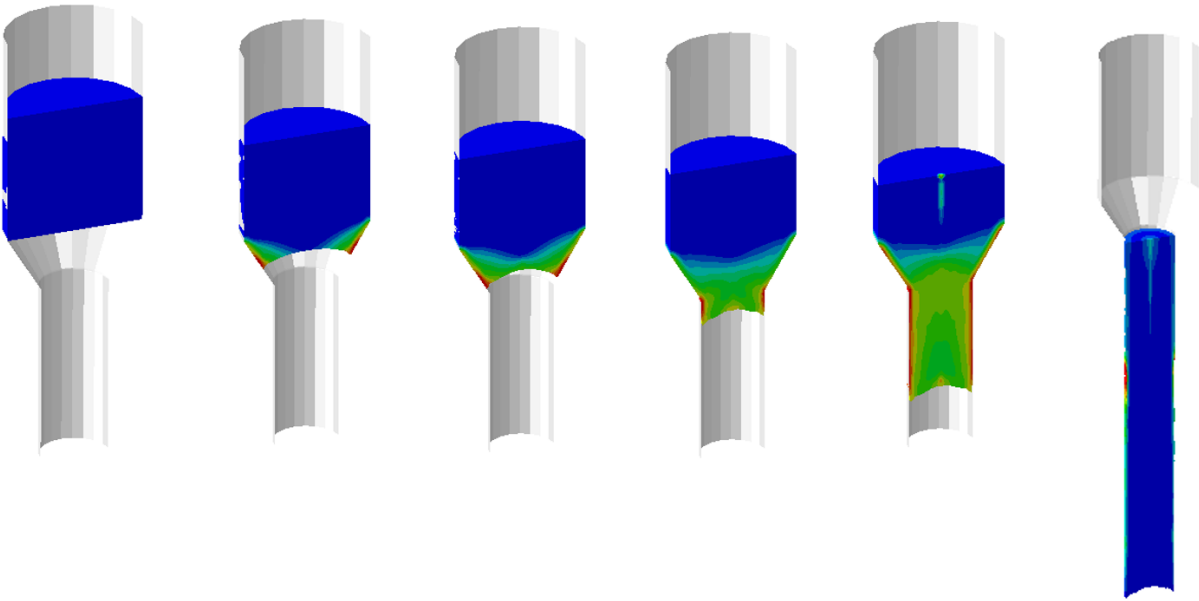
Figure 66. Material deformation under wire extrusion with extrusion ratio 4:1 and die angle 30º in 3D dimension.
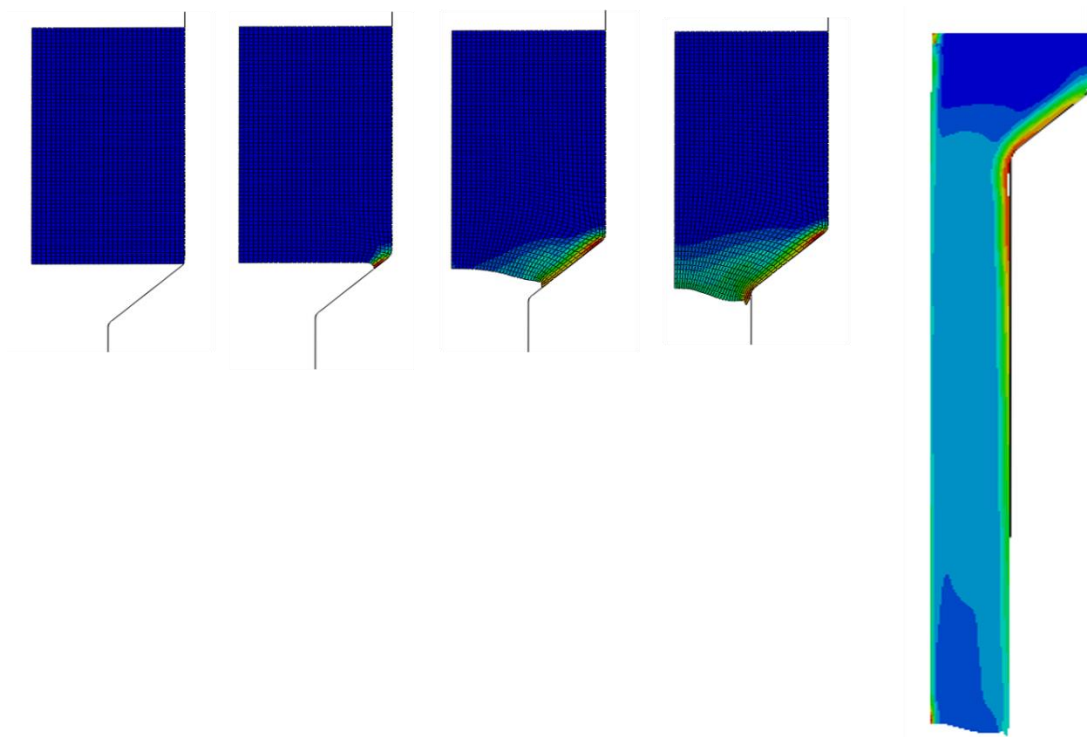
Figure 67. Material deformation under wire extrusion with extrusion ratio 4:1 and die angle 45º in 2D dimension.

Figure 68. Material deformation under wire extrusion with extrusion ratio 4:1 and die angle 45° in 3D dimension.
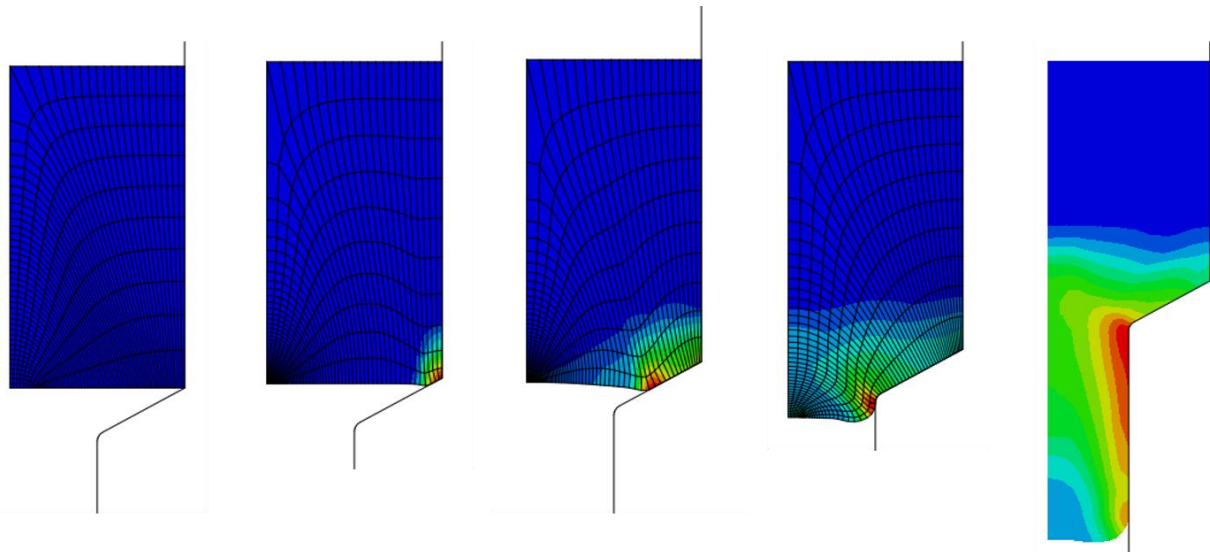
Figure 69. Material deformation under wire extrusion with extrusion ratio 4:1 and die angle 60° in 2D dimension.
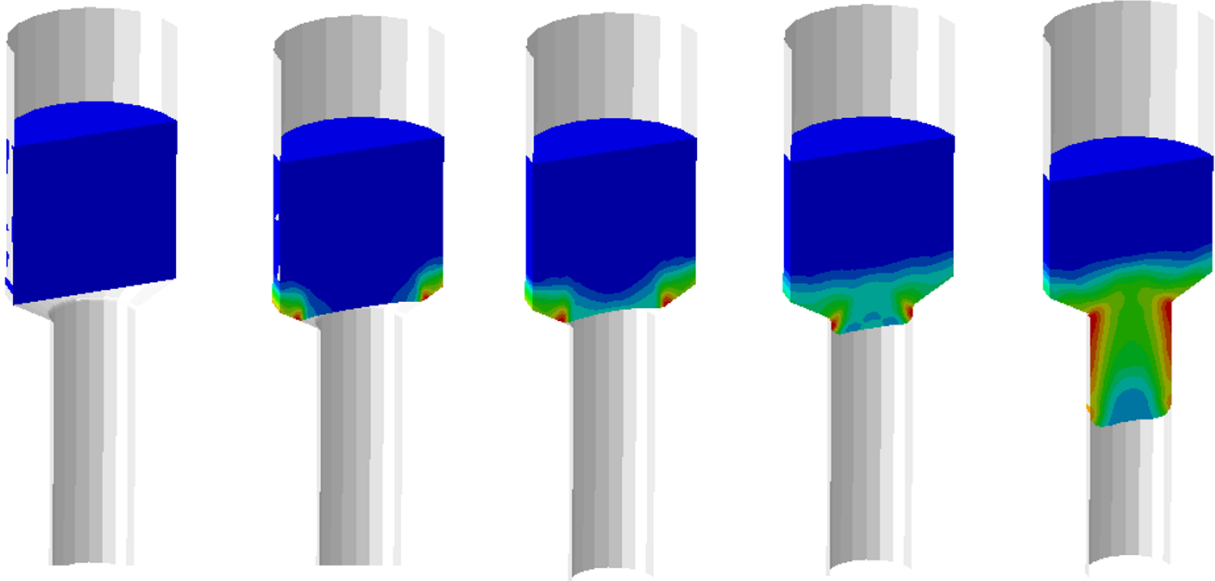
Figure 70. Material deformation under wire extrusion with extrusion ratio 4:1 and die angle 60° in 3D dimension.

<div align="center">

4.5 Analytical Solutions

</div>

For the extrusion force calculation, William Johnson and Mellor (1983) described the slip line field theory in their book in order to estimate the extrusion pressure on the wedged shape die. Jagabandhu Chakrabarty also introduced an analytical solution of the extrusion pressure in his book. These two solutions are summarized in the following Eq. (23) (Johnson and Mellor) and Eq. (24) (Chakrabarty), respectively.

$$F = \pi\sigma_y(1+\alpha)\frac{r_i-r_0}{r_i}r_i(r_i+r_0) \tag{23}$$

$$F = 2\pi\sigma_y\left(1-\frac{r_0}{r_i}\right)(1+\sin\alpha){r_i}^2 \tag{24}$$

Here σ_y is the yield stress of material, α is the die angle of extrusion die, r_i is the entry radius of extrusion die, and r_0 is the exit radius of extrusion.

The comparison results between these two solutions and FEA results for the extrusion area ratios of 4:1 and 16:1 are shown in Table 11 and Table 12. The prediction error percentages with respect to FEA results are also included in the tables. One can conclude that the two analytical solution are not very accurate compared with FEA results.

Table 11. Extrusion force comparisons for extrusion area ratio 4:1.

Die angle (°)	FEA (kN)	Slip line theory (Johnson (1983))		Literature solution (Chakrabarty (2010))	
		Force (kN)	Error (%)	Force (kN)	Error (%)
30	4.4	3.3	26	4.3	3
45	4.7	3.8	19	4.9	4
60	4.7	4.4	7	5.3	13

Table 12. Extrusion force comparisons for extrusion area ratio 16:1.

Die angle (°)	FEA (kN)	Slip line theory (Johnson (1983))		Literature solution (Chakrabarty (2010))	
		Force (kN)	Error (%)	Force (kN)	Error (%)
30	8.1	4.1	50	6.4	21
45	8.7	4.8	45	7.3	15
60	9.0	5.5	39	8.0	11

<u>4.6 An Energy Conservation Based Analytical Solution</u>

In this section, a new analytical solution to predict the extrusion force under different friction conditions will be presented. Energy conservation within a control volume is used. There are two boundary conditions for the extrusion process in the following discussion. One is frictionless or no friction condition, and the other one is friction condition. For simplicity, the friction force is applied only on the interface between the sample and the inclined wall of the extrusion die. An illustration of extrusion is shown in Figure 71.
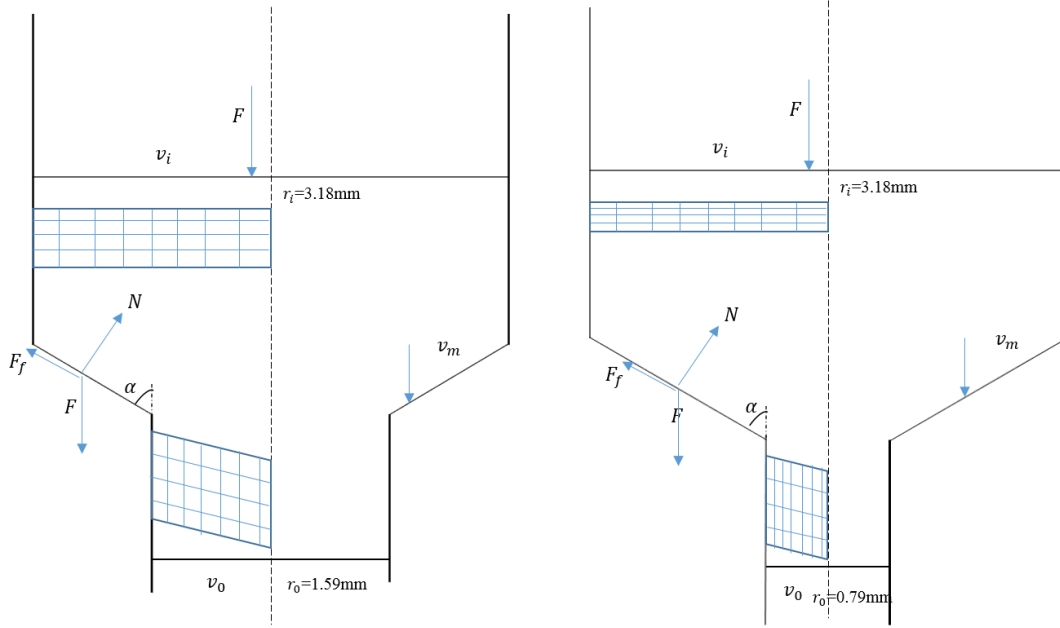
Figure 71. Two extrusion sketches for extrusion area ratios of 4:1(left) and 16:1(right).

For no friction condition,

$$Fv_i = \sigma_y \varepsilon_p \pi r_0^2 v_0 \tag{25}$$

where F is the force applied on the top of the sample; v_i is the entry velocity of the sample; σ_y is the material yield strength (assuming rigid perfect plasticity); ε_p is the equivalent plastic strain of the material introduced during the extrusion process; and v_0 is the exit velocity of the sample. Note that the kinematic energy and elastic strain energy of the sample are neglected.

For friction condition,

$$Fv_i = \sigma_y \varepsilon_p (\pi r_0^2 v_0) + F_f v_m cos\alpha \tag{26}$$

where F_f is the total friction force between the inclined wall of the extrusion die and the sample; v_m is the average sliding velocity of the sample on the extrusion die from the entry to the exit; α is the die angle of the extrusion die.

From the vertical force equilibrium condition,

$$Nsin\alpha + \mu Ncos\alpha = F \qquad (27)$$

where N is the vertical support force of the slope surface of the extrusion die; μ is the friction coefficient of the surface between the extrusion wall and the sample.

From Eq. (27), we get

$$N = \frac{F}{sin\alpha + \mu cos\alpha}. \qquad (28)$$

Assuming a constant friction coefficient of μ, the friction force of the slope surface of the extrusion die becomes.

$$F_f = \mu N = \frac{\mu F}{sin\alpha + \mu cos\alpha} \qquad (29)$$

In order to obtain the amount of plastic strain during extrusion, ε_p , we have strain components defined as follows.

$$\varepsilon_{rr} = ln\left(\frac{r_0}{r_i}\right) \qquad (30)$$

$$\varepsilon_{\theta\theta} = \varepsilon_{rr} = ln\left(\frac{r_0}{r_i}\right) \qquad (31)$$

$$\varepsilon_{zz} = -\varepsilon_{rr} - \varepsilon_{\theta\theta} = -2ln\left(\frac{r_0}{r_i}\right) \qquad (32)$$

$$\gamma_{rz} = tan\alpha(\varepsilon_{rr}) = tan\,\alpha\left(ln\left(\frac{r_0}{r_i}\right)\right) \qquad (33)$$

Here, r_i is the radius of the extrusion die entry or the sample, and r_0 is the radius of the extrusion die or the sample extruded.

For no friction condition,

$$\dot{\varepsilon}_{rr}^p = \frac{v_n \cos\alpha}{r} \tag{34}$$

$$\dot{\gamma} = \frac{v_n \sin\alpha}{r} \tag{35}$$

Thus,

$$\dot{\gamma} = \dot{\varepsilon}_{rr} \tan\alpha \tag{36}$$

And the equivalent strain rate is

$$\dot{\bar{\varepsilon}} = \sqrt{\frac{2}{3}\dot{\varepsilon}_{ij}^p \dot{\varepsilon}_{ij}^p} = \sqrt{\frac{2}{3}\left[\left(\dot{\varepsilon}_{rr}^p\right)^2 + \left(\dot{\varepsilon}_{rr}^p\right)^2 + 4\left(\dot{\varepsilon}_{rr}^p\right)^2 + 2\left(\frac{1}{2}\right)^2 (\tan\alpha)^2 (\dot{\varepsilon}_{rr}^p)^2\right]} =$$

$$\sqrt{\frac{2}{3}\left[6 + \frac{1}{2}(\tan\alpha)^2\right]}\,\dot{\varepsilon}_{rr}^p \tag{37}$$

Thus,

$$\varepsilon_p = \bar{\varepsilon} = \sqrt{4 + \frac{1}{3}(\tan\alpha)^2}\,\ln\frac{r_i}{r_0} \tag{38}$$

From (26), (29) and (38), we have $Fv_i = \sigma_y \varepsilon_p (\pi r_0^2 v_0) + \dfrac{\mu F}{\sin\alpha + \mu\cos\alpha} v_m \cos\alpha$

$$= \sigma_y \pi r_0^2 v_0 \sqrt{4 + \frac{1}{3}(\tan\alpha)^2}\,\ln\left(\frac{r_i}{r_0}\right) + \frac{\mu F}{\sin\alpha + \mu\cos\alpha} v_m \cos\alpha \tag{39}$$

Thus, we can solve the F and obtain the following equation,

$$F = \frac{\sigma_y \pi r_i^2 \sqrt{4 + \frac{1}{3}(\tan\alpha)^2}\,\ln\left(\frac{r_i}{r_0}\right)}{1 - \frac{\mu\cos\alpha}{\sin\alpha + \mu\cos\alpha}\frac{v_m}{v_i}} \tag{40}$$

where,

90

$$\frac{v_m}{v_i} = \sqrt{\frac{3r_i^3}{(r_i^2 + r_0^2 + r_i r_0)r_0}} \tag{41}$$

Note that the Eq (41) was derived under the assumption of same kinematic energy (T). An incremental mass element (dm) inside the die is shown in Figure 72.
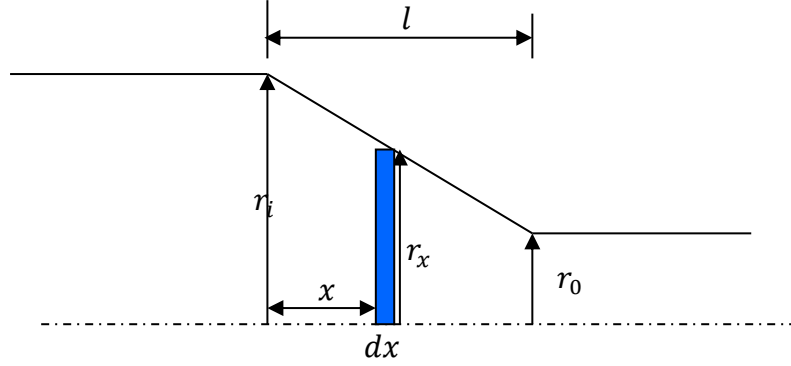
Figure 72. An incremental element inside the die of wire extrusion process.

$$v_x = \left(\frac{r_i}{r_x}\right)^2 v_i \tag{42}$$

$$dm = \rho dV = \rho \pi r_x^2 dx \tag{43}$$

$$dT_x = \frac{1}{2} dm v_x^2 = \frac{1}{2} \rho \pi r_x^2 dx \left[\left(\frac{r_i}{r_x}\right)^2 v_i\right]^2 \tag{44}$$

From geometry similarity, we have the following equation.

$$\frac{r_x - r_0}{r_i - r_0} = \frac{l - x}{l} \tag{45}$$

The total material mass at the die is $m = \int_0^l dm$, and the total kinematic energy is $T = \int_0^l dT_x$. Both m and T can be calculated from the above Eq. (43) and Eq. (44). Assuming the same total kinematic energy, $T = \frac{1}{2} m v_m^2$. We get the following equation.

91

$$v_m = \sqrt{\frac{2T}{m}} = \sqrt{\frac{3r_i^3}{(r_i^2 + r_0^2 + r_i r_0)r_0}}\, v_i \tag{46}$$

Thus, we can derive the Eq (41). According to equation (40), we have

$$F = \frac{\sigma_y \pi r_i^2 \sqrt{4 + \frac{1}{3}(tan\alpha)^2}\, ln\left(\frac{r_i}{r_0}\right)}{1 - \frac{\mu cos\alpha}{sin\alpha + \mu cos\alpha}\sqrt{\frac{3r_i^3}{(r_i^2 + r_0^2 + r_i r_0)r_0}}} \tag{47}$$

This is the final analytical solution we obtain, and further discussions on the shear strain term $(tan\alpha)$ will be presented in the section 4.8.

4.7 Comparisons of Extrusion Forces among Analytical Solution, Finite Element Model, and Test Data

Extrusion forces for the die's die angle of 30°, 45° and 60° under the extrusion area ratios of 4:1 and 16:1 is compared among analytical solution, FEA model and test data. The extrusion die dimension is also shown in the Figure 34. Friction coefficient 0.00, 0.05 and 0.10 are considered in the analytical solution model and FEA model. Generally, the friction coefficient range is considered as less than 0.1 as Groche and Kramer (2018) introduced . Figure 36 and Figure 37 show the extrusion forces for different extrusion die angles with the extrusion area ratios of 4:1 and 16:1. The error between analytical solution and FEA model is below 2kN. Test data is also shown in the following picture of extrusion area ratio 16:1 in order to compare the extrusion force value with the analytical solution and FEA model. One can conclude that there is a good match, especially for no friction condition and low friction coefficient condition (0.05).
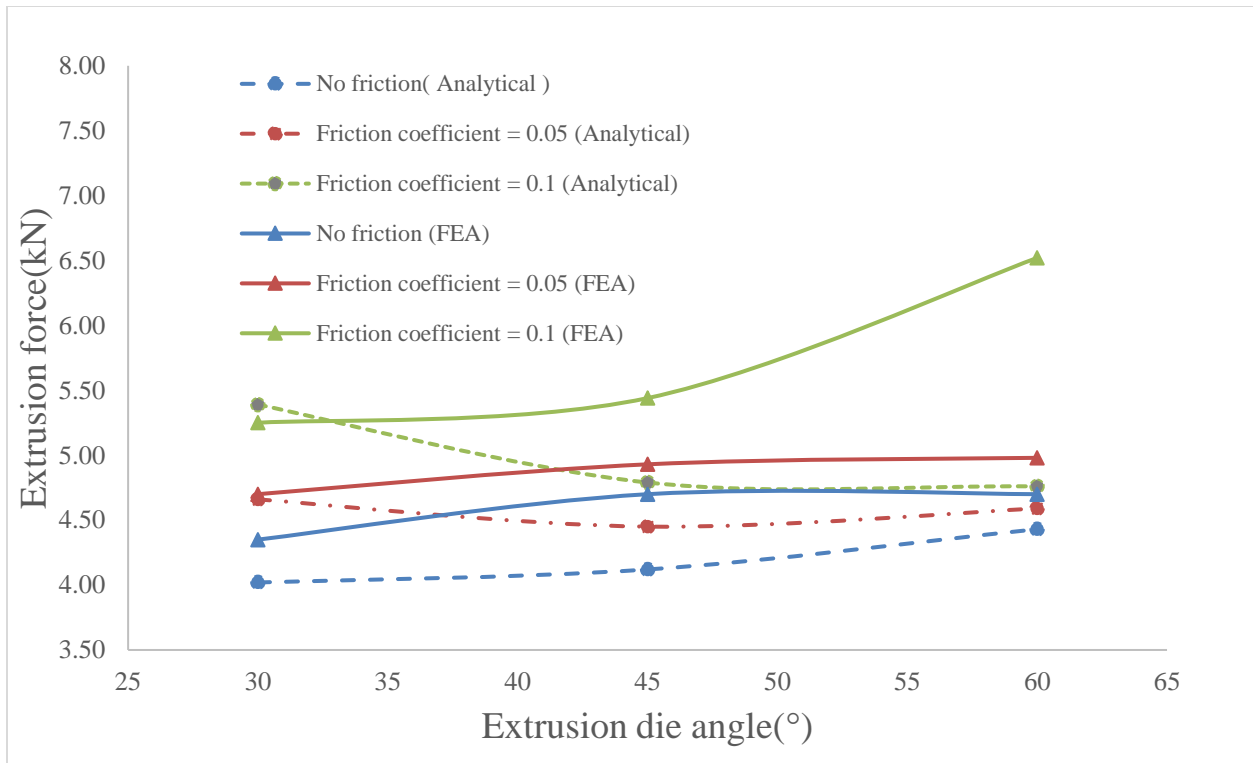
Figure 73. Comparison of extrusion forces among analytical solution, FEA model for the extrusion area ratio 4:1.
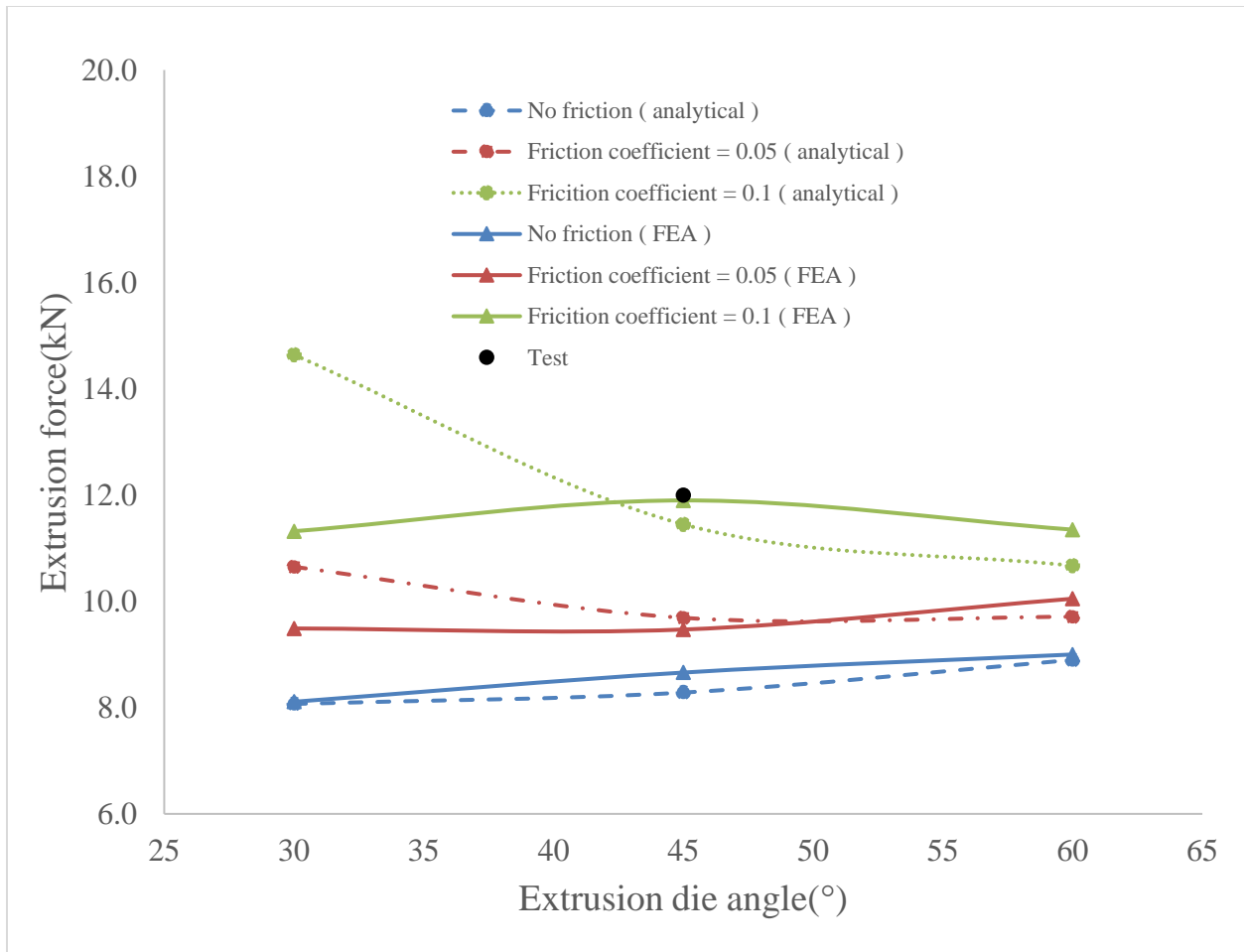
Figure 74. Comparison of extrusion forces among analytical solution, FEA model, and test data for the extrusion area ratio 16:1.

To make a better conclusion, extrusion forces from analytical solution, the classical slip line theory, FEA model and the literature solution introduced are compared each other under no friction condition. Note that the slip line theory and the literature solution are constructed in the ideal smooth boundary between the sample and the extrusion die slope surface which is frictionless. From Figure 75 and Figure 76, one can see that analytical solution developed in this paper is much better than slip line theory and literature solution for extrusion area ratio 4:1 and 16:1. For extrusion area ratio 4:1, analytical solution is much closer to finite element result than other

94

methods under the die angle 60°. For extrusion area ratio 16:1, the analytical solution is very close

to the result of FEA model, and the slip line theory and literature solution are largely less than the

result of finite element model.
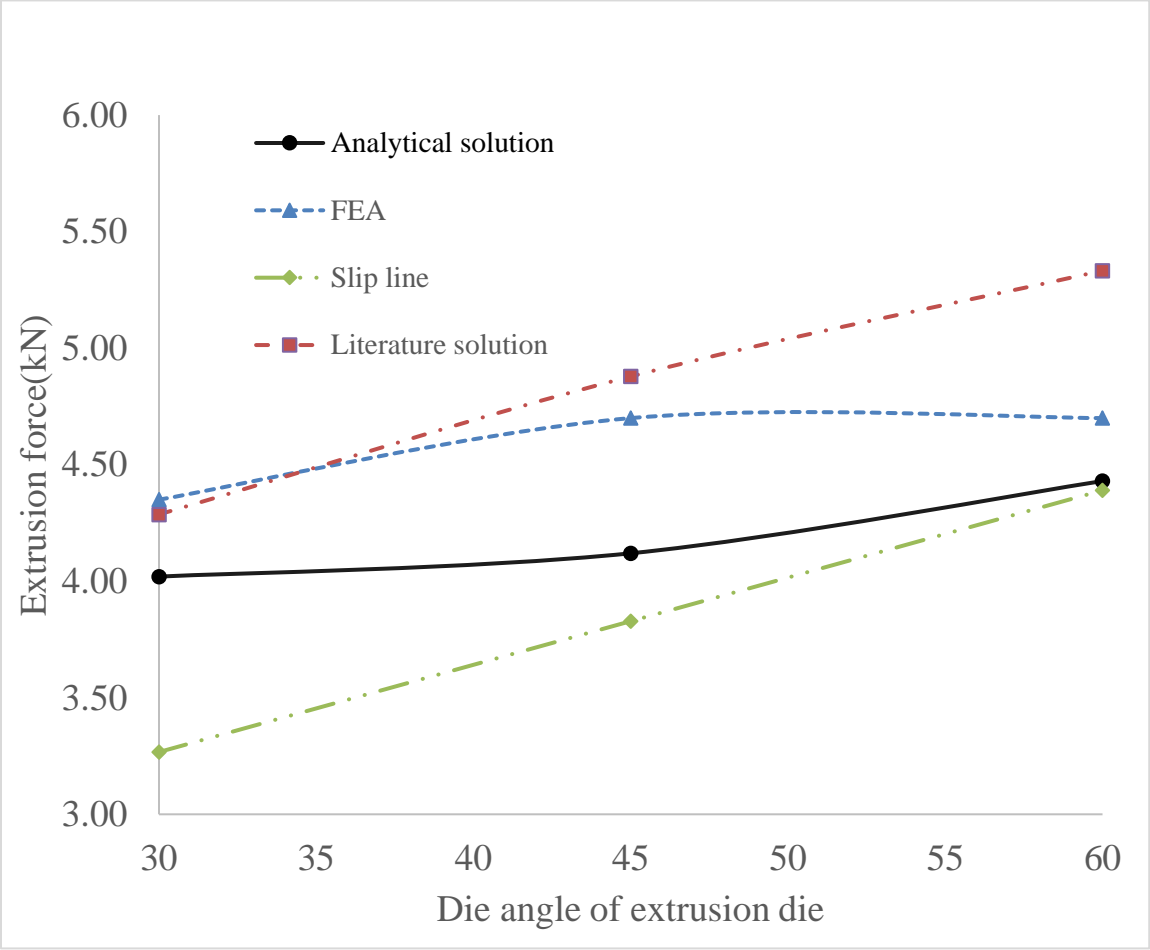
Figure 75. Comparison of extrusion forces among the analytical solution (Eq.(47)), FEA, the slip line theory (Eq.(23)), and the literature solution (Eq.(24)) under the extrusion area ratio 4:1 and frictionless condition.
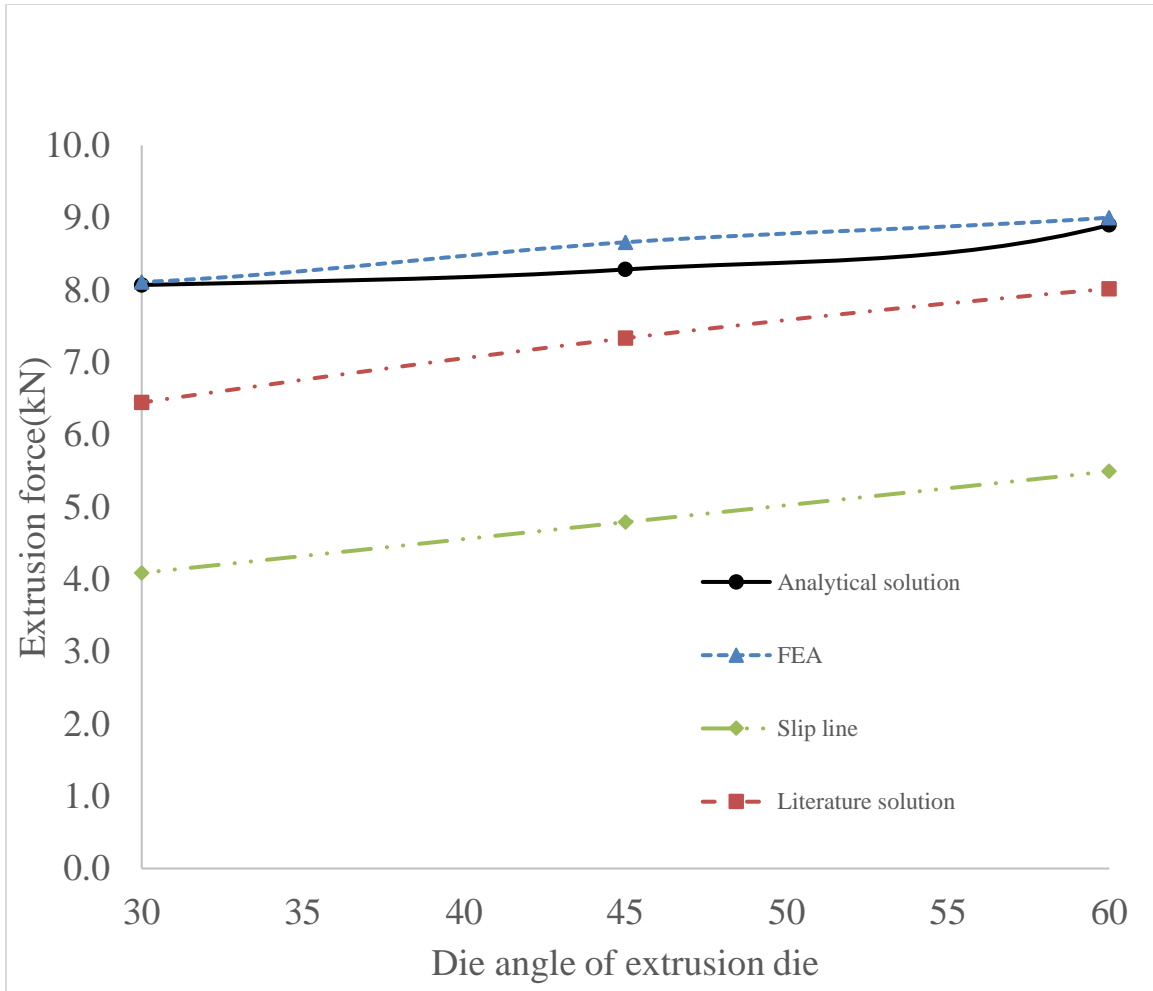
Figure 76. Comparison of extrusion forces among the analytical solution (Eq.(47)), FEA, the slip line (Eq.(23)), and the literature solution (Eq.(24)) under the extrusion area ratio 16:1 and frictionless condition.

4.8 Discussion

In this section, two important parameters in our study will be further discussed, including the die angle and the real yield stress of Al/CNT nano composites.

4.8.1 Discussion on Die Angles

To understand the effect of extrusion die angle on the extrusion force, three die angles (30°, 45° and 60°) were investigated in this paper. The above die angles are more widely used than others of very small or very large extrusion die angles. The above analytical solution is suitable for the

die angle ranging from 30° to 60°. It may be not very suitable for the extrusion die angles outside 30° to 60°. Some modifications will be needed especially for the extreme angle conditions, such as those close to 0° or 90°. One of the main reasons is that the shear strain (Eq. (33)) plays a key role on those extrusion processes. For example, it is noted that when the die angle α is approaching to $\frac{\pi}{2}$, the assumption of shear strain component in Eq. (33) may cause trouble since $\tan\left(\frac{\pi}{2}\right) \rightarrow \infty$. So, the term of $tan\alpha$ can be replaced by $\tan\left(\alpha\left[1-\left(\frac{\alpha}{\pi}\right)^2\right]\right)$. An alternative extrusion force solution with patch becomes as follows.

$$F = \frac{\sigma_y \pi r_i^2 \sqrt{4+\frac{1}{3}\left(\tan\left(\alpha\left[1-\left(\frac{\alpha}{\pi}\right)^2\right]\right)\right)^2} \ln\left(\frac{r_i}{r_0}\right)}{1-\frac{\mu cos\alpha}{sin\alpha+\mu cos\alpha}\sqrt{\frac{3r_i^3}{(r_i^2+r_0^2+r_ir_0)r_0}}} \tag{48}$$

Also, many researchers used different equations to derive the extrusion force for different conditions of the extrusion dies. Chakrabarty considered whether the radius ratio of the extrusion die is moderate or not compared with the extrusion die angle and deduced two extrusion force analytical solutions for different boundary conditions.

4.8.2 Discussion on the Difference between Pure Metal and Metal/CNTs

Pure copper and pure aluminum wire extrusion tests were conducted as well as Cu/CNTs under elevated temperature conditions. The extrusion forces are shown in Figure 44. As we can see from Figure 44, temperature is a key factor that can affect the extrusion force for different materials. Even if Cu/CNT's strength in the room temperature is higher than strength of Cu and Al. The extrusion force of Cu/CNT sample is lower than those of Cu and Al because of its higher extrusion temperature condition.

From Figure 44, one can identify stable extrusion forces for Cu, Al and Cu/CNT. For example, the extrusion force is 8.2kN for Cu/CNT material. From Eq. (48), we can get the yield stress of Cu, Al and Cu/CNT during the extrusion process. The analytical solution provides an alternative way to quickly estimate what the yield stress of material during the extrusion process from the new analytical solution.

CHAPTER 5 CONCLUSIONS AND FUTURE STUDIES

5.1 Summary of Contribution

In this dissertation, powder compaction and wire extrusion manufacturing process were investigated thoroughly for experiments, simulation models and analytical solutions. Al, Cu powder compaction tests and Al, Cu, Cu/CNTs wire extrusion tests were conducted with MTS system. Finite element models were built to explore the mechanics mechanism of the material deformation during powder compaction and wire extrusion processes. The results of finite element model had a good match with test data. Analytical solutions for powder compaction and wire extrusion were developed to predict the compaction pressure in an accurate and fast way. The main contributions in this dissertation are the following contents:

- Designed powder compaction dies with different diameters and designed extrusion dies with different extrusion ratios for different materials Al, Cu and Cu/CNTs. Die with Inconel steel material was designed for elevated temperature conditions. Developed heater systems to build the elevated temperature conditions up to 800ºC. Designed vibration loading conditions with MTS system to improve material density ratio and strength of material during powder compaction process. Developed a two-stage wire extrusion process to fabricate wires while improving material density ratio of Cu/CNT from 0.92 to 0.98.

- Built finite element models with Drucker Prager Cap material constitutive model to simulate powder compaction process. Material parameters were calibrated with only a powder compaction test and simulation models. Wire extrusion simulation models with Eulerian and Lagrangian methods were used to simulate the wire extrusion process. Finite element models with Lagrangian method can simulate the whole wire extrusion process

from the entry of the die to the exit of its, which can be used to predict material fracture during wire extrusion.

- Proposed two innovative analytical solutions to predict the density ratio of material made by powder compaction, and to calculate the extrusion force for wire extrusion. These two analytical solutions can provide very fast and accurate prediction for both powder compaction and wire extrusion.

5.2 Recommended Future Studies

In the present dissertation, powder compaction and wire extrusion dies were designed. Finite element models were built to simulate the powder compaction process, and a series of experiments are conducted. Some experiment methods were introduced to increase relative density ratio of aluminum billet. Wire extrusion tests were conducted, and finite element models for wire extrusion were introduced. But it is still necessary to investigate some related topics in future.

- Powder compaction and wire extrusion tests under other heated conditions could be further investigated. The material property would exhibit a different characteristic under different temperature conditions.

- Vibration assisted powder compaction method can be further investigated. Much more vibration loading conditions can be conducted to confirm the effect of the vibration loading method. The combinations of other higher vibration frequencies and/or amplitudes can be investigated for future study.

- Finite element models of wire extrusion can be updated further in future. The model can contain thermal conditions to predict the hot extrusion of billet. The fracture prediction during material deformation in wire extrusion process, which was observed in some tests, should also be investigated.

REFERENCES

Abrinia, K., & Mossuleh, R. T. (2009). An approximate load estimation method for three dimensional metal forming problems. *International Journal of Mechanical Sciences, 51*(11-12), 774-781.

Altinbalik, T., & Onder, A. (2013). Effect of die inlet geometry on extrusion of clover sections through curved dies: Upper bound analysis and experimental verification. *Transactions of nonferrous metals society of China, 23*(4), 1098-1107.

An, X., Xing, Z., & Jia, C. (2014). Cold Compaction of Copper Powders Under Mechanical Vibration and Uniaxial Compression. *Metallurgical and Materials Transactions A, 45*(4), 2171-2179. doi:10.1007/s11661-013-2160-6

Berber, S., Kwon, Y.-K., & Tománek, D. (2000). Unusually high thermal conductivity of carbon nanotubes. *Physical review letters, 84*(20), 4613.

Bier, W., Dariel, M., Frage, N., Hartmann, S., & Michailov, O. (2007). Die compaction of copper powder designed for material parameter identification. *International Journal of Mechanical Sciences, 49*(6), 766-777.

Bressan, J. D., Martins, M. M., & Button, S. T. (2015). Analysis of aluminium hot extrusion by finite volume method. *Materials Today: Proceedings, 2*(10), 4740-4747.

Cante, J. C., Oliver, J., González, C., Calero, J. A., & Benítez, F. (2013). On numerical simulation of powder compaction process: powder transfer modelling and characterisation. *Powder Metallurgy, 48*(1), 85-92. doi:10.1179/003258905x37684

Chakrabarty, J. (2010). *Applied plasticity* (Vol. 758): Springer.

Chanda, T., Zhou, J., & Duszczyk, J. (2001). A comparative study on iso-speed extrusion and isothermal extrusion of 6061 Al alloy using 3D FEM simulation. *Journal of Materials Processing Technology, 114*(2), 145-153.

Chen, L., Zhao, G., Yu, J., & Zhang, W. (2015). Constitutive analysis of homogenized 7005 aluminum alloy at evaluated temperature for extrusion process. *Materials & Design (1980-2015), 66*, 129-136. doi:10.1016/j.matdes.2014.10.045

Chen, W., Davies, C., Samarasekera, I., Brimacombe, J., & Hawbolt, E. (1996). Mathematical modeling of the extrusion of 6061/Al 2 O 3/20 p composite. *Metallurgical and Materials Transactions A, 27*(12), 4095-4111.

Chen, Z., Ikeda, K., Murakami, T., Takeda, T., & Xie, J.-X. (2003). Fabrication of composite pipes by multi-billet extrusion technique. *Journal of Materials Processing Technology, 137*(1-3), 10-16. doi:10.1016/s0924-0136(02)01052-x

Dash, K., Ray, B. C., & Chaira, D. (2012). Synthesis and characterization of copper–alumina metal matrix composite by conventional and spark plasma sintering. *Journal of Alloys and compounds, 516*, 78-84.

Dong, Y., Zhang, C., Zhao, G., Guan, Y., Gao, A., & Sun, W. (2016). Constitutive equation and processing maps of an Al–Mg–Si aluminum alloy: Determination and application in simulating extrusion process of complex profiles. *Materials & Design, 92*, 983-997. doi:10.1016/j.matdes.2015.12.113

Earp, B., Dunn, D., Phillips, J., Agrawal, R., Ansell, T., Aceves, P., . . . Luhrs, C. (2020). Enhancement of electrical conductivity of carbon nanotube sheets through copper addition using reduction expansion synthesis. *Materials Research Bulletin, 131*, 110969.

Farhoumand, A., & Ebrahimi, R. (2016). Experimental investigation and numerical simulation of plastic flow behavior during forward-backward-radial extrusion process. *Progress in Natural Science: Materials International, 26*(6), 650-656.

Fartashvand, V., Abdullah, A., & Vanini, S. A. S. (2017). Effects of high power ultrasonic vibration on the cold compaction of titanium. *Ultrasonics sonochemistry, 36*, 155-161.

Feng, Y., Mei, D., & Wang, Y. (2019). Cohesive zone method based multi particle finite element simulation of compaction densification process of Al and NaCl laminar composite powders. *Journal of Physics and Chemistry of Solids, 134*, 35-42.

Fiétier, N., Krähenbühl, Y., & Vialard, M. (2009). New methods for the fast simulations of the extrusion process of hot metals. *Journal of Materials Processing Technology, 209*(5), 2244-2259. doi:10.1016/j.jmatprotec.2008.05.022

Flitta, I., & Sheppard, T. (2005). Effect of pressure and temperature variations on FEM prediction of deformation during extrusion. *Materials science and technology, 21*(3), 339-346.

Garner, S., Strong, J., & Zavaliangos, A. (2018). Study of the die compaction of powders to high relative densities using the discrete element method. *Powder technology, 330*, 357-370.

Ghorbani, A., Sheibani, S., & Ataie. (2018). Microstructure and mechanical properties of consolidated Cu-Cr-CNT nanocomposite prepared via powder metallurgy. *732*, 818-827.

Gordon, W., Van Tyne, C., & Sriram, S. (2002). Extrusion through spherical dies—an upper bound analysis. *J. Manuf. Sci. Eng., 124*(1), 92-97.

Groche, P., Kramer, P., Bay, N., Christiansen, P., Dubar, L., Hayakawa, K., . . . Moreau, P. (2018). Friction coefficients in cold forging: A global perspective. *CIRP Annals, 67*(1), 261-264. doi:10.1016/j.cirp.2018.04.106

Guillon, O., Gonzalez-Julian, J., Dargatz, B., Kessel, T., Schierning, G., Räthel, J., & Herrmann, M. (2014). Field-Assisted Sintering Technology/Spark Plasma Sintering: Mechanisms, Materials, and Technology Developments. *Advanced Engineering Materials, 16*(7), 830-849. doi:10.1002/adem.201300409

Hansson, S., & Jansson, T. (2010). Sensitivity analysis of a finite element model for the simulation of stainless steel tube extrusion. *Journal of Materials Processing Technology, 210*(10), 1386-1396.

Heckel, R. (1961). Density-pressure relationships in powder compaction. *Trans Metall Soc AIME, 221*(4), 671-675.

Hosseinabadi, H. G., & Serajzadeh, S. (2014). Hot extrusion process modeling using a coupled upper bound-finite element method. *Journal of Manufacturing Processes, 16*(2), 233-240.

Johnson, W. (1956). The pressure for the cold extrusion of lubricated rod through square dies of moderate reduction at slow speeds. *Journal of the Institute of Metals, 85*(403), 1790-1799.

Johnson, W., & Mellor, P. B. (1983). Engineering plasticity.

Kazanowski, P., Epler, M. E., & Misiolek, W. Z. (2004). Bi-metal rod extrusion—process and product optimization. *Materials Science and Engineering: A, 369*(1-2), 170-180.

Khoei, A. R., Azami, A., & Azizi, S. (2007). Computational modeling of 3D powder compaction processes. *Journal of Materials Processing Technology, 185*(1-3), 166-172.

Kim, D., Park, K., Kim, K., Miyazaki, T., Joo, S., Hong, S., & Kwon, H. (2019). Carbon nanotubes-reinforced aluminum alloy functionally graded materials fabricated by powder extrusion process. *Materials Science and Engineering: A, 745*, 379-389. doi:10.1016/j.msea.2018.12.128

Kim, P., Shi, L., Majumdar, A., & McEuen, P. L. (2001). Thermal transport measurements of individual multiwalled nanotubes. *Physical review letters, 87*(21), 215502.

Kwon, H., Estili, M., Takagi, K., Miyazaki, T., & Kawasaki, A. (2009). Combination of hot extrusion and spark plasma sintering for producing carbon nanotube reinforced aluminum matrix composites. *Carbon, 47*(3), 570-577.

Liu, J., Khan, U., Coleman, J., Fernandez, B., Rodriguez, P., Naher, S., & Brabazon, D. (2016). Graphene oxide and graphene nanosheet reinforced aluminium matrix composites: Powder synthesis and prepared composite characteristics. *Materials & Design, 94*, 87-94. doi:10.1016/j.matdes.2016.01.031

Long, X., Bai, Y., Algarni, M., Choi, Y., & Chen, Q. (2015). Study on the strengthening mechanisms of Cu/CNT nano-composites. *Materials Science and Engineering: A, 645*, 347-356.

Lowrie, J., & Ngaile, G. (2016). Analytical modeling of hydrodynamic lubrication in a multiple-reduction drawing die. *Procedia Manufacturing, 5*, 707-723.

Majzoobi, G., Atrian, A., & Enayati, M. (2015). Tribological properties of Al7075-SiC nanocomposite prepared by hot dynamic compaction. *Composite Interfaces, 22*(7), 579-593.

Mamalis, A., Vottea, I., & Manolakos, D. (2001). On the modelling of the compaction mechanism of shock compacted powders. *Journal of Materials Processing Technology, 108*(2), 165-178.

Mansoor, M., & Shahid, M. (2016). Carbon nanotube-reinforced aluminum composite produced by induction melting. *Journal of Applied Research and Technology, 14*(4), 215-224. doi:10.1016/j.jart.2016.05.002

Marín, M., Camacho, A., & Pérez, J. (2017). Influence of the temperature on AA6061 aluminum alloy in a hot extrusion process. *Procedia Manufacturing, 13*, 327-334.

Mintmire, J. W., Dunlap, B. I., & White, C. T. (1992). Are fullerene tubules metallic? *Physical review letters, 68*(5), 631.

Mohammed, S. M., & Chen, D. L. (2020). Carbon Nanotube-Reinforced Aluminum Matrix Composites. *Advanced Engineering Materials, 22*(4), 1901176.

Ong, P., Chin, D. D. V. S., Ho, C. S., & Ng, C. H. (2018). Modeling and optimization of cold extrusion process by using response surface methodology and metaheuristic approaches. *Neural Computing and Applications, 29*(11), 1077-1087.

Parilak, L., Dudrova, E., Bidulsky, R., & Kabatova, M. (2017). Derivation, testing and application of a practical compaction equation for cold die-compacted metal powders. *Powder technology, 322*, 447-460.

Qamar, S. Z., Chekotu, J. C., & Qamar, S. B. (2019). Effect of shape complexity on Ram pressure and metal flow in aluminum extrusion. *JOM, 71*(12), 4378-4392.

Rahmani, K., Majzoobi, G., & Atrian. (2018). A novel approach for dynamic compaction of Mg–SiC nanocomposite powder using a modified Split Hopkinson Pressure Bar. *Powder Metallurgy, 61*(2), 164-177.

Reddy, N. V., Sethuraman, R., & Lal, G. (1996). Upper-bound and finite-element analysis of axisymmetric hot extrusion. *Journal of Materials Processing Technology, 57*(1-2), 14-22.

Rothe, S., Kalabukhov, S., Frage, N., & Hartmann, S. (2016). Field assisted sintering technology. Part I: Experiments, constitutive modeling and parameter identification. *GAMM-Mitteilungen, 39*(2), 114-148.

Saboori, A., Novara, C., Pavese, M., Badini, C., Giorgis, F., & Fino, P. (2017). An investigation on the sinterability and the compaction behavior of aluminum/graphene nanoplatelets (GNPs) prepared by powder metallurgy. *Journal of Materials Engineering, 26*(3), 993-999.

Shang, C., Sinka, I., & Pan, J. (2012). Constitutive model calibration for powder compaction using instrumented die testing. *Experimental Mechanics, 52*(7), 903-916.

Sharififar, M., & Mousavi, S. A. (2015). Simulation and optimization of hot extrusion process to produce rectangular waveguides. *The International Journal of Advanced Manufacturing Technology, 79*(9), 1961-1973.

Shatermashhadi, V., Manafi, B., Abrinia, K., Faraji, G., & Sanei, M. (2014). Development of a novel method for the backward extrusion. *Materials & Design (1980-2015), 62*, 361-366.

Shin, S., Choi, H., & Bae, D. (2013). Electrical and thermal conductivities of aluminum-based composites containing multi-walled carbon nanotubes. *Journal of composite materials, 47*(18), 2249-2256.

Shokrollahi, H., & Janghorban, K. (2007). Soft magnetic composite materials (SMCs). *Journal of Materials Processing Technology, 189*(1-3), 1-12.

Sinka, I., Cocks, A., Morrison, C., & Lightfoot, A. (2000). High pressure triaxial facility for powder compaction. *Powder Metallurgy, 43*(3), 253-262.

Smil, V. (2016). *Energy transitions: global and national perspectives*: ABC-CLIO.

Strzępek, P., Mamala, A., Zasadzińska, M., Franczak, K., & Jurkiewicz, B. (2019). Research on the drawing process of Cu and CuZn wires obtained in the cryogenic conditions. *Cryogenics, 100*, 11-17. doi:10.1016/j.cryogenics.2019.03.007

Sundaram, R. M., Sekiguchi, A., Sekiya, M., Yamada, T., & Hata, K. (2018). Copper/carbon nanotube composites: research trends and outlook. *Royal Society open science, 5*(11), 180814.

Sung-Kyu, K., & Tae-Sung, O. (2011). Electrodeposition behavior and characteristics of Ni-carbon nanotube composite coatings. *Transactions of nonferrous metals society of China, 21*, s68-s72.

Tang, T., Shao, Y., Li, D., Peng, L., Peng, Y., Zhang, S., & Wu, P. (2018). Polycrystal plasticity simulation of extrusion of a magnesium alloy round bar: Effect of strain path non-uniformity. *Journal of Alloys and Compounds, 730*, 161-181. doi:10.1016/j.jallcom.2017.09.162

Tans, S. J., Devoret, M. H., Dai, H., Thess, A., Smalley, R. E., Geerligs, L., & Dekker, C. (1997). Individual single-wall carbon nanotubes as quantum wires. *Nature, 386*(6624), 474-477.

Thümmler, F., & Oberacker, R. (1993). *An introduction to powder metallurgy* (Vol. 490): Institute of Materials London.

Wagener, H. (1994). Coefficient of friction in cold extrusion. *J. Mater. Process. Technol., 44*, 283-291.

Wang, G., Cai, Y., Ma, Y., Tang, S., Syed, J., Cao, Z., & Meng, X. (2019). Ultrastrong and Stiff Carbon Nanotube/Aluminum–Copper Nanocomposite via Enhancing Friction between Carbon Nanotubes. *Nano letters, 19*(9), 6255-6262.

Wistreich, J. (1955). Investigation of the mechanics of wire drawing. *Proceedings of the Institution of Mechanical Engineers, 169*(1), 654-678.

Wu, C.-Y., Ruddy, O., Bentham, A., Hancock, B., Best, S., & Elliott, J. (2005). Modelling the mechanical behaviour of pharmaceutical powders during compaction. *Powder technology, 152*(1-3), 107-117.

Wu, Y., Huang, S., Chen, Q., Feng, B., Shu, D., & Huang, Z. (2019). Microstructure and Mechanical Properties of Copper Billets Fabricated by the Repetitive Extrusion and Free Forging Process. *Journal of Materials Engineering and Performance, 28*(4), 2063-2070. doi:10.1007/s11665-019-03898-3

Wu, Y., & Kim, G.-Y. (2011). Carbon nanotube reinforced aluminum composite fabricated by semi-solid powder processing. *Journal of Materials Processing Technology, 211*(8), 1341-1347. doi:10.1016/j.jmatprotec.2011.03.007

Yim, D., Kim, W., Praveen, S., Jang, M. J., Bae, J. W., Moon, J., . . . Kim, H. S. (2017). Shock wave compaction and sintering of mechanically alloyed CoCrFeMnNi high-entropy alloy powders. *J Materials Science*

Engineering: A, 708, 291-300.

Yu, M.-F., Lourie, O., Dyer, M. J., Moloni, K., Kelly, T. F., & Ruoff, R. S. (2000). Strength and breaking mechanism of multiwalled carbon nanotubes under tensile load. *Science, 287*(5453), 637-640.

Zaharia, L., Comaneci, R., Chelariu, R., & Luca, D. (2014). A new severe plastic deformation method by repetitive extrusion and upsetting. *Materials Science and Engineering: A, 595*, 135-142.

Zeng, Z., Stanford, N., Davies, C. H. J., Nie, J.-F., & Birbilis, N. (2019). Magnesium extrusion alloys: a review of developments and prospects. *International Materials Reviews, 64*(1), 27-62.

Zhang, H., Li, L., Yuan, D., & Peng, D. (2007). Hot deformation behavior of the new Al–Mg–Si–Cu aluminum alloy during compression at elevated temperatures. *Materials Characterization, 58*(2), 168-173.

Zhou, M., Huang, S., Hu, J., Lei, Y., Zou, F., Yan, S., & Yang, M. (2017). Experiment and finite element analysis of compaction densification mechanism of Ag-Cu-Sn-In mixed metal powder. *Powder Technology, 313*, 68-81. doi:10.1016/j.powtec.2017.03.015

Zhou, Q., Song, S., Chen, Q., & Bai, Y. (2021). Comprehensive Studies on Hot Compaction and Vibration-Assisted Compaction Tests of Aluminum Powder. *Journal of Manufacturing Science and Engineering, 143*(1).